INFORMATION TO USERS

This manuscript has been reproduced from the microfilm master. UMI films the text directly from the original or copy submitted. Thus, some thesis and dissertation copies are in typewriter face, while others may be from any type of computer printer.

The quality of this reproduction is dependent upon the quality of the copy submitted. Broken or indistinct print, colored or poor quality illustrations and photographs, print bleedthrough, substandard margins, and improper alignment can adversely affect reproduction.

In the unlikely event that the author did not send UMI a complete manuscript and there are missing pages, these will be noted. Also, if unauthorized copyright material had to be removed, a note will indicate the deletion.

Oversize materials (e.g., maps, drawings, charts) are reproduced by sectioning the original, beginning at the upper left-hand corner and continuing from left to right in equal sections with small overlaps. Each original is also photographed in one exposure and is included in reduced form at the back of the book.

Photographs included in the original manuscript have been reproduced xerographically in this copy. Higher quality 6" x 9" black and white photographic prints are available for any photographs or illustrations appearing in this copy for an additional charge. Contact UMI directly to order.

UMI

A Bell & Howell Information Company
300 North Zeeb Road, Ann Arbor MI 48106-1346 USA
313/761-4700 800/521-0600

SINGLE IONIZATION IN HIGHLY CHARGED ION-ATOM COLLISIONS AT LOW TO INTERMEDIATE VELOCITIES

by

MOHAMMAD A. ABDALLAH

B.Sc., Yarmouk University, Jordan, 1991

M.Sc., Yarmouk University, Jordan, 1993

A DISSERTATION

submitted in partial fulfillment of the

requirements for the degree

DOCTOR OF PHILOSOPHY

Department of Physics

College of Arts and Sciences

KANSAS STATE UNIVERSITY

Manhattan, Kansas

1998

Approved by:

C. Lewis Cocke

Major Professor

C. Lewis Cocke

UMI Number: 9833749

UMI Microform 9833749
Copyright 1998, by UMI Company. All rights reserved.

This microform edition is protected against unauthorized copying under Title 17, United States Code.

UMI
300 North Zeeb Road
Ann Arbor, MI 48103

SINGLE IONIZATION IN HIGHLY CHARGED ION-ATOM COLLISIONS AT LOW TO INTERMEDIATE VELOCITIES

by

MOHAMMAD A. ABDALLAH

B.Sc., Yarmouk University, Jordan, 1991

M.Sc., Yarmouk University, Jordan, 1993

AN ABSTRACT OF A DISSERTATION

submitted in partial fulfillment of the

requirements for the degree

DOCTOR OF PHILOSOPHY

Department of Physics

College of Arts and Sciences

KANSAS STATE UNIVERSITY

Manhattan, Kansas

1998

Abstract

Single electron ejection from neutral targets (He and Ne) by the impact of low to highly charged ions (p, He^+, Ne^+, He^{2+}, C^{6+}, O^{8+}, and Ne^{10+}) at low to intermediate impact velocities is studied. A novel technique of electron momentum imaging is implemented. In this technique two-dimensional electron momentum distributions are produced in coincidence with recoil ions and projectile ions. In the first generation experiments we studied the ejected electron momentum distributions without analyzing recoil ions momentum. This series of experiments revealed a charge-state dependence and velocity dependence that are contradictory to a dominant saddle point ionization mechanism at intermediate velocities. It showed a possibility of an agreement with a saddle centered distributions for low charge states at low collision velocities. To pursue the problem in more detail, we developed a second generation spectrometer which allowed us to fully determine the recoil ions momentum. Fully determined recoil-ion momentum allowed us to determine the collision plane, energy loss (Q-value), and impact parameter for every collision that resulted in a single (target) ionization. This series of experiments revealed for the first time very marked structures in electron spectra that were impossible to observe in other experiments. These structures are due to the quasi-molecular nature of the collision process even at velocities comparable to the electron "classical" orbital velocity. For the collisions of p, He^+, and He^{2+} with He, a π-orbital shape of the electron momentum distribution is observed. This indicates the importance of the rotational coupling $2p\sigma \rightarrow 2p\pi$ in the initial promotion of the ground state electron followed by further promotions to the continuum.

Contents

Table of Contents i

List of Figures iv

List of Tables x

Acknowledgments xi

1 Introduction **1**

2 Review of the Ionization Theory **11**

2.1 Introduction 11

2.2 Ionization Mechanisms 13

2.3 Theories Studying Ionization 16

2.3.1 Perturbative Methods 16

2.3.2 Binary Encounter Approximation (BEA) 18

2.3.3 Classical-Trajectory Monte Carlo Method (CTMC) 18

2.4 Theory of Slow Atomic Collisions 20

2.4.1 Adiabatic and Diabatic Representations 20

2.4.2 Dynamical Coupling 23

2.4.3 Correlation Diagrams 25

2.4.4 Electron Promotion Model and Translational Energy Spectroscopy 25

2.5 Theory of Hidden Crossings 34

3 Electron Momentum Imaging **40**

3.1 Experimental technique 41

3.1.1 Experimental Setup 41

3.1.2 Electron Momentum Calculation 48

3.1.3 Experimental Resolution 52

3.2 Velocity Dependence of the EEMDs 54

3.2.1 p + He, Ne 55

3.2.2 C^{6+} + He, Ne 63

3.3 Projectile Charge-State Dependence of the EEMDs 65

4 Electron-Momentum Imaging: Fully Determined Recoil-Ion momentum **75**

4.1 Experimental Technique 76

4.1.1 Experimental Setup 76

4.1.2 Data Reduction 84

4.2 Results and Discussion 85

4.2.1 He^{+} + He 85

4.2.2 He^{2+} + He 99

4.2.3 C^{6+} + He 105

5 Concluding Remarks **121**

Appendices **125**

A Simulation of the Time-of-Flight-Position Spectrometer; First Generation **125**

B Simulation of the Time-of-Flight-Position Spectrometer; Second Generation **128**

C Atomic Beam Sources **133**

C.1 Effusive Atomic Beam 133

C.2 Supersonic Atomic Beam 136

D Gas Jet Operation **139**

D.1 Jet-Skimmer Parameters 139

D.2 System Differential Pumping 142

D.3 Gas Input Control 147

E Signal Extraction from the Detectors **150**

F Other Collision Systems **154**

G Data Analysis Code **167**

References **185**

List of Figures

1.1 Total ionization cross section of He by highly charged projectiles . . . 7

2.1 Coordinate system used to describe the collision of a bare ion Z_1 with hydrogen-like atom (with a nuclear charge Z_2). 21

2.2 Correlation diagrams for homo-nuclear and heteronuclear molecules . 26

2.3 Schematic correlation diagram for the He^+ - He system 29

2.4 Spectrum of scattered He^+ ions obtained for 1 kev He^+ + He collisions at $\theta = 8°$ detection angle 30

2.5 Energy loss spectra of the scattered ions He^+ for the collision system He + He 32

2.6 Angular distributions of the scattered ions (He^+) in low energy collisions of He + He 33

2.7 Potential energy curves for H_2^+ quasi-molecule along different axes in the complex plane of the internuclear distance 37

2.8 The same as Fig.2.7, but in the complex $R^{1/2}$ plane instead of the plane of R 38

2.9 Real part of the potential energy as a function of the complex internuclear distance R for two levels connected by an S-type branch point 39

3.1 Schematic sketch of the time-of-flight-position spectrometer of the first-generation experiments 42

3.2 Schematic of the first-generation experiments arrangement 44

3.3 Block diagram of the basic electronics of the first-generation experiments 46

3.4 Simple geometry illustrating the method used in determining the absolute position of the electrons on the electron detector 49

3.5 Electron-momentum distribution from the transfer ionization channel 51

3.6 Contour plots of the two-dimensional electron momentum distributions for p + He collisions 56

3.7 Z- and Y-electron momentum distributions from the ionization channel for p + He collisions for v_p = 2.39, 1.71, 1.15, 0.85, and 0.63 a.u. . 58

3.8 The same experimental data as displayed in Fig. 3.7(a) but the projection onto the Z axis is only for small Y momentum ($v_y \approx \pm 0.18$ a.u.) 61

3.9 Plot of the experimental Z-electron momentum distributions vs the Z-electron velocity over the projectile velocity for p + He collisions resulting in pure ionization. 62

3.10 Contour plots of the two-dimensional electron momentum distribution from C^{6+} + He collisions 64

3.11 Z- and Y-electron momentum distributions from the ionization channel for C^{6+} + He collisions for v_p = 1.63, 1.38, and 1.16 a.u. 66

3.12 Experimental Z-electron momentum distributions vs the Z-electron velocity over the projectile velocity for C^{6+} +He collisions 67

3.13 Contour plots of the two-dimensional electron-momentum distribution from p, He^{2+}, C^{6+}, O^{8+}, and Ne^{10+} + He, and Ne collisions . . . 69

3.14 Z- and Y-electron momentum distributions from the ionization channel for p, He^{2+}, C^{6+}, O^{8+}, and Ne^{10+} + He collisions at $v_p = 1.63$ a.u. 70

3.15 Z- and Y-electron momentum distributions from the ionization channel for p, He^{2+}, C^{6+}, O^{8+}, and Ne^{10+} + Ne collisions at $v_p = 1.63$ a.u. 71

3.16 Theoretical CDW-EIS calculations for the systems shown in Fig. 3.14 72

3.17 Slices of three selected two-dimensional momentum distributions projected into the longitudinal direction with $| v_y | < 0.2$ a.u. 74

4.1 Schematic sketch of the experimental setup in the second-generation experiments 77

4.2 Time-of-flight-position spectrometer used in extracting and detecting electrons and recoil ions 78

4.3 Schematic sketch of the voltage distribution on different parts of the second-generation spectrometer 80

4.4 The coordinate system used in describing the results of this experiment. 82

4.5 Recoil-ion transverse momentum distribution in the collision He^+ + He 86

4.6 Recoil-ion transverse momentum vs longitudinal momentum for 10 keV/u He^+ + He 88

4.7 Q-value distribution in the collision 10 keV/u He^+ + He 89

4.8 Side view of ejected electron momentum distribution in the collision 10 keV/u He^+ + He 92

4.9 Top view of the ejected electron momentum distribution in the collision 10 keV/u He^+ + He 93

4.10 Top view of the ejected electron momentum distribution in the collision 10 keV/u He^+ + He 95

4.11 Recoil-ion transverse momentum distribution in the collision He^+ + He at projectile velocities v_p = 0.45 - 1.00 a.u. 97

4.12 Top view of the ejected electron momentum distribution in the collision of He^+ + He at v_p = 0.45 - 1.00 a.u. 98

4.13 Recoil-ion transverse momentum distribution in the collision He^{2+} + He at projectile velocities v_p = 0.45 - 1.00 a.u. 100

4.14 Top view of the ejected electron-momentum distribution in the collision of He^{2+} + He at v_p = 0.45 - 1.00 a.u. 102

4.15 Average transverse velocity in the scattering plane for v_{ez} around $0.5v_p$ 104

4.16 Recoil-ion transverse momentum ($p_{r\perp}$) vs longitudinal momentum ($p_{r\parallel}$) for the collision C^{6+} + He at v_p = 1.36 a.u. 107

4.17 Recoil-ion transverse momentum for the collision C^{6+} + He at v_p = 1.63, 1.36, and 1.17 a.u. 108

4.18 Top view, side view, and the total distribution of the emitted electrons in C^{6+} + He at v_p = 1.63 a.u. 110

4.19 Top view, side view, and the total distribution of the emitted electrons in C^{6+} + He at v_p = 1.36 a.u. 111

4.20 Top view, side view, and the total distribution of the emitted electrons in C^{6+} + He at v_p = 1.17 a.u. 112

4.21 Top view of the emitted electrons in C^{6+} + He at v_p = 1.63 a.u. gated on different ranges of recoil- ion transverse momentum. 114

4.22 Longitudinal and transverse projections of the 2-D distributions in Fig. 4.21 115

4.23 Top view of the emitted electrons in C^{6+} + He at $v_p = 1.36$ a.u. . . . 117

4.24 Top view of the emitted electrons in C^{6+} + He at $v_p = 1.17$ a.u. . . . 118

4.25 Longitudinal and transverse projections of the 2-D distributions in Fig. 4.23 119

4.26 Longitudinal and transverse projections of the 2-D distributions in Fig. 4.24 120

A.1 Simulation of the time-of-flight-position spectrometer of the first-generation experiments 126

B.1 Simulation of the time-of-flight-position spectrometer of second-generation experiments 129

B.2 Simulation of the trajectories of some of the recoil ions in the second-generation time-of-flight-position spectrometer. 131

B.3 Simulation of the trajectories of some of the electrons in the second-generation time-of-flight-position spectrometer. 132

D.1 Jet-skimmer system employed in the experiment 140

D.2 Schematic diagram of the experimental setup 143

D.3 Pressure in the catcher and the chamber regions 146

D.4 Schematic sketch of the target-gas flow control system. 148

E.1 Time and position signals extraction from a wedge-strip-type position sensitive detector. 152

F.1 Recoil-ion transverse momentum distributions in the collision Ne^+ + Ne at projectile velocities v_p = 0.25 - 0.55 a.u. 156
F.2 Recoil-ion transverse momentum versus longitudinal momentum for the collision Ne^+ + Ne at v_p = 0.45 a.u. 157
F.3 Q-value distribution for the collision Ne^+ + Ne at v_p = 0.45 a.u. . . . 158
F.4 Top view and side view of the ejected electrons in the collision of Ne^+ + Ne at v_p = 0.45 a.u. 159
F.5 Top view of the ejected electrons in the collision of Ne^+ + Ne at v_p = 0.45 a.u. 160
F.6 Recoil-ion transverse momentum versus longitudinal momentum for the collision Ne^+ + Ne at v_p = 0.35 a.u. 161
F.7 Top view and (b) side view of the ejected electrons in the collision of Ne^+ + Ne at v_p = 0.35 a.u. 162
F.8 Top view of the ejected electrons in the collision of Ne^+ + Ne at v_p = 0.35 a.u. 163
F.9 Recoil-ion transverse momentum distributions in the collision He^+ + Ne at projectile velocities v_p = 0.33 - 0.78 a.u. 164
F.10 Recoil-ion transverse momentum versus longitudinal momentum for the collision He^+ + Ne at v_p = 0.33 a.u. 165
F.11 Top view and side view of the ejected electrons in the collision of He^+ + Ne at v_p = 0.33 a.u. 166

List of Tables

3.1 Values by which the CDW-EIS and CTMC present theoretical results were multiplied in the Z and Y directions so that the peaks of the distributions coincide with those of the present experimental results . 59

D.1 Table of the pressure in the five differentially pumped regions 145

Acknowledgments

First, praise be to Allah, most gracious, most merciful for that he helped me and guided me all the time. I vow this work to Allah hoping for His acceptance. My thanks go to my parents Abdallah and Aqilah Nazzal for their love, support and the faith they raised me on. Everything I accomplished or will accomplish in my life is the fruit of their work and patience. My thanks also go to my brothers and sisters for their continuous support and love. My thanks are to my fiancé, Shorouk, for her love and encouragement since the first day I met her.

No words will be enough in expressing my immense gratitude and appreciation for Professor C. Lewis Cocke, my major advisor. He provided me with the opportunity to work with him and learn from him all what it means to be a physicist. Working with Lew made me trust my abilities and made me love the experimental research. He is my highest example of competence and professional integrity.

I would like to thank my committee members, Prof. Patrick Richard, Prof. Itzhak Ben-Itzhak and Prof. J. Kenneth Shultis for many helpful discussions and for reviewing this dissertation. I would like also to thank Prof. Peter Sherwood for serving as the defense chairman and for reviewing this dissertation.

My special thanks are extended to Prof. Martin Stöckli for his continuous advice and help. Martin's critical review for the experimental design was an essential factor in the success of the experiments presented in this dissertation. I would like also to express my appreciation for Prof. Chii-Dong Lin for teaching me the principles of atomic physics and for many helpful discussions. Thanks also go to Prof. Brett Depaola and Prof. Sieggbert Hagmann for many helpful discussions.

I would like to express my appreciation for Prof. R. Olson for providing the classical trajectory Monte-Carlo calculations, Dr. V. D. Rodriguez and Dr. Y. D.

Wang for providing the CDW-EIS calculations, and for Dr. Emil Sidky for many helpful discussions and for his calculations for the studied systems.

In this opportunity I would like to extend my appreciation and thanks for all researchers who educated me or participated in this research over the years: Prof. Emmanuel Kamber, Prof. Hans Wolf, Prof. Wanya Wolff, Dr. Mark Raphaelian, Dr. Scott Kravis, Dr. Wuchun Wu, Dr. Slawek Winecki, Bernhard Walch, Chun-Yen Chen, Lamya Salih and Allen Landers.

The technical support provided by J. R. Macdonald personnel was important in the success of our experimental work. My deepest thanks are for Prof. Kevin Carnes for providing help on the laboratory computer network and data acquisition system. Kevin's immediate help was crucial factor in the success of the experiments. I would like to thank also Paul Gibson for his technical support and tuning the CRYEBIS beam, Vincent Needham for assistance on and maintenance of the laboratory network of personal computers, Tracy tipping for he taught us the basics of safety in the laboratory, Dave Hill and Bob Geering for crafting the needed parts for different experiments with great precision, and Steve Kelly for providing some electronics and cables.

Special thanks go to my friend and colleague Kastro Hamed for proofreading the manuscript of this dissertation and his continuous encouragement during all stages of my research.

Finally, my thanks are extended for all of my friends in Manhattan, Kansas. I can not name all of them in this little space but all of them had an impact on me that helped me and encouraged me for more excellent research. My special thanks go to my roommates Khalid Al-Khatib and Imad Yaseen for they did not ask me to clean the house while I was working on this dissertation.

Chapter 1

Introduction

Ionization is a process in which an atom loses one (or more) of its electrons to the continuum or to another atom. It is common to refer to the former process simply as ionization and to the latter as capture (transfer). It is electron ejection to the continuum that we are treating in this dissertation. The process of ionization occurs in nature as a result of interactions of photons, electrons, or other atoms or ions with matter.

The process of ionization has been the subject of a significant amount of research in the last fifty years. Understanding this process and inelastic processes in atomic collisions in general is important for a broad range of pure and applied research fields such as astrophysics and stellar structure and evolution [1], plasma physics and thermonuclear fusion [2, 3], surface and material study and modification [4-7], and radiation detection. On the theoretical side the process of ionization is of special importance as it is a critical test for studying the multi-particle problem.

The mechanisms leading to single electron ionization are well understood and well reproduced by theoretical calculations at large impact velocities ($v_p \gg v_o$,

where v_p is the projectile velocity and v_o is the classical bound electron velocity in the target atom). In a recent publication [8] Stolterfoht, DuBois, and Rivarola gave a very detailed review of ionization mechanisms in ion-atom collisions. Target direct ionization (DI) in soft collisions is responsible for the largest fraction of the ionization total cross section [9]. This mechanism leaves electrons in the target continuum. In addition, a few other mechanisms can be identified. One of these is the binary encounter (BE) mechanism, which is a hard projectile-electron collision in which the target nucleus is a spectator [10-12]. Electron capture to the continuum (ECC) is a mechanism that accounts for a small fraction of the total cross section and leaves electrons in the projectile continuum [13-18].

On the experimental side, most of what we know about ionization process in ion-atom collisions was learned through total cross section measurements and singly and doubly differential cross sections of the ejected electrons. The use of electrostatic electron energy analyzers introduced in the sixties has been the major experimental method. In this technique the electron energy is measured at a specific ejection angle. To obtain the angular distribution of the ejected electrons, this kind of measurement must be repeated at different angles. Although this technique remains the standard method, it suffers from certain problems when very low energy electrons are to be studied. Stray electrons, which can be generated through beam or electron collisions with slits and surfaces in the analyzing system, can appear as false slow electrons. The presence of stray magnetic fields can deflect slow electrons resulting in incorrect measurements. Finally, the limited solid angle of typical electrostatic analyzers is quite small, usually about 10^{-4} ster.

In the collisions where $v_p \leq v_o$, the basic mechanisms which lead to continuum electron production are poorly understood. This has lead to much research on this

subject since the beginning of the last decade. Although the picture of an electron falling to the effect of either the projectile or the target ion was sufficient in qualitative understanding of the ionization process at high velocities, it was realized that at intermediate to low velocities a combined effect of the two Coulomb centers on the ejected electron should be taken into account in what is known as the two-center effect [19-25]. In 1983 Olson [26] used the classical-trajectory Monte Carlo method (CTMC) to study ionization and electron capture in the H^++H(1s) collision. He noted that a large fraction of the forward emitted electrons were with velocities approximately equal to half the velocity of the projectile. In a classical description these electrons will be electrons that were left "stranded" at the point where they feel equal and opposite forces from the projectile and the target core ions. While the two Coulomb centers are receding from each other, those electrons will be pushed to higher levels with the rising saddle point. Eventually this will leave the saddle-riding electrons in the continuum when the two Coulomb centers become infinitely separated. Olson [27] and Olson *et al.* [28] studied in more detail those electrons within the CTMC framework and referred to them as $v_p/2$ electrons. This mechanism found support from coupled channel calculations by Winter and Lin [29]. They found that the inclusion of a third center at the equiforce point in their close-coupling calculations resulted in a large improvement in the calculated cross section compared to early experimental results by Fite *et al.* [30]. However, Winter and Lin calculations were carried out at relatively smaller impact energies compared to the CTMC calculations by Olson and coworkers.

More recently this mechanism found additional support from the hidden crossing theory [31-37]. In this theory two major mechanisms leading to ionization are identified: they are called the T and the S processes. In both processes the electron

is promoted to the continuum via successive hidden crossings of the quasi-molecular states formed during the collision. The term "hidden" was used since those crossings take place in the complex plane of the inter-nuclear axis. The T process promotes electrons to the continuum while the two Coulomb centers are receding from each other. This process is the quantum mechanical analog of the "classical" saddle-point ionization mechanism. In the S process, an electron is promoted to the continuum while the two Coulomb centers are approaching each other. This process can be described classically in the following way: while the two centers are approaching each other, a centrifugal barrier is formed between them. Electrons are forbidden from existing inside this barrier. On the other hand, an electron may be pushed to the continuum while this barrier is rising (in the way to form a united atom) [38]. It was shown by Ovchinnikov and Macek [32] that this process produces electrons centered on both the target and the projectile.

Experimentally there was a great deal of work to investigate the existence or the importance of the saddle point ionization mechanism (the T process). This led to very conflicting experimental results. An electron distribution that is centered on the saddle point was expected to shift by changing projectile charge, target charge, and projectile velocity the same way as the saddle point would do. The velocity of the saddle point (v_s) can be easily shown to be:

$$v_s = \frac{v_p}{1 + \sqrt{q_p/q_t}} \quad , \tag{1.1}$$

where q_p and q_t are the projectile and the target charge states, respectively. The first experimental study of this mechanism was carried out by Olson *et al.* [28] where they studied the ionization in the collision H^++He in a projectile energy range of 60 - 200 keV. The double differential cross section at 17° was measured in the velocity space.

The peak observed between the projectile and the target (in momentum space) was considered as an indication of the saddle-point mechanism. Most of the experiments that followed focused on studying this peak. However, most of the measurements were at angles larger than 0° in order to avoid the pronounced cusp of the ECC in the forward direction. Irby *et al.* [39] studied the two collision systems H^++He and He^{2+}+He at energies of 60 - 120 kev/u. They reported electron momentum spectra that have a peak which shifts with changing projectile velocity and charge state according to eq. (1.1). The same group [40] reported later similar results for the collisions of C^+, C^{2+}, and C^{3+} with He and Ne at energies 83, 100, and 150 kev/u. In an independent work Gay *et al.* [41] showed also such behavior. On the other hand, Bernardi *et al.* [21, 42, 43] and Meckbach *et al.* [44] showed that the mentioned peak does not shift according to eq. (1.1) and the observed peak is just the remnant of the cusp at larger angles. DuBois [45] also did not see this shift in the peak in his experimental data for the collisions H^+ and He^{2+} with He in a similar energy range. He concluded that any confirmation of the existence of the saddle-point ionization mechanism based on shifts observed by Irby *et al.* [39, 40] and Gay *et al.* [41] was problematic. In a later paper [46] he measured the double differential cross section in the collision C^{q+}+He at impact energies of 100 and 150 keV/u, where the projectile charge $q = 0 - 4$. Again his data did not support the suggested saddle point ionization mechanism.

Since a considerable amount of theoretical evidence about this mechanism was given by adiabatic theories, which apply at much smaller velocities than those used in most of the previous studies, Pieksma *et al.* [47] studied the velocity distribution of the emitted electrons in the energy range of 1 - 6 keV for the collision H^++H, where adiabatic theories apply. Their experimental data show an apparent dominance of

the saddle-point (T process) ionization mechanism for energies 4 - 6 keV.

Wu *et al.* [48] measured the total cross section for single ionization of He by the impact of the bare ions C^{6+}, N^{7+}, and O^{8+} in addition to Ar^{16+} and Xe^{30+}. They found that the measured cross sections follow a certain scaling formula, namely

$$\frac{\sigma_{SI}}{q_p} \simeq A(v_p q_p^{-1/4}) e^{-C/v_p q_p^{-1/4}} \quad , \tag{1.2}$$

where A and C are constants for a given target. These constants for He target are found to be

$$A = 110 \times 10^{-16}, C = 7.24 \quad . \tag{1.3}$$

The scaled cross sections are shown in Fig. 1.1. In the velocity range for which $0.7 < v_p q_p^{-1/4} < 1.2$, this scaling agrees with the total ionization cross section predicted by the theory of hidden crossings [38]. According to this theory, ionization in this range of velocity by highly charged ions is dominated by promotion to the continuum via the T-type crossings. Although it is not conclusive, this agreement was used as an indication for a possible important role of the saddle point ionization mechanism (T process) in ionization.

Dörner *et al.* [49] applied the newly developed cold target recoil ion momentum spectroscopy (COLTRIMS) [50-52] combined with electron detection in studying electron ejection in p+He system at energies of 5, 10, and 15 keV. By measuring the three components of recoil ion momentum in addition to two components of the ejected electron momentum he managed to determine, with good accuracy, the electron momentum distributions for well-defined scattering planes. In addition he measured the transverse momentum of the recoil ions, which could be used to select different ranges of impact parameters. He noticed that ejected electrons preferred

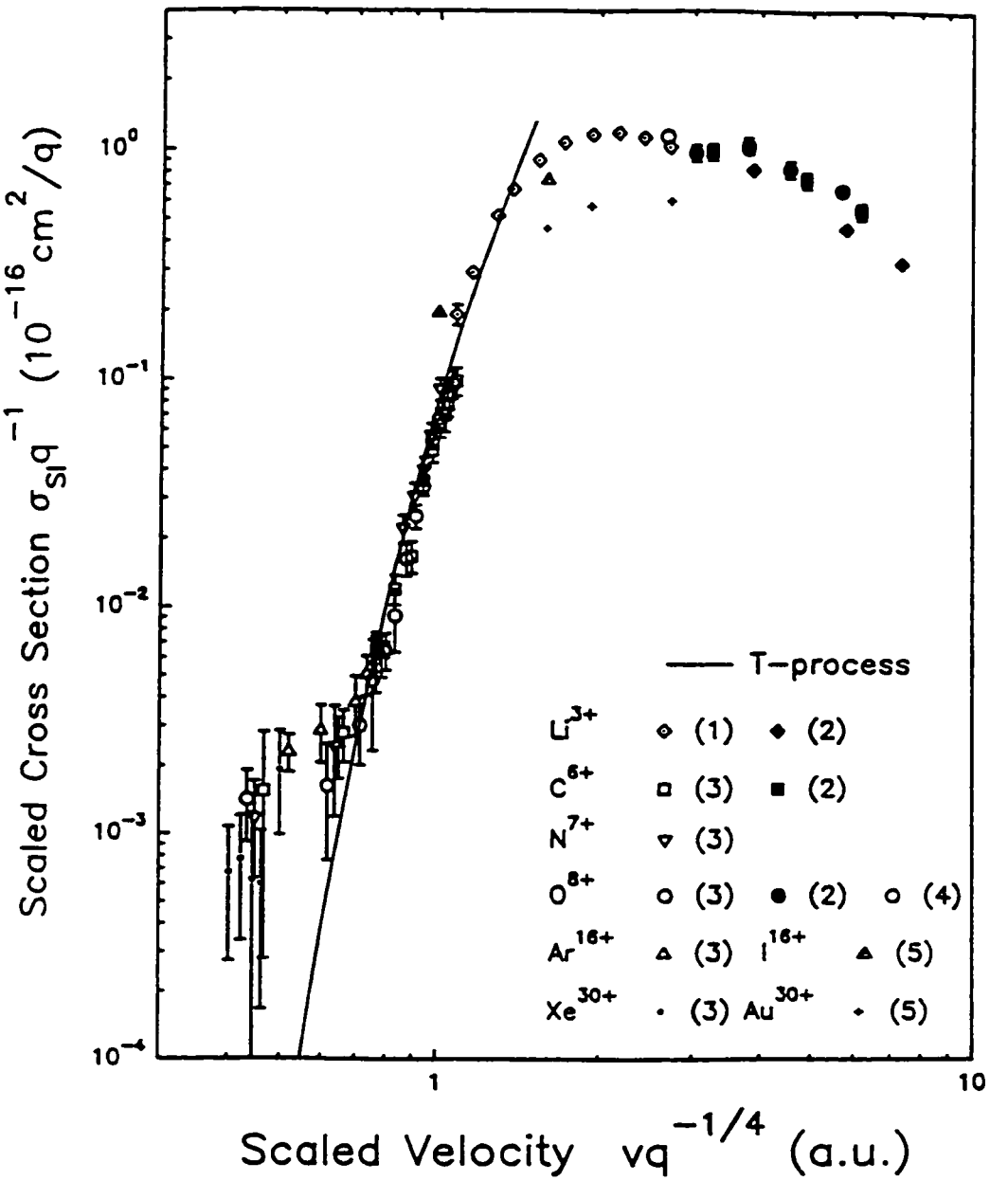

Figure 1.1: He single ionization total cross section scaled by the projectile charge (q) versus the reduced velocity of the projectile ($vq^{-1/4}$). (Adapted from Wu *et al.*[48])

to stay in the scattering plane and in the forward direction. They exhibited a marked distribution in the scattering plane where they preferred to be emitted off the inter-nuclear axis. This produced two peaks in the transverse direction and a nodal line on the inter-nuclear axis. This behavior was explained and qualitatively reproduced by the hidden crossings theory by Ovchinnikov and Macek [32, 53, 54]. Such distribution could be explained as a "signature" of the quasi-molecular states through which the electron was promoted in its way to the continuum. In the case of p on He, this was dominated by the $2p\pi$ state. An interference with other states could affect the symmetry of such distributions. A good review of the process was recently given by M. Pieksma [55].

In atomic collisions many processes leave the neutral target atom (molecule) positively charged as it loses to the projectile or to the continuum one or more of its electrons. This new ion is called a recoil ion. In the early seventies, recoil ions were used as a source of slow highly charged ions. Energy transfer to the recoil ions was of no interest in any translational energy spectroscopic study since this energy was small and dominated by the thermal energy of the particle [56]. Pioneering experiments were performed by Levin *et al.* [57] and Ullrich *et al.* [58] in 1987 in which the recoil ion's momentum was measured. Since then the technique was considerably developed at the University of Frankfurt and Kansas State University. In early experiments a warm [58] and cooled [59] static gas target was used. In later experiments effusive gas targets were used [60]. Currently, supersonic gas expansion is used to produce cold atomic beams. For more details about the principle of operation of such sources, see appendix C. The advantage of such sources is the small momentum spread of the target atoms in the three directions [52] in addition to the spatial localization of the target which is important for any attempt to reconstruct

momentum information of recoil ions.

An important improvement of the technique was extracting and detecting low energy electrons in addition to recoil ions [49, 61, 62]. This made performing kinematically complete experiments possible. Therefore, now in a single experiment one can measure the three components of momentum of the projectile, the recoil ion, and the ejected electron(s). Currently this technique is routinely used in many labs around the world. Reviews of this technique are given by Ullrich et. *al.* [50], Ullmann *et al.* [51], and Moshammer *et al.* [52].

The purpose of this dissertation is to present an independent study of the single ionization process at low to intermediate velocities. A review of ionization by charged ion impact is given in chapter 2. In this review we survey ionization mechanisms and theoretical models of ionization. Special attention is given to the molecular promotion model and early ionization experiments for their relevance to our present study. In this present study, we avoided problems encountered in most of the previous experimental studies by applying a new method of electron momentum imaging combined with recoil ion spectroscopy. This technique is very similar to the technique applied by Dörner *et al.* [49].In a first series of experiments, reported in chapter 3, we measured ejected electron momentum distributions in coincidence with charge-state analyzed recoil ions and in some cases with projectiles as well. In these experiments, no momentum transfer was measured for either the projectile or the recoil ion. Only two components of ejected electron momentum were measured. The coincidence was used only to separate ionization events from other final reaction channels. A systematic study was carried out using this technique to establish the velocity dependence and projectile charge-state dependence of the electron momentum distributions. To provide a more differential study of the electron spectra,

a second series of experiments was carried out and is reported in chapter 4. In these experiments electrons were detected in coincidence with the fully momentum-analyzed recoil ions. Projectiles were not detected. The complete momentum vector of recoil ions was measured. This made it possible to determine the energy loss (Q-value) of the collision, the scattering plane, and the scattering angle and hence the impact parameter. Concluding remarks are given in chapter 5. Some of the material presented in this dissertation has been published [61-63].

Chapter 2

Review of the Ionization Theory

2.1 Introduction

Ion-atom collisions [64-66] involve many different inelastic processes that can result in different final channels. In inelastic processes the initial states and final states are different in both energy distribution and/or configuration distribution. To give an illustration of some of the possible inelastic processes, consider for instance the collision of C^{6+} with He. Some of the possible processes are:

$$
\begin{aligned}
C^{6+} + He \longrightarrow\ & C^{6+} + He^{+} + e^{-} && \text{(single ionization)} \\
& C^{6+} + He^{2+} + 2e^{-} && \text{(double ionization)} \\
& C^{5+} + He^{+} && \text{(single capture)} \\
& C^{4+} + He^{2+} && \text{(double capture)} \\
& C^{5+} + He^{2+} + e^{-} && \text{(transfer ionization)}
\end{aligned}
$$

Additionally, the projectile or the target atom can be singly or multiply excited. For example one electron can be ionized and another, either in the target or in

the projectile, can be excited. This process of simultaneous ionization and excitation is termed ionization-excitation. In a limiting case the second electron can reach the continuum resulting in double ionization. Another process is transfer-excitation where one electron is transfered from one atom to another and another electron on either center is excited. Photons can be emitted in the cases where an excited electron falls to lower levels or to the ground state. This is termed radiative stabilization.

The cross sections for these different processes are strongly energy dependent. In general, single and multiple electron ionization are dominant at large projectile energies, while electron capture is dominant at low energies. Transfer ionization is different in nature depending on the energy range. At high energies transfer ionization is mainly single ionization accompanied by single capture. At low energies it is mainly double electron capture followed by autoionization. W. Wu in his Ph.D. dissertation [67] studied in detail the cross sections of these different processes over a wide range of energies for the impact of different highly charged ions.

In this dissertation our main interest is in single electron ejection (single ionization) from a neutral target by low to highly charged ions at low to intermediate velocities. That means we are studying this process over a range of energy where it is a weak channel compared to electron capture. This results some technical difficulties that will be explained later.

In this chapter we review the main ionization mechanisms. In addition, we survey theoretical methods that describe the process of ionization. We do not go into very detailed explanation of those theories and we refer the interested reader to some comprehensive reviews on the subject. Emphasis is placed on the theory of hidden crossings due to its relative success in explaining some of the results described in

this dissertation.

2.2 Ionization Mechanisms

Electron spectroscopy has been a very powerful technique in revealing different ionization mechanisms, especially at high projectile velocities. In the following we give a very brief review of the main identified mechanisms leading to target ionization. These mechanisms have been mostly studied using the conventional electron spectroscopy where the energy of the the emitted electrons is analyzed by electrostatic analyzers at a certain emission angle.

The interaction between the ejected electron and its mother nucleus dominates for slow ejected electrons. Those electrons are produced mainly in "soft collisions" and the mechanism is termed soft electron emission or simply direct ionization (DI). The term soft is used to describe those collisions that involve small momentum transfer to the electron which occurs at the large impact parameters. In general this process accounts for the major fraction of the ionization total cross section. The ejected electrons are strongly affected by the interaction with the target nucleus and are left centered around it in the velocity space. In conventional electron spectroscopy those electrons are called soft electrons. At very large projectile velocities they are peaked at $\theta = \pm 90°$, relative to the projectile beam direction, since they are produced in a dipole transition. This makes them symmetric along the beam direction. By reducing the projectile velocity (or increasing the projectile charge state), the effect of the projectile charge is increased due to the increased interaction time. This makes the distribution asymmetric, favoring the forward direction, which is known as the two-center effect. Both the projectile velocity and the projectile charge state are important in estimating the importance of the two center

effects. The parameter Z_p/bv_p, called Bohr parameter, is useful in estimating the importance of the two-center effect. Two-center effects are less important for the cases where $Z_p/v_p \ll 1$, since that involves a smaller interaction strength between the projectile and the ejected electron [22, 24].

One of the mechanisms that produces a distinguishable signature in electron spectra is the binary encounter mechanism. This mechanism happens in hard projectile-target electron collisions. The momentum transfer to the electron is large compared to that transfered to the target atom. The target electron can be thought of as quasi-free. Using conservation of energy and momentum, we can show that electrons ejected through binary encounter collisions have an energy that depends on their scattering angle according to [9]:

$$E_{be} = 4T cos^2\theta \quad , \tag{2.1}$$

for $0° \leq \theta \leq 90°$, where θ is the scattering angle of the ejected electron in the laboratory frame, and T is the energy of electrons that have a velocity equal to the velocity of the projectile ($T = mv_p^2/2$, where m is the electron mass and v_p is the projectile velocity). The ejected electron has a maximum energy $E_{bemax} = 4T$ at $\theta = 0°$. If the electron was completely at rest before the collision takes place, the energy E_{be} would be a delta function at every angle according to Eq. 2.1. However, the electron has a velocity distribution (Compton profile) that depends on its mother atom. This results in generating a width for the binary encounter peak.

Another process is electron capture to the continuum (ECC). In this process a target-atom electron ends up in the projectile-ion continuum. In velocity space this electron has a velocity equal to the projectile velocity. This feature has been the subject of an extensive experimental and theoretical research since the mid sixties.

It can be produced by either ionization or capture [14]. Those electrons captured into the projectile continuum appear as a cusp-shaped peak in the forward direction centered at the projectile velocity, and also known as "cusp electrons". Although the cusp electrons are mainly influenced by the projectile charge, the receding target nucleus still has an effect on them. This effect is manifested as an asymmetry in the cusp [69]. More electrons favor the low energy side of the cusp due to the considerable effect of the target nucleus. This effect, again, is referred to as a two-center effect.

In the collision of slow bare ions with atomic targets, the process of double electron capture is one of the strongest channels. The two electrons are usually captured into excited levels. De-excitation of the the projectile can happen either by photon emission (radiative stabilization) or by autoionization. In the latter process one of the electrons falls into a lower state while the other electron is ejected into the continuum as a free electron with a certain energy and angular momentum. Due to conservation of energy, the ejected electron will have a specific continuum energy. Reviews of this process and the experimental techniques used in studying it can be found, for example, in the references [70-74]. This process is part of a general phenomenon that can lead to ejecting an electron to the continuum with a specific energy, known as the Auger effect. It is experimentally inseparable from the process of transfer ionization which is two separate events of one electron capture and one electron ionization. The latter process is less likely at low and intermediate velocities. In our experiments we discriminate against such processes as they produce recoil ions that lost two electrons (He^{2+} and Ne^{2+}) which can be separated from single ionization recoil ions (He^{+} and Ne^{+}) by their different time-of-flight.

2.3 Theories Studying Ionization

In the following we summarize the major theoretical models and approximations used in describing the ionization process at higher collision velocities. The purpose of this review is just to provide a background with which to compare the case of low energy collisions covered by the experiments in this dissertation. Some of the experimental results reported in chapter 3 will be compared to the CTMC and CDW-EIS calculations.

2.3.1 Perturbative Methods

The Plane-Wave Born Approximation (PWBA) is the basis for perturbative methods in studying ionization and ion-atom collisions in general. In this approximation it is assumed that the the projectile deflection as a result of its interaction with the target nucleus is negligible. Therefore one can treat the collision as a perturbation where the projectile can be presented by a plane wave. The electronic wave function is taken to be centered on the target atom. This assumption is valid if $q_p/q_t \ll v_p/v_o$, where q_p and q_t are the projectile and the target nuclear charges, respectively. v_p is the projectile velocity and v_o is Bohr velocity.

The PWBA gives good results especially at large projectile velocities, as most of the ionizing collisions happen at large impact parameters, and therefore involve a small deflection of the projectile. This approximation reproduces the soft electron peak and the binary encounter peak. However it does not account for the electron capture to the continuum (ECC) peak [90-92], since there is no interaction between the ejected electron and the projectile within this approximation. A review of this approximation is given by Briggs and Macek [18].

In the PWBA method the projectile-target ion interaction is completely ne-

glected. This limits the applicability of the method to collisions involving small scattering angles of the projectile. The applicability of the method is extended by including the projectile-target nucleus interaction. This technique is called the distorted wave Born approximation (DWBA). Therefore, the changes in the projectile wave function due to the interaction with the target atom are taken into consideration. A review of this approximation is given by Rudd *et al.* [93].

The continuum -distorted-wave method (CDW) was first introduced by Cheshire [94] in 1964 to study charge-exchange in the collision p + H(1s). In 1978 it was used by Belkić [95] to study ionization of atoms by heavy ions. In this method all two-particle Coulomb interactions are explicitly contained in the initial- and final-state wave functions. The final state wave function is represented as a product of Coulomb wave functions for the electron-target subsystem, the electron-projectile subsystem, and the projectile-target subsystem. The same applies to the initial state wave function except that the electron-target wave function is an initial bound state.

In 1983 Crothers and McCann [96] developed the CDW method within the framework of the semi-classical impact-parameter time-dependent model. In this treatment, the final state is treated in the standard CDW method. On the other hand, the initial state is represented as an Eikonal approximation to the initial-state continuum distorted wave. This method is currently known as the CDW-EIS method (continuum-distorted-wave Eikonal-initial-state). This method gained momentum when Fainstein (1988) [97] extended it to study ionization of multi-electron targets. It was extensively used to study the singly differential and doubly differential cross sections of electron spectra. This method is reviewed by Crothers *et al.* [98].

2.3.2 Binary Encounter Approximation (BEA)

The binary encounter approximation (BEA) is one of the earliest approximations used in describing and studying the ionization process. In this approximation it is assumed that ionization is totally caused by the binary encounter between the charged projectile and the target electron. The target nucleus and the rest of its electrons play no role in the process except for providing the momentum distribution and the binding energy of the ejected electron.

This theory dates back to the pioneering work of Thomson in the early 1912. He used the results of the Rutherford scattering theory to calculate the singly differential cross section of electron ejection. He assumed the the target electron was at rest before the collision. This theory was improved in 1927 by Williams and Thomas who took account of the electron initial velocity. Rudd *et al.* extended the theory in 1971 [76] by using a quantum-mechanically derived velocity distribution for the target electron. Further extension of the theory was made by Bonsen and Vriens in 1970 [77] by calculating doubly differential cross sections (in angle and ejected electron energy). It is worth noting that in this approximation the total cross section has an asymptotic behavior that goes as $1/E$ instead of the well established $(1/E)lnE$, where E is the projectile energy. A review of this theory was given by Rudd and Macek [78] and E. J. Mansky [79].

2.3.3 Classical-Trajectory Monte Carlo Method (CTMC)

This method was introduced into ion-atom collision studies by Abrines and Percival [80, 81] in 1966. They used classical mechanics to study electron capture and ionization in the collision p + H at intermediate velocity. Since then, this method was extensively used by many authors to study different inelastic processes

including ionization [20,26,82-86]. In this method the classical equations of motion are solved explicitly. The initial target electron is represented by spatial and momentum distributions that are calculated quantum mechanically. The target core ion is described by a model potential such as a screened Coulomb potential. The independent-electron model [87, 88] is used for many-electron atoms. The impact parameter and the initial position and momentum of the target electron are chosen randomly. Different reaction channels are identified by looking at the final states (position and momentum of the three collision products) when the collision partners are infinitely separated. The procedure is repeated for a large number of trajectories ($\sim 10^5 - 10^7$). The cross sections are determined statistically from the number of events that lead to each channel.

Utilizing the rapid development in computers, Olson in 1987 [89] developed the method by directly including all the electrons on the target atom. This method was called the n-body CTMC (nCTMC). In this theory the interactions between projectile ion, target ion and all target electrons are taken into consideration. The electron-electron interaction is not included in the equation of motion.

A strong advantage of this technique is that it includes interactions between the ejected electron and both Coulomb centers. In addition it allows us to calculate the momentum distribution of all the collision products. This makes it possible to calculate the impact parameter dependence of any inelastic process, the scattering angle of the projectile, and the energy loss (gain) by the projectile. Full information can be obtained about recoil ions [56]. For this reason the CTMC method has accompanied the recoil ion momentum spectroscopy development since its early days until now. The CTMC method gives the best results at intermediate velocities. Like the binary encounter approximation it has an asymptotic behavior of $(1/E)$ rather

than $(1/E)lnE$.

2.4 Theory of Slow Atomic Collisions

When the velocity of the projectile v_p is comparable to or less than the bound electron velocity v_o, a transient molecule is formed during the collision which plays a major role in determining the inelastic processes that take place, including excitation, charge transfer and ionization. The two nuclei come close to each other and there is enough time that the target-atom electron is shared temporarily by both nuclei. In this regime, any perturbative treatment of the collision is expected to give poor results due to the strong interaction between the projectile ion, target atom, and the target-atom active electron. The need for rigorous quantum nonperturbative treatment then arises. One commonly used approximation in this velocity range is the so called "semi-classical approximation", the electronic motion whereby is described quantum mechanically while the nuclear motion is described classically.

2.4.1 Adiabatic and Diabatic Representations

For simplicity, let us consider a bare ion (Z_1) colliding with a hydrogen-like-atom (with a nuclear charge Z_2). Fig. 2.1 shows the center-of-mass coordinate system. In this coordinate system, one can write the Hamiltonian,

$$H = -\frac{1}{2\mu}\nabla_R^2 + \frac{Z_1 Z_2}{R} - \nabla_r^2 - \frac{Z_1}{r_1} - \frac{Z_2}{r_2} \quad , \tag{2.2}$$

where μ is the reduced mass of the two nuclei [99]. This Hamiltonian can be separated into nuclear part (T_R) describing the (slow) motion of the nuclei and an electronic part (H_{el}) describing the (fast) motion of electrons,

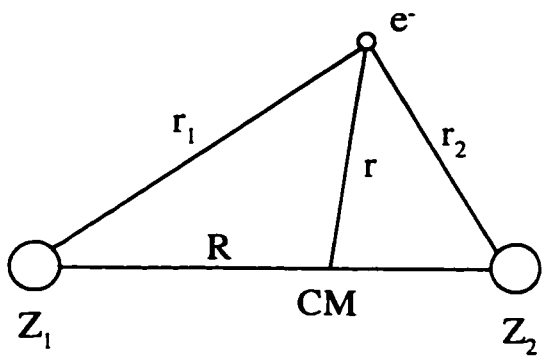

Figure 2.1: Coordinate system used to describe the collision of a bare ion Z_1 with hydrogen-like atom (with a nuclear charge Z_2).

$$T_R = -\frac{1}{2\mu}\nabla_R^2 \quad , \tag{2.3}$$

$$H_{el} = \frac{Z_1 Z_2}{R} - \nabla_r^2 - \frac{Z_1}{r_1} - \frac{Z_2}{r_2} \quad . \tag{2.4}$$

The time-independent Schrödinger equation is

$$H\Psi = (T_R + H_{el})\Psi = E\Psi \quad . \tag{2.5}$$

The total wave function Ψ can be expressed in terms of an orthonormal basis set of electronic wave functions $\phi_i(R, \mathbf{r})$,

$$\Psi = \sum_i F_i(\mathbf{R})\phi_i(R, \mathbf{r}) \quad . \tag{2.6}$$

Substituting Eq. 2.2 and Eq. 2.6 in Eq. 2.5 and making use of the orthonormality of the basis set $\phi_i(R, \mathbf{r}) \equiv |i>$, we get the set of coupled equations

$$[T_R + < j|H_{el}|j > -E]F_j(\mathbf{R}) = -\sum_{i \neq j}[< i|H_{el}|j > -\frac{1}{\mu} < i|\nabla_{\mathbf{R}}|j > \cdot\nabla_{\mathbf{R}}]F_i(\mathbf{R}) \quad , \tag{2.7}$$

where we neglected the second order terms.

The left hand side of Eq. 2.7 represents the elastic scattering in the j channel for a collision energy E. The right hand side contains the coupling terms which induce electronic transitions between the channel $|j>$ and the other channels $|i>$. The term $< i|H_{el}|j > \equiv \varepsilon_{ij}$ is usually called the *electronic coupling* term and $< i|\nabla_{\mathbf{R}}|j > \cdot\nabla_{\mathbf{R}}$ is the *dynamic coupling.*

In order to use Eq. 2.7 in calculations for inelastic processes, one must use a suitable basis function $\phi_i(R, \mathbf{r})$ that has the correct asymptotic behavior (as the two atoms are infinitely separated). If the molecular orbitals (MOs) are chosen as a basis, then

$$< i|H_{el}|j > = \varepsilon_{ij}(R)\delta_{ij} \equiv \varepsilon_j^A(R) \quad . \tag{2.8}$$

Then Eq. 2.7 reduces to

$$[T_R + \varepsilon_j^A(R) - E]F_j(\mathbf{R}) = -\sum_{i \neq j} \frac{1}{\mu} < i|\nabla_{\mathbf{R}}|j > \cdot\nabla_{\mathbf{R}} F_i(\mathbf{R}) \quad , \tag{2.9}$$

Therefore, in this representation only dynamical coupling exists between different channels. This representation is referred to as the *adiabatic representation* as it inherently allows the electronic cloud to adapt to the slowly moving nuclei.

On the other hand, one may choose a basis set functions $\phi_i(\mathbf{r})$ that do not depend on R. These can be atomic orbitals (AO), for instance. In this case only the electronic coupling will contribute. $\varepsilon_{ij}(R)$ will no longer be diagonal

$$< i|H_{el}|j >= \varepsilon_{ij}^{D}(R) \qquad , \tag{2.10}$$

and Eq. 2.7 is rewritten as

$$[T_R + \varepsilon_j^D(R) - E]F_j(\mathbf{R}) = -\sum_{i \neq j} \varepsilon_{ij}^D(R) F_i(\mathbf{R}) \qquad . \tag{2.11}$$

Such representation is usually called *Diabatic representation.* Details and reviews of adiabatic and diabatic representations can be found for example in the following references [100-105].

2.4.2 Dynamical Coupling

To achieve a physical meaning of the *dynamical coupling* term derived in the previous section, we can write a time-dependent version of the expansion shown in Eq. 2.6

$$\Psi(t, \mathbf{R}, \mathbf{r}) = \sum_i a_i(t) \chi_i(\mathbf{R}, \mathbf{r}) \qquad . \tag{2.12}$$

The time-dependent Schrödinger equation therefore reads

$$i\frac{\partial}{\partial t}\Psi(t, \mathbf{R}, \mathbf{r}) = H\Psi(t, \mathbf{R}, \mathbf{r}) \qquad . \tag{2.13}$$

Applying Eq. 2.12 in Eq. 2.11 and making use of the orthonormality of the basis χ_i, one will get the set of coupled equations:

$$i\frac{d}{dt}a_j = \sum_i < \chi_j|H - i\frac{\partial}{\partial t}|\chi_i > a_i(t) \qquad , \tag{2.14}$$

Again the term $< \chi_j|H|\chi_i >$ contains the electronic coupling. The dynamical coupling is contained in the term $< \chi_j| - i\frac{\partial}{\partial t}|\chi_i >$. In an arrangement where the scattering plane is defined to be the xz plane, the operator $\frac{\partial}{\partial t}$ can be rewritten as

$$\frac{\partial}{\partial t} = \frac{dR}{dt}\frac{\partial}{\partial R} + \frac{d\theta}{dt}\frac{\partial}{\partial \theta} = v_R \frac{\partial}{\partial R} + \frac{v_p b}{R^2} i L_y \quad , \tag{2.15}$$

where θ is the angle of rotation of the internuclear axis, b is the impact parameter, v_p is the initial projectile velocity, v_R is the radial velocity, and $L_y = -i\partial/\partial\theta$ is the angular momentum perpendicular to the collision plane.

Accordingly, the dynamical coupling term can be rewritten as:

$$< \chi_i | \frac{\partial}{\partial t} | \chi_j >= v_R < \chi_i | \frac{\partial}{\partial R} | \chi_j > + \frac{v_p b}{R^2} < \chi_i | i L_y | \chi_j > \quad , \tag{2.16}$$

The term $v_R < \chi_i | \frac{\partial}{\partial R} | \chi_j >$ is called the *radial coupling* term. It couples molecular states that have the same projection of angular momentum on the internuclear axis. This projection is represented by the quantum number m. This can be be rephrased by stating that the radial coupling term couples molecular states for which $\Delta m = 0$ (for example $\sigma \leftrightarrow \sigma$ or $\pi \leftrightarrow \pi$). The other term, $\frac{v_p b}{R^2} < \chi_i | i L_y | \chi_j >$ is called the *rotational coupling* term. It couples molecular states that are different by $\Delta m = \pm 1$ (for example $\sigma \leftrightarrow \pi$ or $\pi \leftrightarrow \delta$). For more details about molecular orbitals you can refer to standard atomic physics textbooks, for example *Physics of Atoms and Molecules* by Bransden and Joachain [106].

One can think of the rotational coupling as a geometrical effect that results from the rotation of the internuclear axis. During the collision, the internuclear axis rotates with respect to a space fixed frame. Therefore the molecular orbitals have to rotate also. However, they have an inertial tendency to keep their orientation fixed. This can result in a change of their symmetry (with respect to the internuclear axis) during the course of collision. The radial coupling arises from the tendency of the molecular orbits to keep their position in space [107].

2.4.3 Correlation Diagrams

As discussed earlier one can treat slow collisions in a molecular basis. It assumes the formation of a transient molecule during the collision. Two limiting cases must be considered. When the two atoms are infinitely separated (either before the two atoms approach each other or after they do) we have the *separated atoms* (SA) limit. When (theoretically) the two nuclei overlap to form, and the electrons of the two atoms are shared by, the *united atom*, we have the *united atom* (UA) limit.

During the transition between the SA limit and the UA limit, molecular orbitals are formed. Due to symmetry considerations, atomic orbitals in the SA limit evolve to certain molecular orbitals at intermediate internuclear distances and finally to specific atomic orbitals in the UA limit. This kind of correspondence is usually represented by molecular orbital *correlation diagrams*. In addition some of these diagrams involve an energy absolute scale which shows how the energy of a certain atomic/molecular orbital changes as the internuclear distance changes.

For the purpose of illustration and for use in later discussions, we show in Fig. 2.2 two correlation diagrams. The diagram in Fig. 2.2(a) represents a homo-nuclear diatomic molecule while the diagram in Fig. 2.2(a) represents a slightly asymmetric heteronuclear diatomic molecule. It should be noted that, in these diagrams, the energy is not to scale and varies from one molecule to another. However, the general character and order of states is more general.

2.4.4 Electron Promotion Model and Translational Energy Spectroscopy

By looking at the correlation diagrams in Fig. 2.2, we note that some of the molecular orbitals intersect. At an intersection point, the electron may make a transition

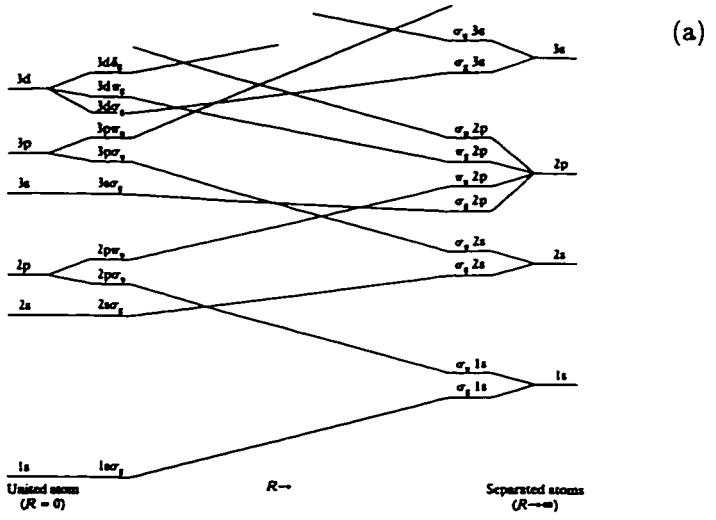

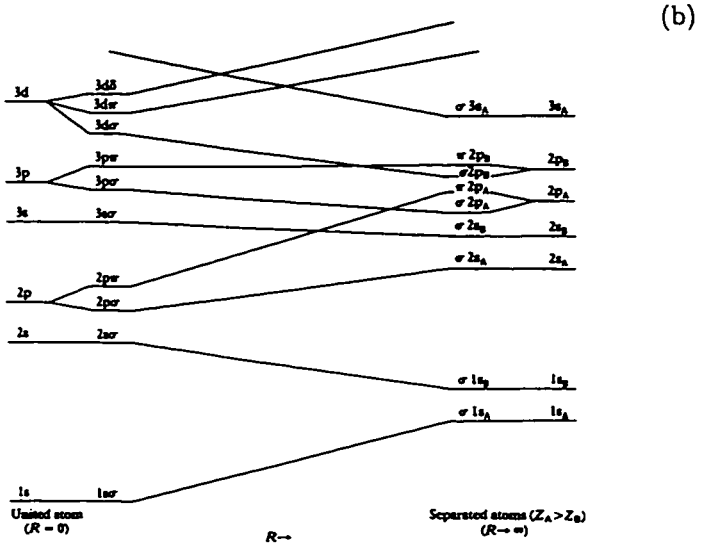

Figure 2.2: Correlation diagrams for (a) homo-nuclear diatomic molecules and for (b) heteronuclear diatomic molecules. The diagrams are not to scale. Energy levels vary from a molecule to another. (adapted from Bransden and Joachain [106]).

from its original level to the other level. Rotational and radial couplings (section 2.4.2) are the major coupling mechanisms between different adiabatic levels. The transition probability depends on the details of the intersection and can be treated by different models such as, for example the Landau-Zener model [101]. As the electron makes a transition from one orbital to another it is said to be promoted. Promotion processes can happen while the two atoms are approaching each other or while they are receding from each other.

The electron promotion model was first suggested by by Fano and Lichten [108] in 1965. It was successfully used in explaining the L inner shell vacancy formation in the collision of Ar^+ with Ar [75]. A correlation diagram of the Ar-Ar system, shows a very sharp rise in the molecular orbital $4f\sigma$ at an internuclear distance $R \simeq 0.25$ Å while the two atoms are approaching each other. An electron in the L level is promoted through this molecular orbital to a higher level or to the continuum leaving an L-level vacancy. This vacancy may later be filled by a higher level electron resulting in an X-ray or Auger-electron emission.

The molecular promotion model was very successful in explaining inelastic processes in low velocity collisions. It received a great deal of attention as a result of major developments in experimental techniques employed in the 1960's and 70's. Electrostatic analysis spectrometers and time-of-flight spectrometers were developed to measure the energy loss (Q-value) and scattering angles of slow projectiles ($\sim$ 100 ev - 10 keV). These differential measurements allowed researchers to identify different mechanisms involving different electronic subshells. Angular distributions of the scattered projectiles were crucial in studying the impact parameter dependence of various processes.

Two major reasons limited these studies to such low collision energies. First, the

required energy resolution and angular resolution become prohibitive with increasing projectile energy. Second, it was expected that the molecular model would fail when the projectile velocity became comparable to the "classical" electron orbital velocity.

Most of the studies based on the molecular promotion model focused on the processes of excitation and charge exchange [110-117]. It was suggested by several authors [114,116,118,119] that ionization in slow collisions could be treated based in the molecular promotion model as well.

For the sake of illustration and comparison with the results reported in chapter 4, we review excitation and ionization processes in the two systems He^+ + He and He + He. A schematic correlation state diagram of the system He^+ - He adapted from Barat *et al.* [114] is given in Fig. 2.3. The major inelastic process happens via the rotational coupling of the two states A $\rightarrow$ C in Fig. 2.3 due to the underlying rotational coupling of one $2p\sigma$ electron to a $2p\pi$ orbital. This coupling leads mainly to target excitation ($1s^2 \rightarrow 1s2p$). Another rotational coupling leads to different excitation, transfer, and projectile ionization channels but not to target ionization. In Fig. 2.3, this coupling happens between line F and the lines G, H, and J. These different channels can be identified in an energy loss spectrum. Such a spectrum is shown in Fig. 2.4. This figure is adapted from Gerber *et al.* [115]. It is noted that in addition to the elastic scattering peak at Q = 0, the spectrum is dominated by target single excitation, target single excitation plus projectile excitation and target double excitation. The two main peaks centered at Q = 21 eV and 61 eV have tails that extend to reach the ionization threshold. Due to the dominance of excitation over ionization, no estimation can be given to the nature of the ionizing events. One expects that ionization can happen via the following two routes: radial coupling of the Σ_g state with the continuum states of the same symmetry, and rotational

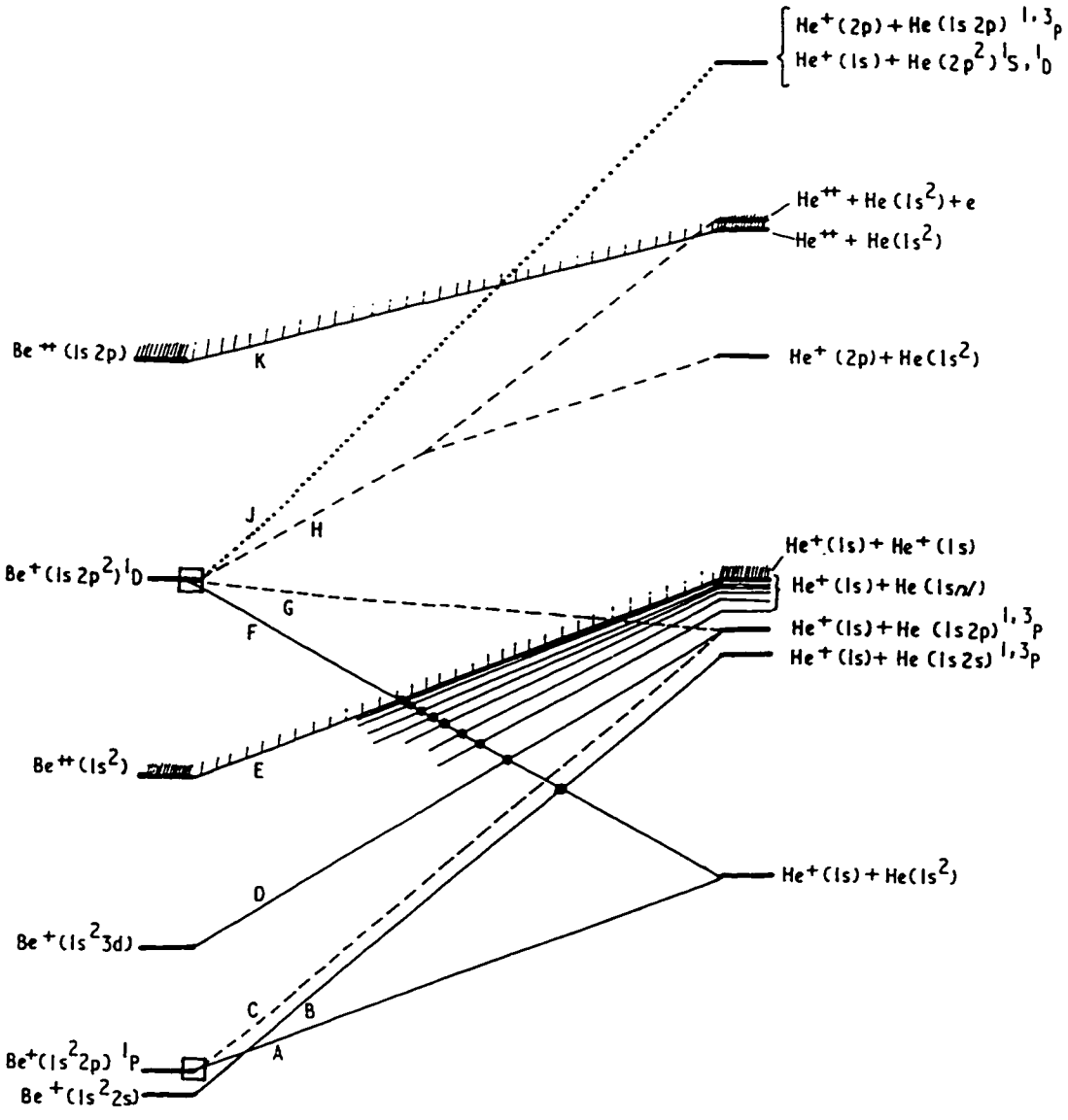

Schematic correlation diagram for the He^+-He system. A, $\{(1s\sigma_g)^2(2p\sigma_u)\}\ ^2\Sigma_u$; B, $\{(1s\sigma_g)^2(2s\sigma_g)\}\ ^2\Sigma_g$; C, $\{(1s\sigma_g)^2(2p\pi_u)\}\ ^2\Pi_u$; D, $\{(1s\sigma_g)^2(3d\sigma_g)\}\ ^2\Sigma_g$; E, $\{(1s\sigma_g)^2\}\ ^1\Sigma_g$ (of He_2^{2+}); F, $\{(1s\sigma_g)(2p\sigma_u)^2\}\ ^2\Sigma_g$; G, $\{((1s\sigma_g)(2p\sigma_u)\ ^3\Sigma_u)(2p\pi_u)\}\ ^2\Pi_g$; H, $\{((1s\sigma_g)(2p\sigma_u)\ ^1\Sigma_u)(2p\pi_u)\}\ ^2\Pi_g$; J, $\{(1s\sigma_g)(2p\pi_u)^2\}\ ^2\Delta_g$; K, $\{(1s\sigma_g)(2p\sigma_u)\}\ ^1\Sigma_u$ (of He_2^{2+}). ——Σ states; - - - - - Π states; $\cdots$ Δ states. Curve crossings where radial coupling induces inelastic transitions are marked by ●; those where rotational coupling occurs are marked by □.

Figure 2.3: Schematic correlation diagram for the He^+ - He system (Adapted from Barat *et al.* [114]).

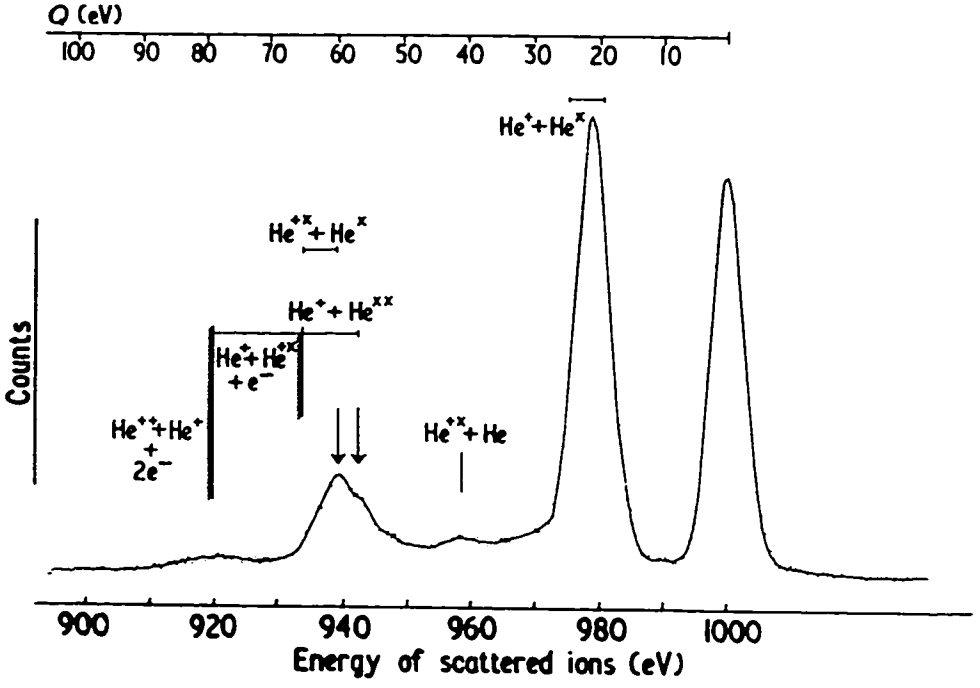

Figure 2.4: Spectrum of scattered He^+ ions obtained for 1 kev He^+ + He collisions at $\theta = 8°$ detection angle. (Adapted from Gerber *et al.*[115]).

coupling ($\Sigma_g \rightarrow \Pi_g$, $\Sigma_u \rightarrow \Pi_u$) leading to autoionizing states. Since electrostatic analysis of the projectile He^+ will include both events of excitation and events of target ionization, a coincidence experiment is needed to separate ionization process. To our knowledge no such experiment was done for this system.

However, in the collision of He + He , one will automatically separate ionization events if the projectiles that lost one electron (He^+) are energy analyzed. This was done by Barat *et al.* [114]. Fig. 2.5 shows some energy loss spectra for the ionized projectiles (He $\rightarrow$ He^+). The spectrum consists of two main peaks. The first peak corresponds to single ionization with no excitation. Note the asymmetric shape of this peak which can be explained as a result of the ejected electron energy distribution. The second peak corresponds to single projectile ionization accompanied by target excitation. The second peak is broad due to the presence of many excitation channels.

Angular distributions of scattered ions of the same system for three different velocities are presented in Fig. 2.6. The distributions are given in terms of the reduced scattering angle $\tau = E\theta$. Note that ionization accompanied by excitation is associated with large scattering angles and therefore happens at smaller impact parameters relative to those for ionization with no excitation. These results can be compared directly to the results that are presented in chapter 4 using the COLTRIMS technique and at relatively higher energies.

Finally we mention a set of experiments were carried out by Gerber *et al.* [115, 121] to measure ejected electron energy distributions in the collisions of the symmetric systems of He, Ne, Ar, and Kr. In addition, the collisions of He and He^+ with Ne, Ar, Kr, and Xe were studied. The observed Auger peaks were interpreted successfully in terms of molecular orbitals. The results agreed very well with the re-

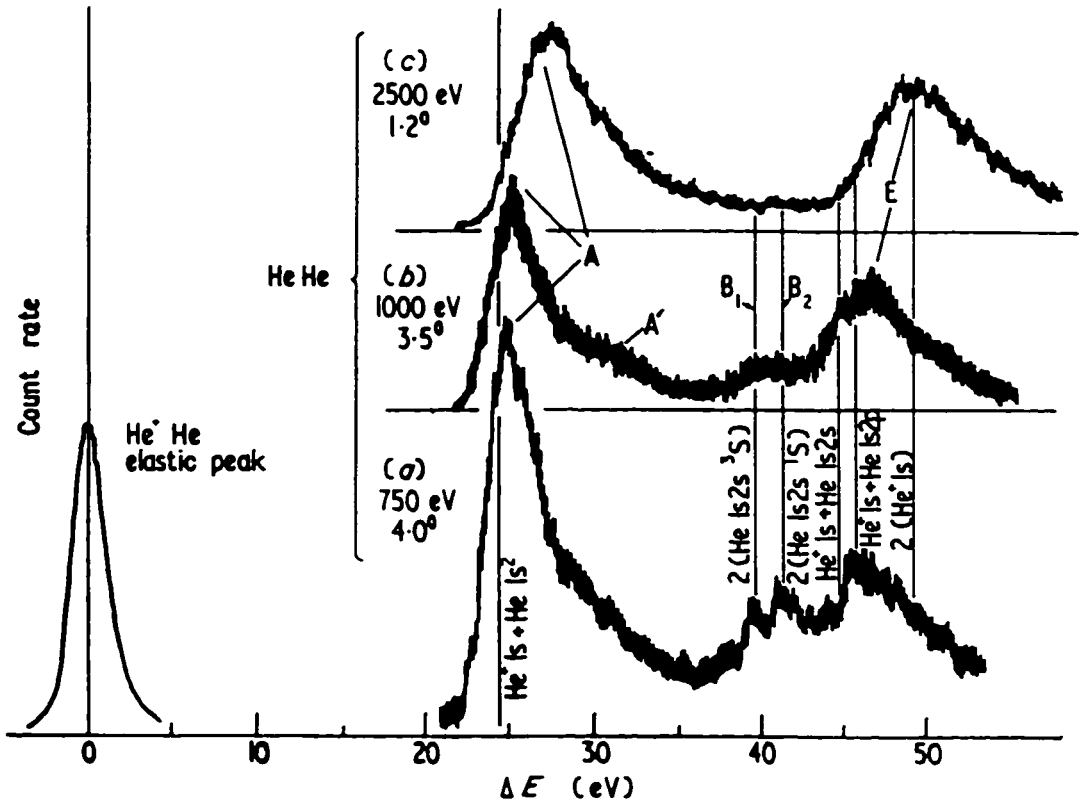

Figure 2.5: Energy loss spectra of the scattered ions He^+ at some incident energies and scattering angles for the collision system He + He. (Adapted from Barat *et al.*[114]).

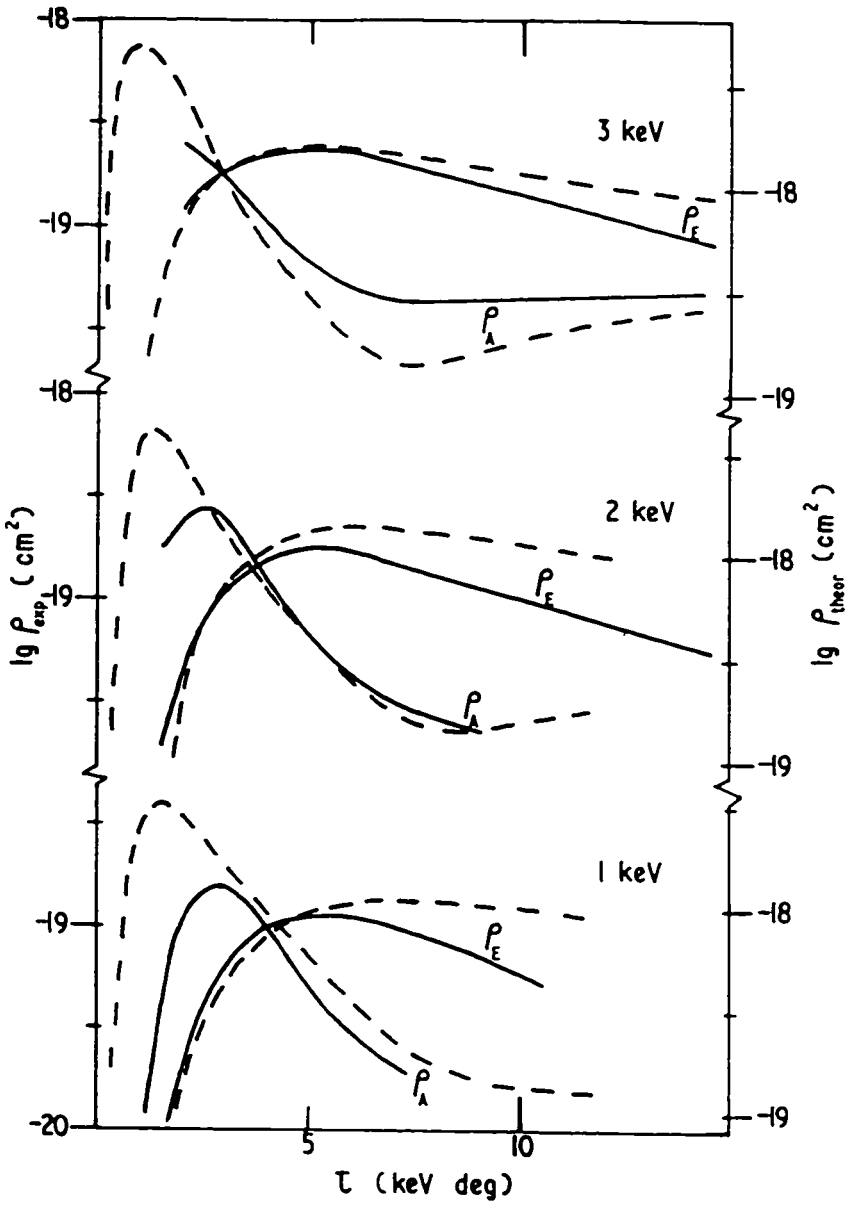

Figure 2.6: Angular distributions of the scattered ions (He^+) in low energy collisions of He + He. The subscripts A and E refer to the two peaks in Fig. 2.5. Solid lines are experimental and the dashed lines are theoretical calculations based on the rotational coupling model. (Adapted from Barat *et al.*[114].

sults of the Q-value distributions obtained using translational energy spectroscopy. However these peaks formed a small fraction of the total cross section. The major part of the distribution was near ejected electron energy $E = 0$. Studying these electrons in detail was not achievable due to different problems that we discussed earlier.

2.5 Theory of Hidden Crossings

This theory started to emerge in the beginning of the last decade as an extension of the adiabatic theory. It is still being developed by several researchers to deal with different inelastic processes. Of a special interest is the ionization process. The basic idea in this theory is extending the internuclear distance to be a complex quantity. This results in potential curves crossings in the complex plane of R. Those crossings are referred to as *hidden crossings*. A transition between different adiabatic states happens at these hidden crossings. Upon finding the hidden crossings the total cross section and doubly differential cross sections can be calculated.

For the purpose of illustration, we give a short and elementary explanation of the basics of this theory. More details can be found elsewhere [31-37]. For simplicity let us assume two diabatic potential curves $U_1(R) = E_o + \alpha R$ and $U_2(R) = E_o - \alpha R$. The two levels interact via a potential W which is independent of R (as in Landau-Zener model). The corresponding adiabatic energy levels are

$$E_1(R) = E_o - \sqrt{(\alpha R)^2 + W^2} \quad , \tag{2.17}$$

$$E_2(R) = E_o + \sqrt{(\alpha R)^2 + W^2} \quad . \tag{2.18}$$

These two curves pseudo-cross at the intersection point of the diabatic levels. In the complex plane of R, $E_1 = E_2$ at the two branch points $R_c = \pm\frac{i}{\alpha}W$. Near the branch points R_c, the energy difference between the two adiabatic states is

$$\Delta E(R) = E_1(R) - E_2(R) \approx A\sqrt{R - R_c} \quad , \tag{2.19}$$

where A is a constant. Upon moving around a branch point R_c, states are switched. In general, the transition probability between the two states E_1 and E_2 is given by

$$P = \exp\left(-\frac{2Q_M}{v_p}\right) \quad , \tag{2.20}$$

where v_p is the collision velocity. Q_M is a Massey-type parameter and is given as a contour integral in the complex plane:

$$Q_M = \left| Im \int_{Ret(R_c)}^{t(R_c)} \Delta E(R(t)) v_p dt \right| \quad , \tag{2.21}$$

where the time t is introduced in a semi-classical way by taking a classical trajectory of the nuclear motion.

Different types of hidden crossings were identified. Of main interest in studying the ionization process and most of the inelastic processes are those two groups of hidden crossings associated with the T and the S series of branch points. These series were denoted by S_{NLM} and $T_{n1,n2,m}$ where N, L, M are the spherical quantum numbers and $n1, n2, m$ are the parabolic quantum numbers. The S series was found analytically by Solov'ev [122] in 1981. This series is associated with transitions while moving from the SA limit to the UA limit. Therefore electron promotion to the continuum happens via this process (S process) while the two nuclei are approaching each other. The T-type of hidden crossings were revealed through numerical calculations by Ovchinnikov and Solov'ev [37] in 1986. In this type of

hidden crossings, electrons are promoted to the continuum while the two nuclei are receding from each other. The T process is the equivalent of the (classical) saddle point ionization mechanism.

To illustrate these processes, we discuss the hidden crossings in the simplest atomic collision system, namely $H^+ + H$. A detailed study of this system within the framework of the theory of hidden crossings was carried out by M. Pieksma [123]. The two types of hidden crossings for this system are shown in Fig. 2.7 and Fig. 2.8. You can notice that the S-type crossings lead to continuum while the two centers are approaching each other. On the other hand the T-type crossings lead to the continuum while they are departing from each other. Fig. 2.9, illustrates the spiral-shape surface leading from one level to another by moving around a branch point.

As will be discussed further later, either of these processes could lead to low-energy ionization. However, as will be shown from our data, the more important process appears to be initiated by a $2p\sigma - 2p\pi$ coupling at small internuclear distances, followed by a T-promotion along a π-type series similar to the σ-type series shown in Fig. 2.8.

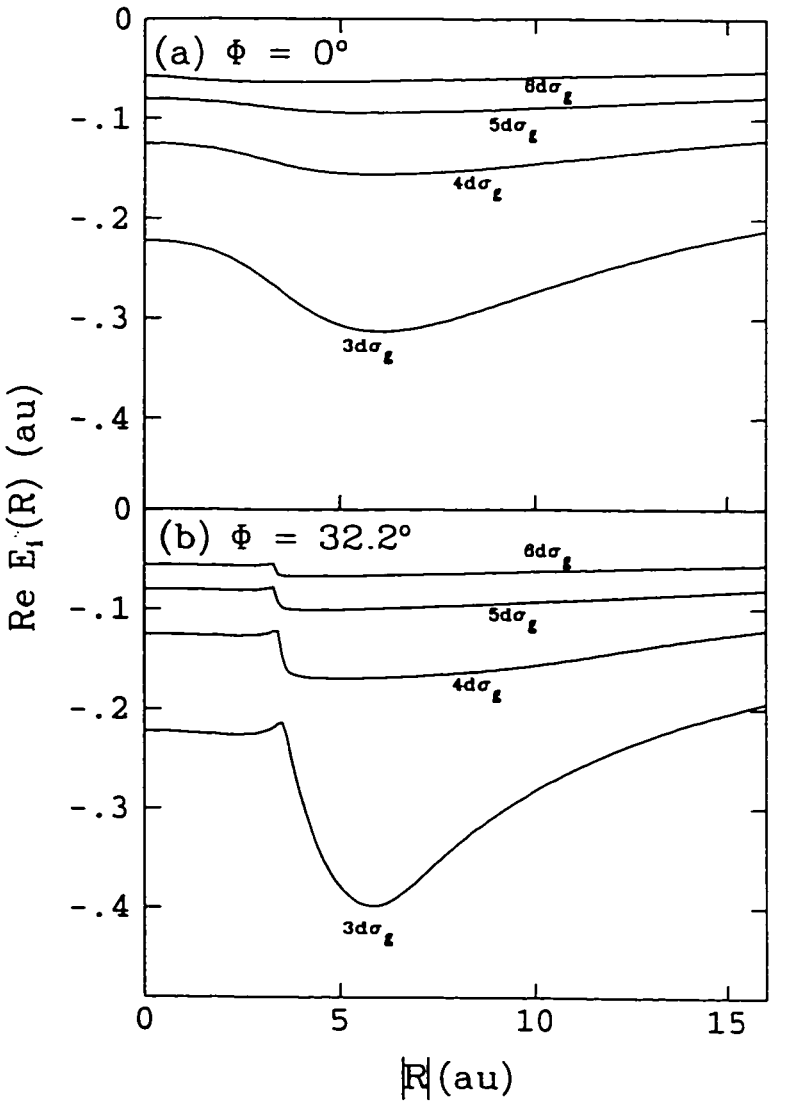

Figure 2.7: Potential energy curves for H_2^+ quasi-molecule. (a) along the real axis ($\Phi = 0°$) and (b) along an axis in the complex plane which makes an angle $\Phi = 32.2°$ with the real axis. The S-type hidden crossings can be seen in (b). (Adapted from M. Pieksma [123]).

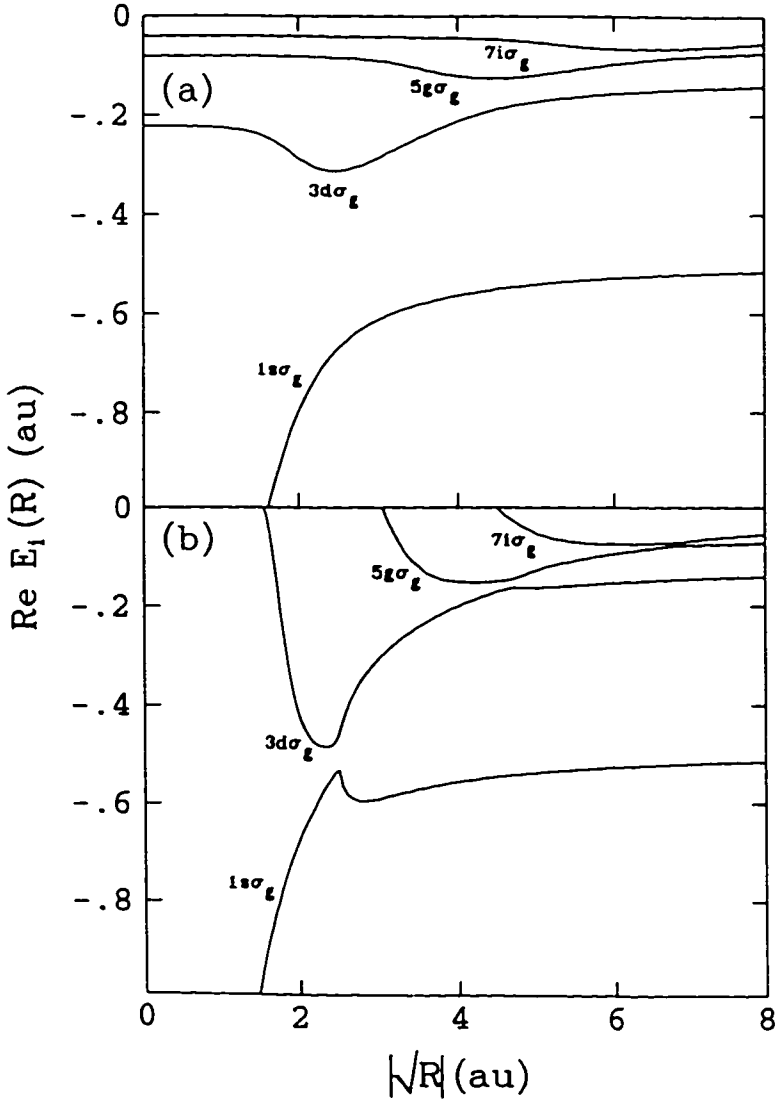

Figure 2.8: The same as Fig.2.7, but in the complex $R^{1/2}$ plane instead of the plane of R. T-type hidden crossings of the potential curves can be seen. In (a) potential curves are plotted along the real $R^{1/2}$ axis. In (b), the path is taken along a straight line path that passes close to successive T branch points. (Adapted from M. Pieksma [123]).

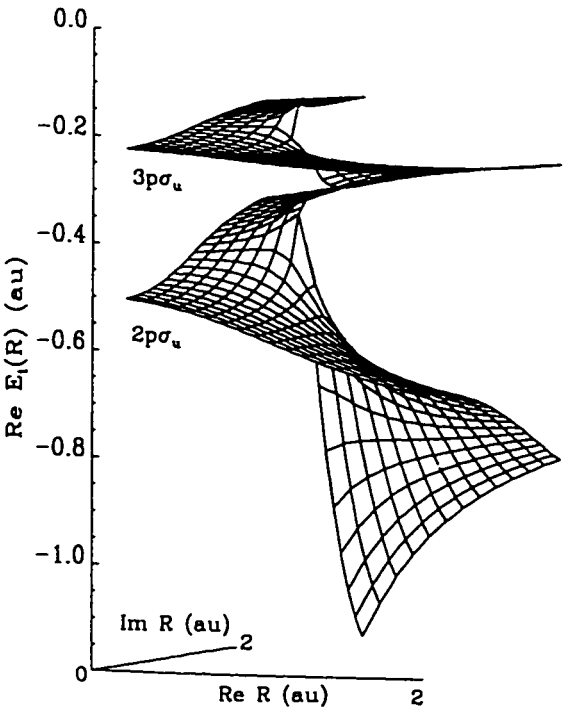

Figure 2.9: Real part of the potential energy as a function of the complex internuclear distance R for two levels connected by an S-type branch point. (Adapted from M. Pieksma [123]).

Chapter 3

Electron Momentum Imaging

As discussed in the introduction, the position of the saddle point changes while the two Coulomb centers are receding from each other. The saddle point velocity (v_{sp}) in the laboratory frame, where the target initially is at rest, is given by the equation

$$v_{sp} = \frac{v_p}{1 + \sqrt{q_p/q_t}} \quad , \tag{3.1}$$

where v_p and q_p are the projectile velocity and charge state, respectively. q_t is the target-charge state. An electron distribution centered on the saddle point will have a projectile velocity and charge-state dependence that agrees with Eq. 3.1. This chapter is devoted to studying the velocity and projectile charge-state dependence of the ejected electron momentum distributions. First, we will study the collision system p + He over a range of projectile velocity v_p = 0.63 - 2.39 a.u. The system C^{6+} + He is then studied over a range v_p = 1.16 - 1.63 a.u. Then we study the projectile charge-state dependence at v_p = 1.63 a.u. In this study we use the bare ions p, He^{2+}, C^{6+}, O^{8+}, and Ne^{10+} as projectiles and He and Ne as targets.

3.1 Experimental technique

3.1.1 Experimental Setup

All of the experiments discussed in this dissertation were carried out at the KSU CRYEBIS facility [124-126]. It is a very powerful ion source capable of producing highly charged ions with energy up to 150 keV per charge. A description of this type of ion source and its operation is given, for example, by E. D. Donets [127]. In our experiments we used ion beams with currents ranging from 0.2 to 2 nAmps. The ion beam was collimated to 0.5 mm in the collision area by two 4-jaw slits. One of these slits was located after the acceleration column and the other was in front of the entrance to the collision chamber. Target atoms were supplied as a nonlocalized diffusive gas entering the collision chamber through a 0.5-mm pinhole. Pressure in the collision area was kept in the range of 1 - 2 $\times$ 10^{-6} torr to maintain single collision conditions.

The main part in the experimental setup is the time-of-flight-position spectrometer which was designed and built for this experiment. Fig. 3.1 shows a schematic sketch of this spectrometer. A uniform electric field of 420 V/cm was generated by a stack of thin copper plates connected to a chain of resistors. The thickness of the plates was 1 mm while the gap between every two adjacent plates was 3.4 mm. The two ends of the resistor chain were connected to two high-voltage power supplies. The spectrometer axis was positioned perpendicular to the projectile-ion beam. Ejected electrons were accelerated in the direction of increasing positive electric field through a distance of 3.8 cm. After exiting the acceleration region they were detected by a two-dimensional position sensitive detector(2d-psd). Ionized target atoms (recoil ions) were accelerated in the opposite direction through a distance

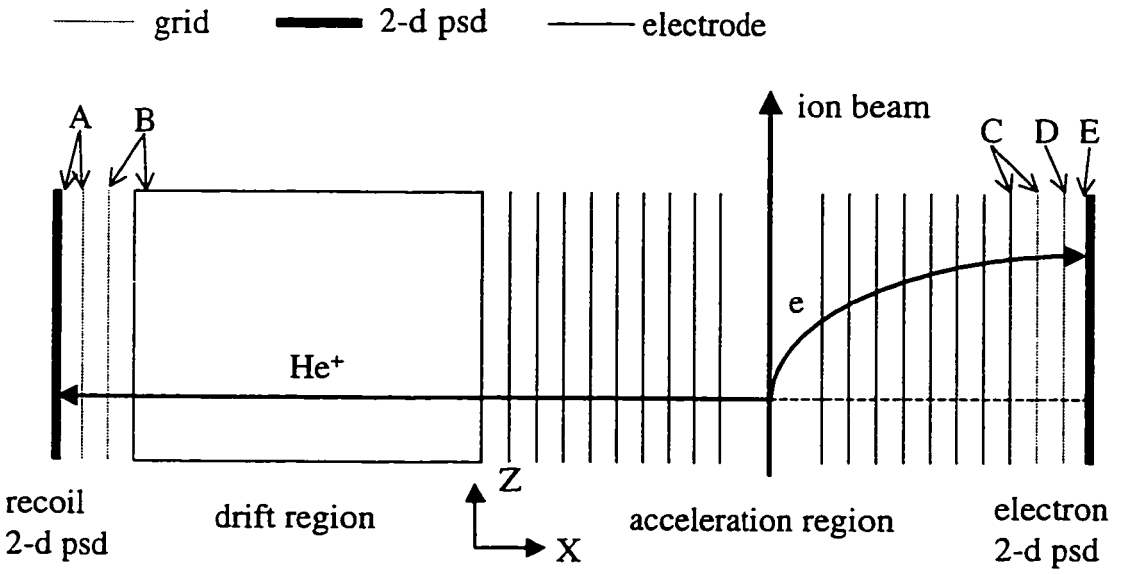

Figure 3.1: Schematic sketch of the time-of-flight-position spectrometer. The plates in the acceleration region are connected together by a resistor chain (not shown) so that a uniform electric field is created. The letters correspond to the following applied potentials: A = -3.02, B = -3.03, C = 0.50, D = 0.25, and E = 0.21 kV.

of 4.5 cm and then entered a field-free drift region of of 7.1 cm, after which they were detected by another 2d-psd. The electron and recoil-ion detectors were identical, using two micro-channel plates with a wedge-and-strip-type anode. For more details about the structure and operation of this type of detector see the dissertations of S. Cheng [128] or M.V. Frohne [129].

To minimize the effect of stray magnetic fields on the ejected electrons, especially at the center of the collision region where electrons are still slow, three sets of perpendicular Helmholtz coils were installed around the collision chamber. Each set of coils generated a magnetic field that is opposite in direction and equal in intensity to the stray field at the center of the collision area along one of the three axes. Stray magnetic fields were kept below 50 mG, which was too small to affect the ejected electrons.

For all experiments, except for experiments with protons as projectiles, the projectile ions were charge analyzed after exiting the collision chamber and were detected by a third 2d-psd. This detector was similar to the electron and recoil-ion detectors except for the anode which was of the resistive-anode type [128, 129].

Fig. 3.2 shows a schematic sketch of the geometry of the experimental setup. The projectile ion beam is taken to be in the positive Z-direction. The extraction field is oriented in the negative X-direction. The electron detector and the recoil-ion detector are facing each other and lie in the YZ-plane. Electrons, recoil ions, and projectiles were detected in a triple-coincidence mode. This means that in order to consider the "event" as a valid event, the three collision products must be detected and registered. The time of flight of the electrons under the large applied electric field was a few nanoseconds. This was three orders of magnitude smaller than the time of flight of the recoil ions and the projectile ions. Therefore, the electron

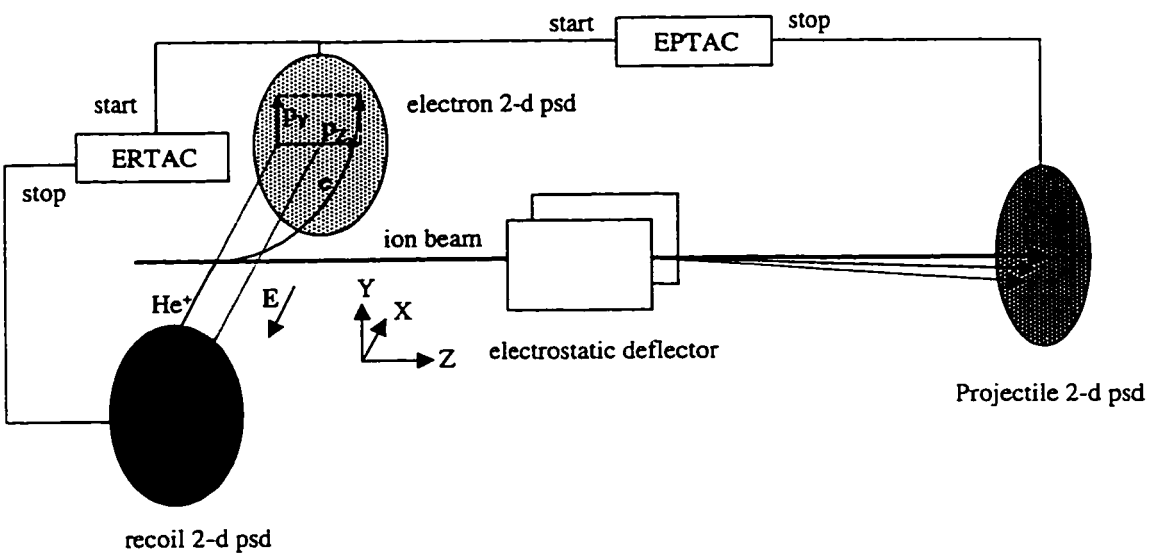

Figure 3.2: Schematic sketch of the experimental setup illustrating the geometry of the three two-dimensional position sensitive detectors (2d-psd) for triple coincidence between the ejected electrons, recoil ions and projectile ions.

detector provided the start signal for the time-to-amplitude converters (TACs) that were used to measure the time of flight of the recoil ions and projectile ions. The following information was recorded for every "valid" event: electron position, recoil-ion position and time of flight, and projectile position and time of flight.

The goal of this experiment was to measure ejected electron momentum distributions in a single ionization process, for example, $C^{6+} + He \rightarrow C^{6+} + He^{+} + e$. There are other processes that can have much larger cross sections and can produce false events, such as single electron capture and transfer ionization. In addition, there are stray electrons that can be generated in the collision chamber in many different ways. The triple coincidence mode in which the experiment was carried out served in minimizing interference with other reaction channels and helped in discriminating against stray electrons. For example, a recoil-ion-time-of-flight distribution will show two peaks corresponding to He^{+} and He^{2+}. This distribution was used to "gate" on He^{+}. On the other hand the projectile detector was used to "gate" on C^{6+} which was separated from other possible charge states by an electrostatic deflector. In addition, a gate was put on the time-of-flight peak of the projectiles. This last gate was necessary to reduce a subtle background from the reaction $C^{6+} + He \rightarrow C^{5+} + He^{+} + h\nu$, where the photon was detected by the electron detector and the C^{5+} ion was not detected. In this situation it is possible to register a C^{6+} from the intense main beam within the strobe time ($\approx$5 μsec) of the data acquisition computer, but less likely for it to occur during the 0.02-μsec-wide electron-projectile time-to-amplitude converter (TAC) peak. For the proton data, only coincidences between the He^{+} recoils and electrons were necessary since other channels, such as electron capture, were less important.

A block diagram of the experimental basic electronics is shown in Fig. 3.3. Ten

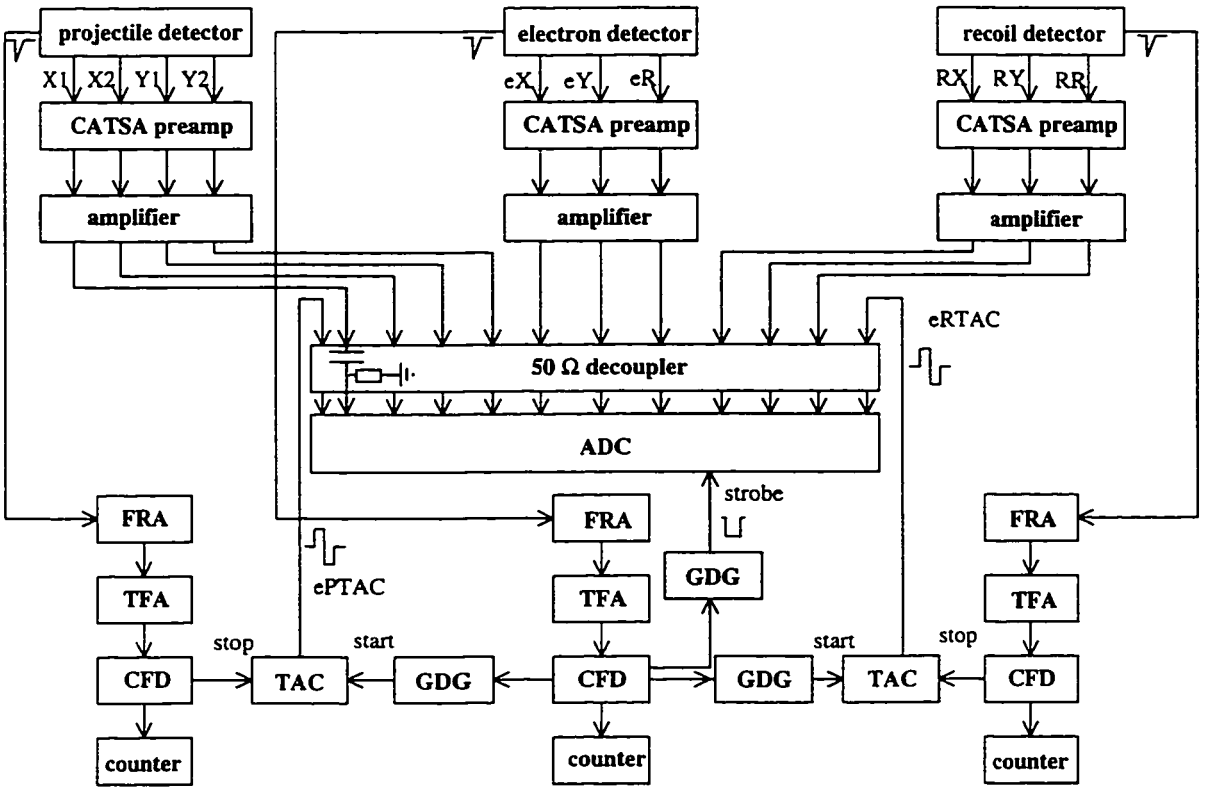

Figure 3.3: Block diagram of basic electronics. These are the used abbreviations: Amp: amplifier, FTA: Fast Timing Amplifier, TFA: Time Filter Amplifier, CFD: Constant Fraction Discriminator, TAC: Time-to-Amplitude Converter, GDG: Gate and Delay Generator, ADC: Analog-to-Digital Converter.

position signals from the three detectors were first amplified by CATSA preamplifiers and then sent to amplifiers for further amplification and shaping. Three of the ten position signals (eX, eY, eR) were from the electron detector, three others from the recoil-ion detector (RX, RY, RR), and four from the (resistive anode)-projectile detector (X1, X2, Y1, Y2). After amplification, the ten signals were sent to an analog-to-digital converter (ADC). The timing signals for the electrons and recoil ions were taken from the the anodes through the CATSA preamplifiers and for the projectile detector from the back of the second channel plate. The time signal of the projectiles was not taken from the anode, since the resistive anode introduces a large spread on the timing signal by about 20 nsec which would strongly affect time resolution. Every one of the three time signals then was amplified by a timing-filter amplifier and then noise discriminated by a constant fraction discriminator and sent to two time-to-amplitude converters (TAC) for which the electron time signal provided the start. The stop signal was provided by the recoil-ion time signal for one (eRTAC) and by the projectile for the other (ePTAC). The output signal of the TACs were also fed to the ADC. The strobe signal was provided by the electron timing signal, as it was the earliest to arrive due to the small time-of-flight of the electrons. Data were taken, stored and analyzed using the JRM micro-VAX computer network. XSYS data acquisition and analysis package [130] was used to take the data and for off-line analyses. A typical analysis code is provided in appendix G. The code supplied in appendix G was used in analyzing data of the experiments reported in chapter 4. However it can be modified to work for any other experiment.

3.1.2 Electron Momentum Calculation

In this experiment the ejected electron momentum distributions (EEMDs) were calculated using the position of the electrons on the electron detector. The recoil ions are born with small energy. They are quickly accelerated by the large electric field and travel in nearly straight line trajectories toward the recoil detector, pinpointing the origin of the ionization event. This position $\mathbf{r}_R$ is subtracted from the position of the electron on the electron detector $\mathbf{r}_e$ to find the absolute position of the electrons $\mathbf{r}_e$-$\mathbf{r}_R$ as shown in Fig. 3.4. For convenience, the Z-component of this resultant vector will be called Z. The Y-component will be called Y. The position (Y,Z) is proportional to the initial Y and Z components of the electron momentum, P_Y and P_Z, respectively. The proportionality constant between position and momentum can be calculated using the known dimensions and electric field in the spectrometer. This constant turns out to be the time of flight of the electrons. Therefore, we can write

$$Y = P_Y t/m \quad , \tag{3.2}$$

and

$$Y = P_Z t/m \quad , \tag{3.3}$$

where t is the time-of-flight of electrons. In a simple case where P_X=0, and electrons are accelerated by the field E to the surface of the channel plate through a distance d, then it is straightforward to show that the time-of-flight of the electrons is given by

$$t = \sqrt{2md/qE} \quad , \tag{3.4}$$

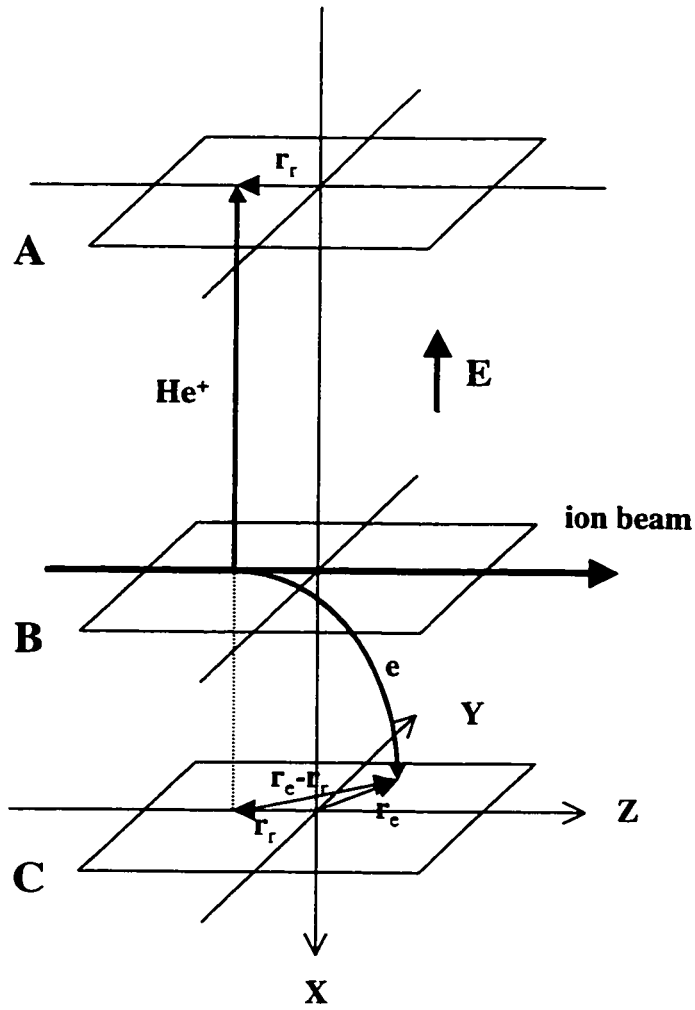

Figure 3.4: Simple geometry illustrating the method used in determining the absolute position of the electrons on the electron detector. The planes **A** and **C** coincide with the recoil and the electron detectors, respectively. The collision takes place in a plane **B** which is parallel to the two detectors surfaces.

where m and q are the mass and charge of the electron respectively. The nonzero value of P_X introduces a small effect on the experimental resolution that will be discussed in the next section. In general, the assumption that electrons have an initial velocity that lies in the plane **B** is very accurate (see section 3.1.3).

The software SIMION [131] was used to simulate the spectrometer and calculate with a good accuracy the proportionality constant t. The simulation took into consideration all details of the electric field and geometry of the system. More details about this simulation are provided in appendix A.

Verification of the calculated constant was accomplished by examination of the $3l3l'$ transfer-ionization channel in C^{6+}+He data. The resulting Auger lines following double capture into the $3lnl'$ states have been measured by Stolterfoht *et al.* [132] and the energy levels of these states have been calculated by Bhalla *et al.* [133]. This channel can be isolated in our experiment by recording electrons in coincidence with C^{5+} and He^{2+} ions. In the corresponding two-dimensional electron- momentum spectra, the Auger lines appear as an annular pattern centered on the projectile velocity as seen in Fig. 3.5(a). In Fig. 3.5(a) the annular pattern is not uniform indicating enhanced forward-backward Auger emission. The diameter of the annular region is twice the known Auger electron momentum. Fig. 3.5(b) is a projection of a small slice (around P_Y=0) of Fig. 3.5(a) on the Z-momentum axis where the location of the electrons emitted from the n=3,n'=3 states can be clearly identified. A peak can be seen in the spectrum centered near a velocity of 2 a.u. One may speculate that this peak could be resulting from autoionization from very high Rydberg states. However, this does not explain the asymmetry of the peak around the projectile velocity. It is obvious from Fig. 3.5 that this peak is, mainly, in the forward direction.

Further confirmation of the conversion factor was obtained by observing the con-

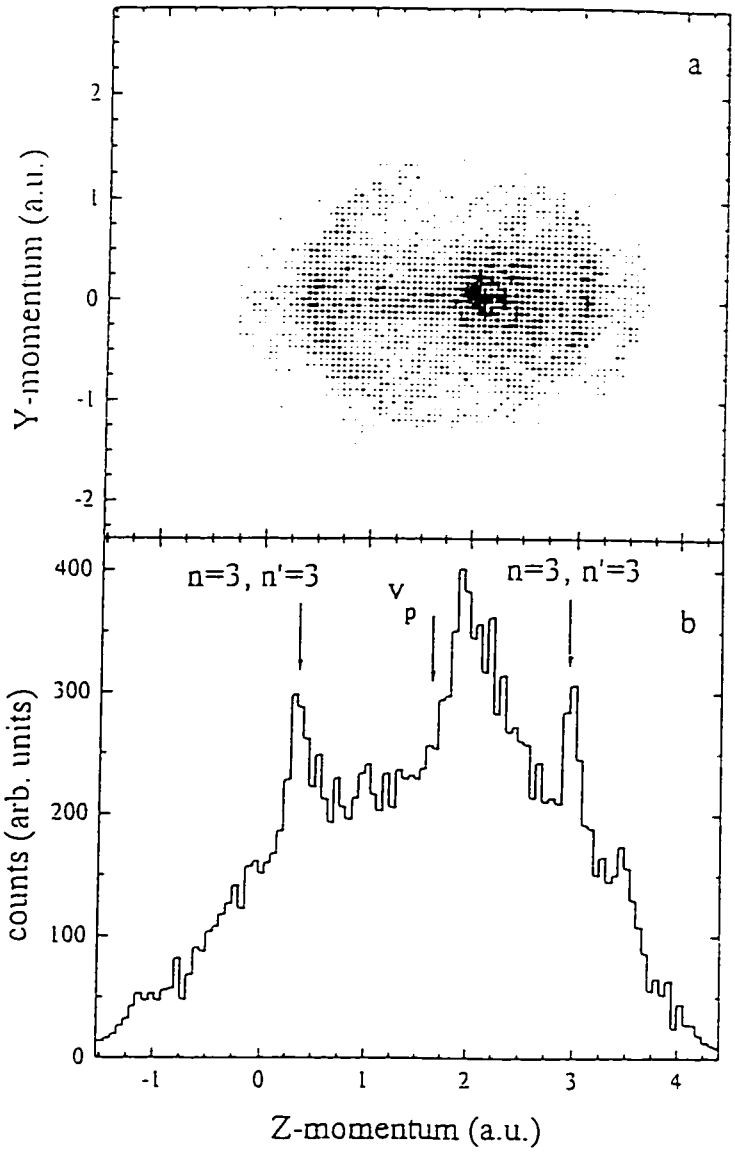

Figure 3.5: Two-dimensional electron-momentum distribution (a), from the transfer ionization channel, used for momentum calibration of the time-of-flight spectrometer.(b) is a projection of a small slice from the center of (a).

tribution of electron capture to the continuum (ECC) process to the ejected electron momentum distributions. The ECC process produces electrons that have the same velocity as the projectile. In the Z-momentum distributions we could see a small hump corresponding to this process marking the accuracy of our calculated conversion factor. We will discuss this process and its contribution to ejected electrons in the forward direction in later sections.

3.1.3 Experimental Resolution

The electron (Y,Z) momentum resolution in this experiment is affected, mainly, by three factors: (1)initial momentum of the electrons, (2) initial momentum of the recoil ions and (3) position resolution of the detectors. The initial momentum of the electrons affects the resolution in the following way. As explained earlier, the (Y,Z) position of each electron is determined by its initial momentum components P_Y and P_Z. The proportionality constant is the time of flight (TOF) of the electron. If an electron is born with $P_X = 0$, then its time of flight t is about 3.4 nsec. It was not possible in our experiment to measure this time with a reasonable accuracy. This left the component P_X undetermined. The unknown, nonzero value of P_X changes the time of flight slightly. That means electrons with the same P_Z will hit the electron detector at slightly different places depending on their P_X component. The error caused by this can be estimated by utilizing the cylindrical symmetry of the emitted electrons around the beam. This means that the final electron-momentum distribution has equal values for P_X and P_Y because of the cylindrical symmetry of the beam. Since P_Y is measured, we can estimate the full width at half maximum of the P_X distribution. In the worst case, corresponding to the widest P_X distribution in the case of protons on He at $v_p = 2.39$ a.u., this FWHM is about 1 a.u. for our

particular geometry and voltages. This will result in an uncertainty in P_Z and P_Y equal to $0.08 \times P_Z$ and $0.08 \times P_Y$, respectively. In the case of C^{6+} on He at v_p = 1.63 a.u., the FWHM of the P_X distribution was about 0.5 a.u. This resulted in a resolution of $0.04 \times P_Z$ and $0.04 \times P_Y$ a.u. in both directions.

In order to decide the origin of the collision (the place in space where the collision happens and electrons are emitted), the recoil ion corresponding to a certain collision was taken as a marker. This will be completely true if the recoil ions are born with zero momentum. However, they have nonzero longitudinal and transverse momentum (with reference to the ion beam). The magnitudes of these momentum components depend on the system and the process under study. In addition, recoil ions have a permanent thermal energy which corresponds to room temperature. The largest longitudinal $P_{\|}$ and transverse $P_{\perp}$ components are expected for the lowest velocity (0.63 a.u.) protons on He. Taking the position of the peak we found that $P_{\|} \sim 1$ a.u. and $P_{\perp} \sim 2.5$ a.u.. This corresponds to an energy of 1.9 and 11.6 meV. Thermal energy at room temperature, $3kT/2$ is about 40 meV. This means that thermal energy is dominant over the energy that the recoil ions receive as a result of the collision. Using the known geometry of the spectrometer and the applied electric field, the error caused by this uncertainty is estimated to be about 0.08 a.u. in electron momentum.

The position resolution of both detectors was measured experimentally. A mask with an array of holes with different sizes and spacings was positioned in front of the detector. An alpha particle source was used as a source of uniform parallel-ray ions. The image of the masked detector was reconstructed using the computer. The resolution was found to be about 0.5 mm. This translates into momentum resolution of 0.06 a.u. We had to take into consideration that this position resolution affects

the electron momentum distributions directly through the electron detector and indirectly through the uncertainty carried with the recoil ions position.

Adding the different contributions to the resolution, in quadrature, for protons data yields

$$\Delta P_Z = [(0.08P_Z)^2 + (0.08)^2 + 2(0.06)^2]^{1/2} \quad , \tag{3.5}$$

$$\Delta P_Y = [(0.08P_Y)^2 + (0.08)^2 + 2(0.06)^2]^{1/2} \quad , \tag{3.6}$$

and for the C^{6+} data,

$$\Delta P_Z = [(0.04P_Z)^2 + (0.08)^2 + 2(0.06)^2]^{1/2} \quad , \tag{3.7}$$

$$\Delta P_Y = [(0.04P_Y)^2 + (0.08)^2 + 2(0.06)^2]^{1/2} \quad . \tag{3.8}$$

For a typical Z-momentum component equal to 1 a.u. we find that $\Delta P_Z = 0.14$ a.u. for protons and $\Delta P_Z = 0.11$ a.u. This error can be safely neglected for distributions wider than 1 a.u.

3.2 Velocity Dependence of the EEMDs

We will present the results of this experiment in the form of two-dimensional electron-momentum distributions in the YZ plane. As we mentioned earlier, the X-component of the electron momentum remains undetermined. This will have a small effect on the value of the spectra because of the cylindrical symmetry of the electron momentum distribution in the XY plane. Some of the data presented in this chapter can be found in the publications [61-63].

3.2.1 p + He, Ne

The system of protons colliding with He was the first system to be studied for several reasons. First, it is the simplest ion-atom system, except for protons on atomic hydrogen which requires special consideration in producing target atomic hydrogen. Second, this system received a considerable amount of attention experimentally and theoretically for several years. Finally, this system is easier to be dealt with theoretically than more complex systems. For the sake of comparison, we also studied the collision of protons on a Ne target. The target type in these collisions proved to have little effect on the EEMDs.

The system of p + He was studied using this technique in the velocity range of 0.63 - 2.39 a.u. The highest velocity studied corresponded to an energy of 140 keV, close to the highest energy achievable with KSU CRYEBIS. Fig. 3.6 shows the 2-d EEMDs for this system. The target velocity, which is zero in the lab frame, is marked by a vertical dashed line. The projectile velocity is marked by short vertical solid lines. The differences in magnitude between contour lines of individual plots are constant in spacing, but differ between plots due to the varying number of total counts in each spectrum. We can see the visual advantage of this technique of electron spectroscopy. In one glance we can get a comprehensive idea about the electron-momentum distribution in both directions, parallel and perpendicular to the direction of the projectile ion beam. A general characteristic of all spectra is that most of the electrons are ejected in the forward direction (the positive Z direction). We will see later that this behavior is not limited to this system, but rather is a general behavior for ionization in ion-atom collisions in this range of velocity. This general behavior is due to the strong two-center effect in this range of velocity.

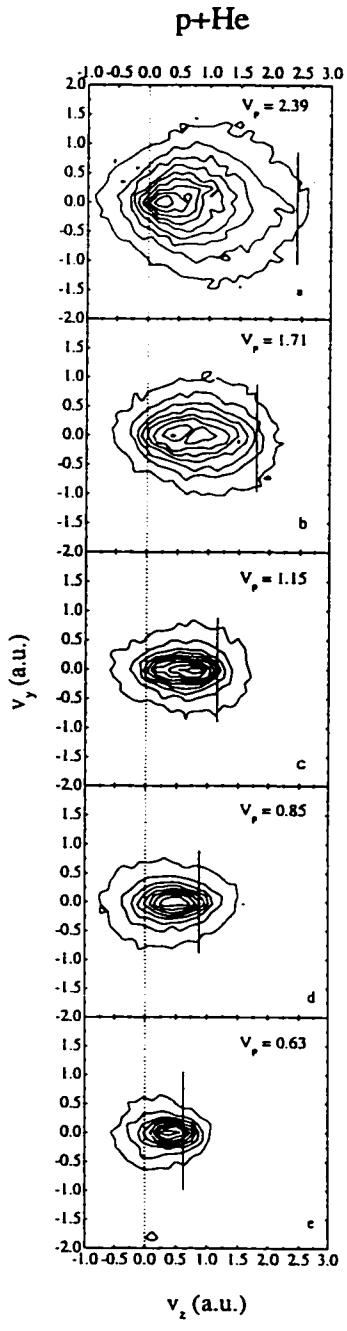

Figure 3.6: Contour plots of the two-dimensional electron momentum distributions from p + He collisions for the ionization channel. The solid lines are located at the projectile velocities.

At high projectile velocities, the electron-momentum distribution is peaked near the target velocity. By decreasing the velocity, the peak of the distribution shifts toward the projectile velocity. At the lowest velocities the peak is about midway between the projectile and the target (in velocity space). This indicates the possibility of a saddle point ionization mechanism at lower velocities ($v_p < 1$ a.u.).

To have a more quantitative idea about the electron momentum distribution, one-dimensional momentum distributions were produced from the two-dimensional momentum distributions. Every spectrum in Fig. 3.6 was integrated first, over all values of v_y to make the 1-d EEMD in the Z direction parallel to the projectile ion beam and second, it was integrated over all values of v_z to produce the 1-d EEMD in the y direction perpendicular to the direction of the beam. The results of this integration are presented in Fig. 3.7. Experimental data are compared with the CDW-EIS and CTMC theoretical calculations. Experimental data were integrated and then normalized to the total ionization cross section [134]. The peak heights of the theoretical results were scaled to coincide with the experimental peak heights so that the momentum-distribution shapes could be easily compared. Table 3.1 contains the values the theoretical results were multiplied by. In general, the experimental and theoretical results were in good agreement, except for $v_p = 1.15$ a.u., where the CDW-EIS result was more strongly peaked near the projectile velocity (Z distribution) than in the experiment. Results for the CDW-EIS are not shown below $v_p = 1.15$ a.u. since it was expected that the theory would fail at those low velocities.

The progression of the spectra of Fig. 3.6 and Fig. 3.7 as the projectile velocity is lowered can be discussed as a continual progression from high- to low-velocity impact ionization mechanisms. Beginning at the highest velocity of 2.39 a.u., for

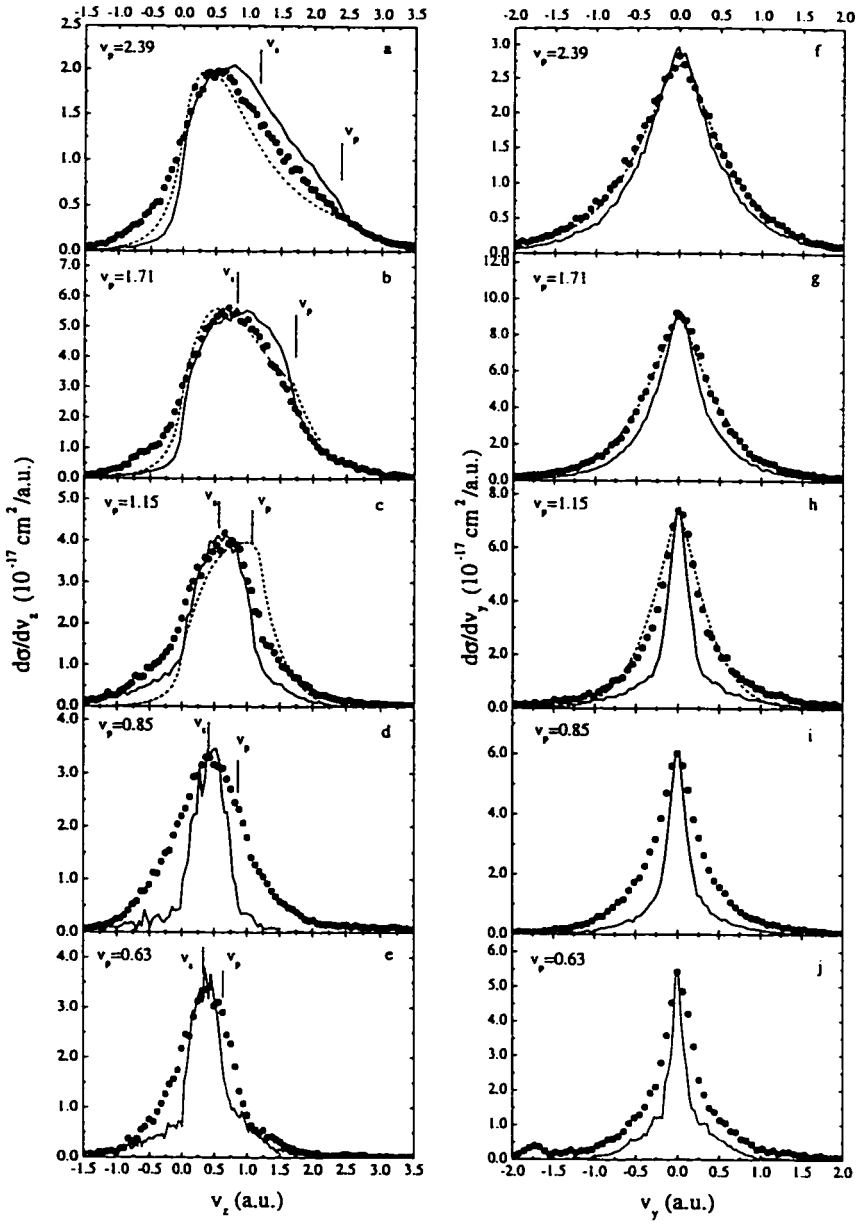

Figure 3.7: Z- and Y-electron momentum distributions from the ionization channel for p + He collisions for v_p = 2.39, 1.71, 1.15, 0.85, and 0.63 a.u. The filled circles are the experimental data, the dashed lines are the CDW-EIS results, and the solid lines are the CTMC results. The short lines annotated by v_s and v_p indicate the position of the saddle-point electron velocity calculated from Eq. (3.1) and electrons with the projectile velocity, respectively.

collision velocity (a.u.)	CDW-EIS Z	CDW-EIS Y	CTMC Z	CTMC Y
		C^{6+} + He		
1.63	0.44	0.97	1.52	0.90
1.38	0.45	1.14	0.60	0.60
1.16	0.84	2.35	*	*
		p+He		
2.39	0.77	0.91	1.12	0.94
1.71	0.94	1	1.61	1.25
1.15	1	1.14	2.27	1.65
0.85	-	-	1.59	2.30
0.63	-	-	*	*

Table 3.1: Values by which the CDW-EIS and CTMC present theoretical results were multiplied in the Z and Y directions so that the peaks of the distributions coincide with those of the present experimental results. CDW-EIS calculations were not performed for proton data below 1.15 a.u. (see text), indicated by -. Absolute total cross sections for the CTMC results at the lowest velocities for both the protons and C^{6+} data were not determined and are indicated by * in the table.

which DI (soft electrons) and ECC (cusp electrons) are still appropriate terms, one can identify the major ionization mechanism as being DI to the target continuum. A small hump in the EEMD exists at $v_p = 0$ that represents capture into the projectile continuum. This hump is much more noticeable when electrons with only small Y momentum are examined as shown in Fig. 3.8. Such a spectrum that integrates over all X momenta still emphasizes forward electrons. The hump seen in that spectrum is that seen in the energy-loss spectra of Vajnai *et al.* [134] and corresponds to the cusp peak routinely observed in 0° spectra at high velocities. It is clear that even at this velocity, this feature represents only a small contribution to the total cross section and would likely be overlooked without emphasis on forward directed electrons. As v_p is reduced, DI electrons can more strongly interact with the Coulomb potential of the outgoing proton; thus the DI electrons can be described as "focused" and pulled toward the projectile [136]. This shifts the DI electron peak closer to v_p in the longitudinal (Z) direction and narrows the distribution in the Y direction. As v_p is reduced, the ECC contribution appears to grow in relative importance, but the overlap of these ECC electrons with the DI peak becomes so strong that it is no longer possible to describe these as different features in the spectrum. The two features in the spectra coalesce into a single peak that seems to settle at approximately the velocity of the saddle of two singly charged ionic cores. Whether this result by itself constitutes evidence for the dominance of the T process is not immediately claimed, but the data certainly seem qualitatively consistent with the physical picture of saddle-point electrons. The evolution of the longitudinal momentum spectrum from the target centered toward the saddle is emphasized in Fig. 3.9, where the data are plotted versus v_z/v_p, thereby removing the infiuence of the overall scale factor v_p from the appearance. This evolution of the

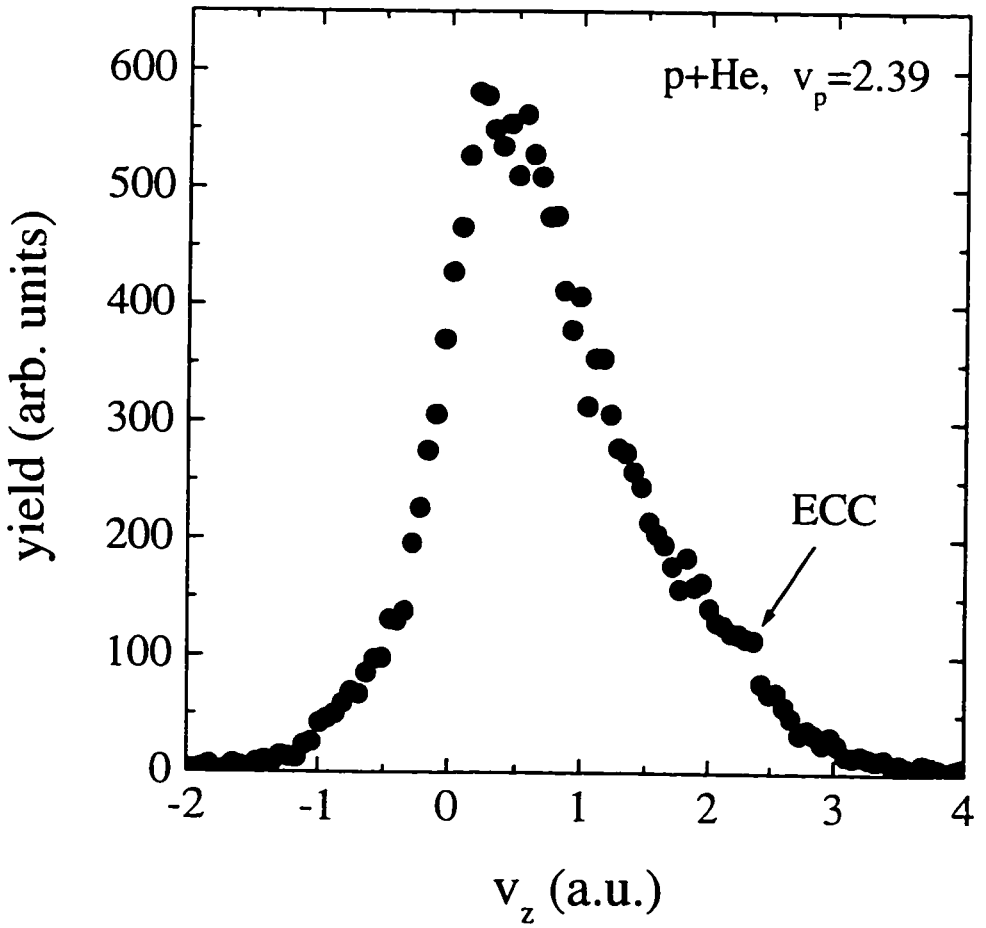

Figure 3.8: The same experimental data as displayed in Fig. 3.7(a) but the projection onto the Z axis is only for small Y momentum ($v_y \approx \pm 0.18$ a.u.). The hump in the distribution caused by ECC electrons is clearly observed.

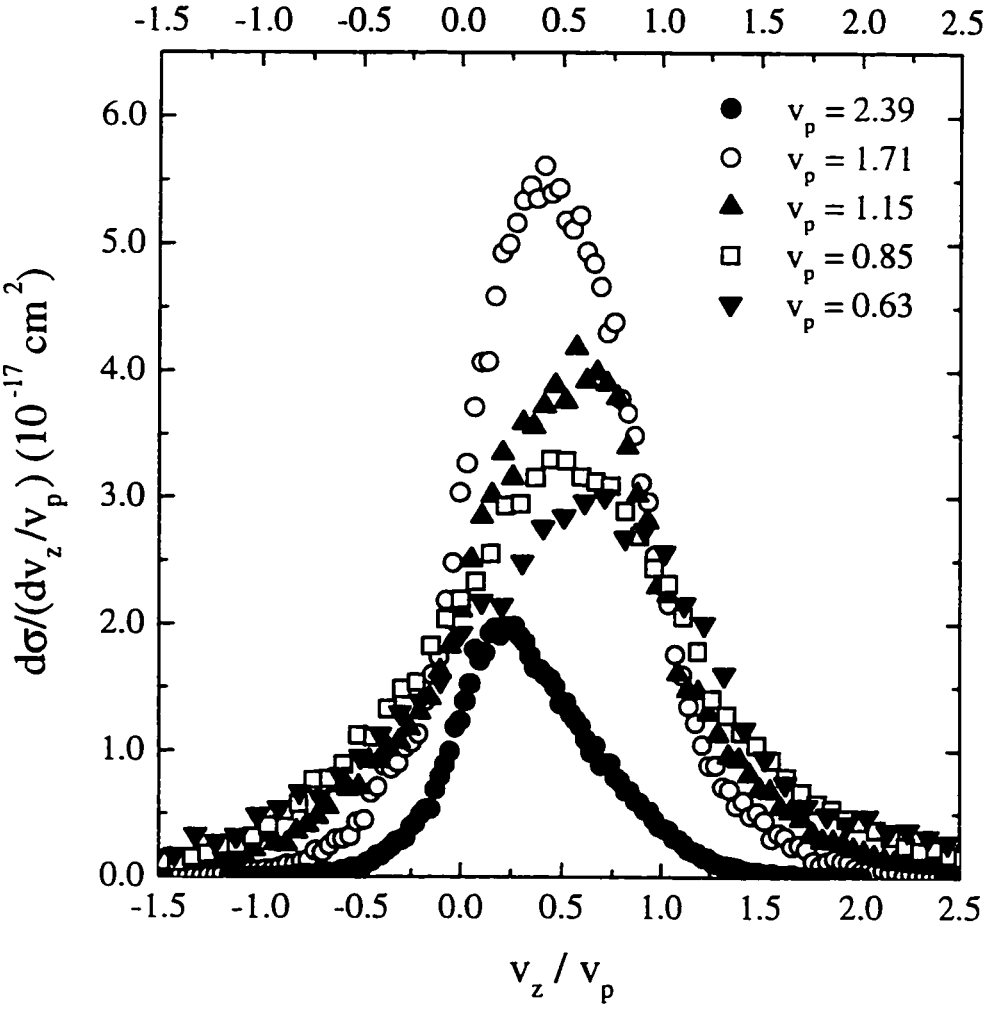

Figure 3.9: Plot of the experimental Z-electron momentum distributions vs the Z-electron velocity over the projectile velocity for p + He collisions resulting in pure ionization.

spectrum is qualitatively described by both the CDW-EIS and CTMC calculations, although the former seems to overestimate the importance of the projectile-electron interaction at $v_p = 1.15$ a.u.

The relative narrowing of the spectrum in the transverse (Y) direction is also rather well described by both calculations. We note that, because of the rather complicated dependence of the resolution function on the electron momenta, we have not tried to fold the theoretical spectra into the experimental resolution function. Such a folding would be expected to have only a small effect on most of the spectra, but for the very narrow transverse distributions at $v_p = 0.85$ a.u. and below such a folding would improve the agreement between the CTMC and experimental transverse spectra. The transverse spectra evolve from nearly equal longitudinal width at 2.39 a.u. to sharply centered on the beam axis at low velocities. Such a behavior could be ascribed within the saddle-point terminology as due to an adiabatic transverse cooling of the electrons as the transverse harmonic potential well seen by these electrons gradually dissolves as the ion cores recede from each other.

3.2.2 C^{6+} + He, Ne

The system of C^{6+} + He was studied at three velocities; 1.62, 1.38, and 1.16 a.u. We note that while the velocity range covered by the proton data goes from below to above the velocity-matching maximum in the total cross section, the C^{6+} data all lie at velocities far below the corresponding maximum, and thus should be viewed as representing only the low-velocity region. Fig. 3.10 shows the two-dimensional distributions of the ejected electron momentum. The distributions are strongly oriented in the forward direction with a pointed edge near the target. As was seen in the protons data, the distribution becomes smaller and narrower by decreasing

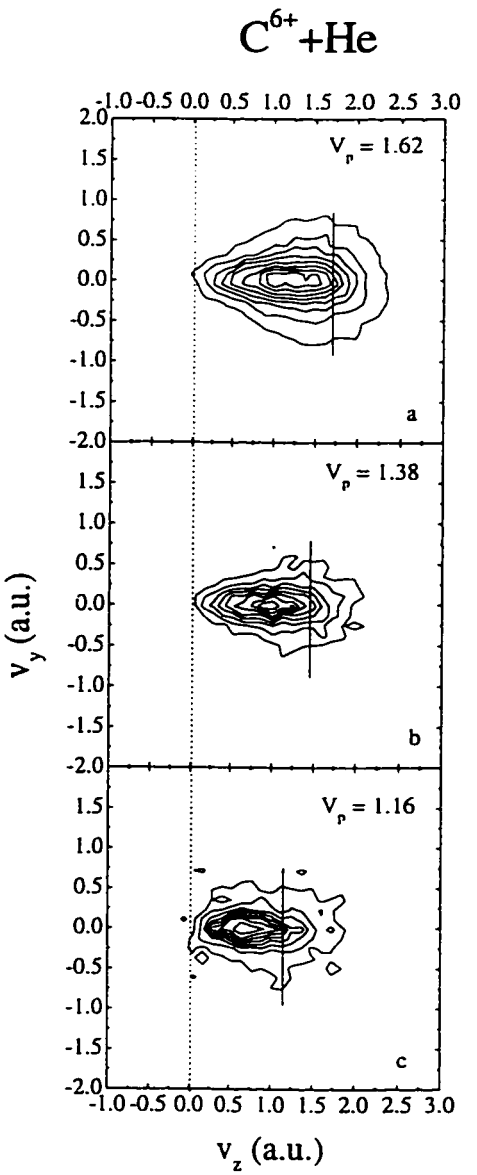

Figure 3.10: Contour plots of the two-dimensional electron momentum distribution from C^{6+} + He collisions for the ionization channel. The solid lines are located at the projectile velocity.

the projectile velocity. Fig. 3.11 shows the Z and Y projections of the two dimensional distributions. The spectra show that the fraction of electrons ejected in the backward direction is very small. This fraction decreases by increasing the projectile velocity in the studied range. The Z distributions seem to have an onset at the target velocity in the forward direction. The spectra are resolutely centered at a velocity of about $3v_p/4$. This characteristic is more clearly shown in Fig. 3.12, which shows these spectra plotted versus v_z/v_p. By decreasing v_p, the peak appears to shift slightly toward lower velocities and hence have a better agreement with the saddle-point ionization mechanism. But still the peak is well above the saddle-point velocity which is about $0.29v_p$ for this system. A strong disagreement between experimental data and theoretical calculations and among theoretical calculations can be seen. This disagreement is worse than what was seen in the protons data. The disagreement increases by lowering v_p. The CTMC calculations underestimates the electrons emitted with a velocity near the projectile velocity while the CDW-EIS calculations overestimate it. In the transverse direction, the distributions are narrow and become narrower by decreasing v_p. The calculations also do not have a good agreement with experimental results although the CTMC seems to have a better agreement at lower velocities.

3.3 Projectile Charge-State Dependence of the EEMDs

Ionization of He and Ne by a series of bare ions was studied at $v_p = 1.63$ a.u. The projectiles used were p, He^{2+}, C^{6+}, O^{8+}, and Ne^{10+}. Some of the spectra shown previously for p and C^{6+} bombardment are reproduced here for completeness.

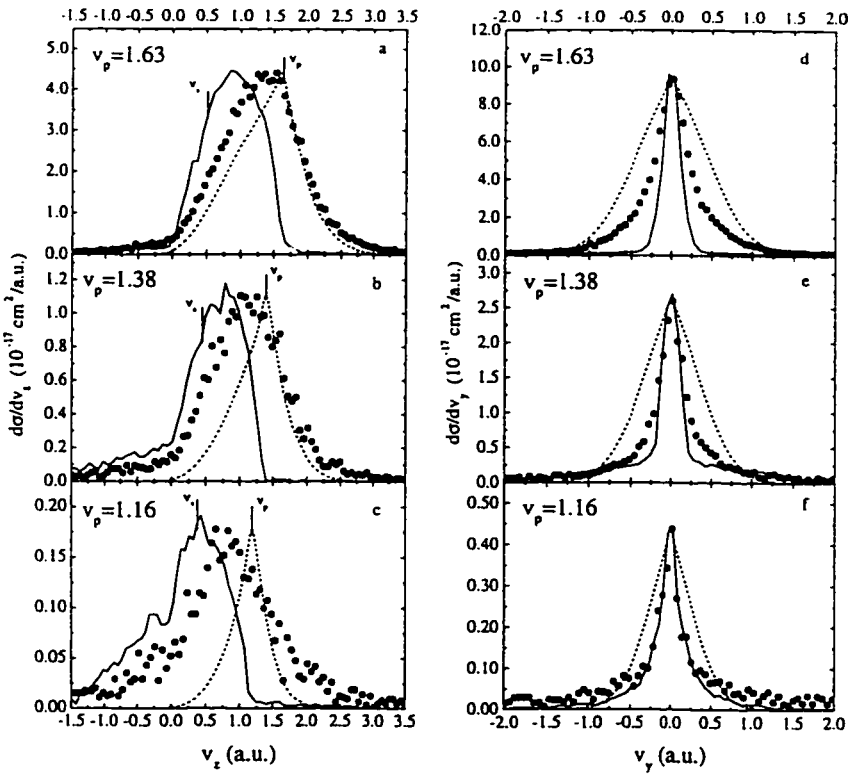

Figure 3.11: Z- and Y-electron momentum distributions from the ionization channel for C^{6+} + He collisions for v_p = 1.63, 1.38, and 1.16 a.u. The filled circles are the experimental data, the dashed lines are the CDW-EIS results, and the solid lines are the CTMC results. The short lines annotated by v_s and v_p indicate the position of the saddle-point electron velocity calculated from Eq. (3.1) and electrons with the projectile velocity, respectively.

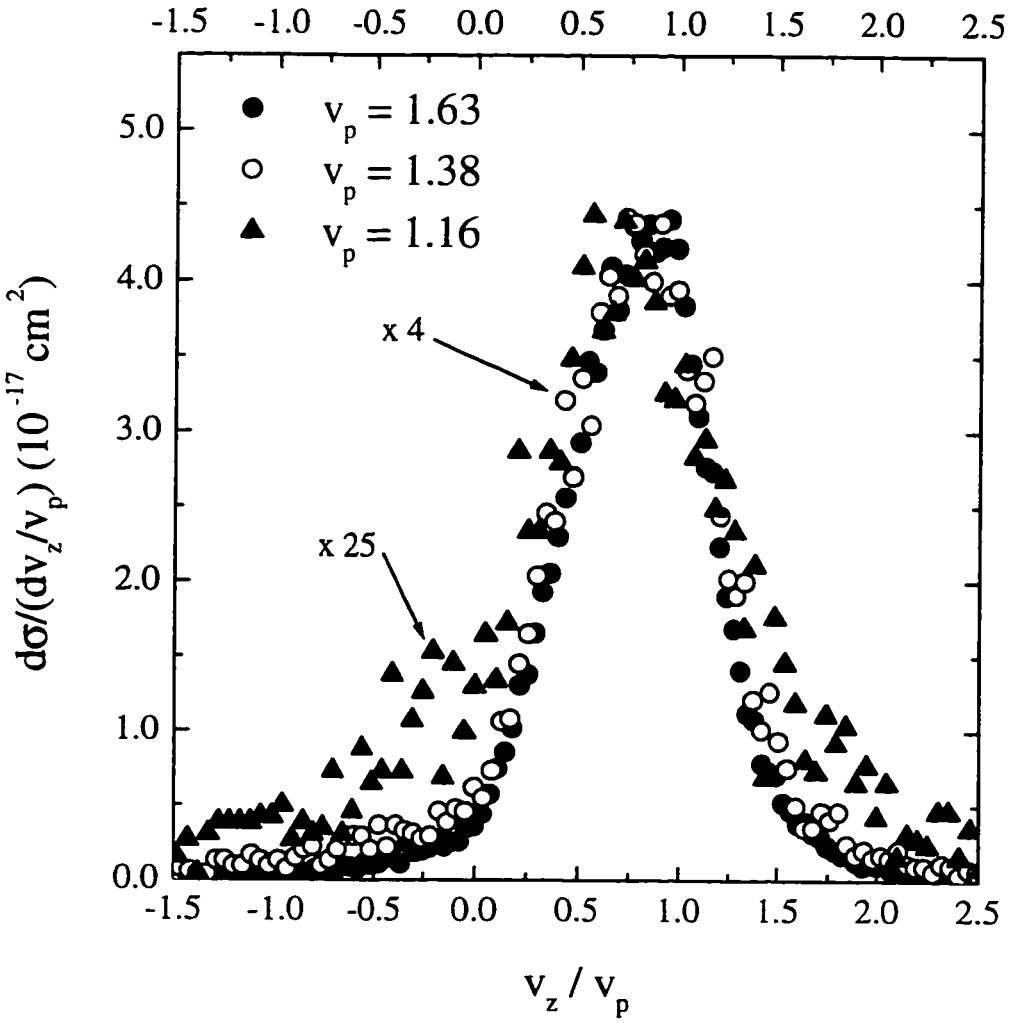

Figure 3.12: Plot of the experimental Z-electron momentum distributions vs the Z-electron velocity over the projectile velocity for C^{6+} +He collisions resulting in pure ionization.

The two-dimensional electron-momentum distributions are shown in Fig. 3.13. The peak of the distribution is located near the target ($v_z = 0$) for low charge states (p, He^{2+}). This peak shifts toward the projectile velocity for the highest three charge states. This behavior is opposite to what is expected if the distribution follows Eq. (3.1). This indicates that a naive picture of saddle-point mechanism that produces electrons with forward velocities that agree with Eq. (3.1) is not true in this range of velocity. This disagreement is emphasized in Fig. 3.14 and Fig. 3.15. By increasing the projectile-charge state, the saddle-point-electron velocity shifts toward the target velocity ($v_z = 0$ a.u.), while the peak of the distribution shifts toward the projectile velocity ($v_z = 1.63$ a.u.). Similar behavior is seen independent of the target type. The agreement between the position of the peak and v_s for the protons data for both targets occurs only at low velocity and for singly charged projectiles. Spectra seem to saturate at a nearly universal shape centered near the projectile velocity. As discussed before, these results verify the strong influence of the projectile charge on the emitted electrons distribution. Technically this is called Coulomb focusing and is expected to increase by increasing the projectile charge state. This focusing effect also can be seen in the transverse (Y) distributions. This distribution becomes narrower by increasing the projectile charge state. Coulomb focusing also explains the decrease of the fraction of electrons emitted backward by increasing projectile charge state. The emitted electrons are strongly "pulled" forward by the relatively slowly moving high-charge projectile. They are not given the chance to "fly backward" as seen in the high velocity electron spectra.

Fig. 3.16 shows the CDW-EIS calculations for the systems presented in Fig. 3.14. The calculations are able to reproduce the general behavior observed in the experimental data. However, they tend to overestimate the role of the process of electron

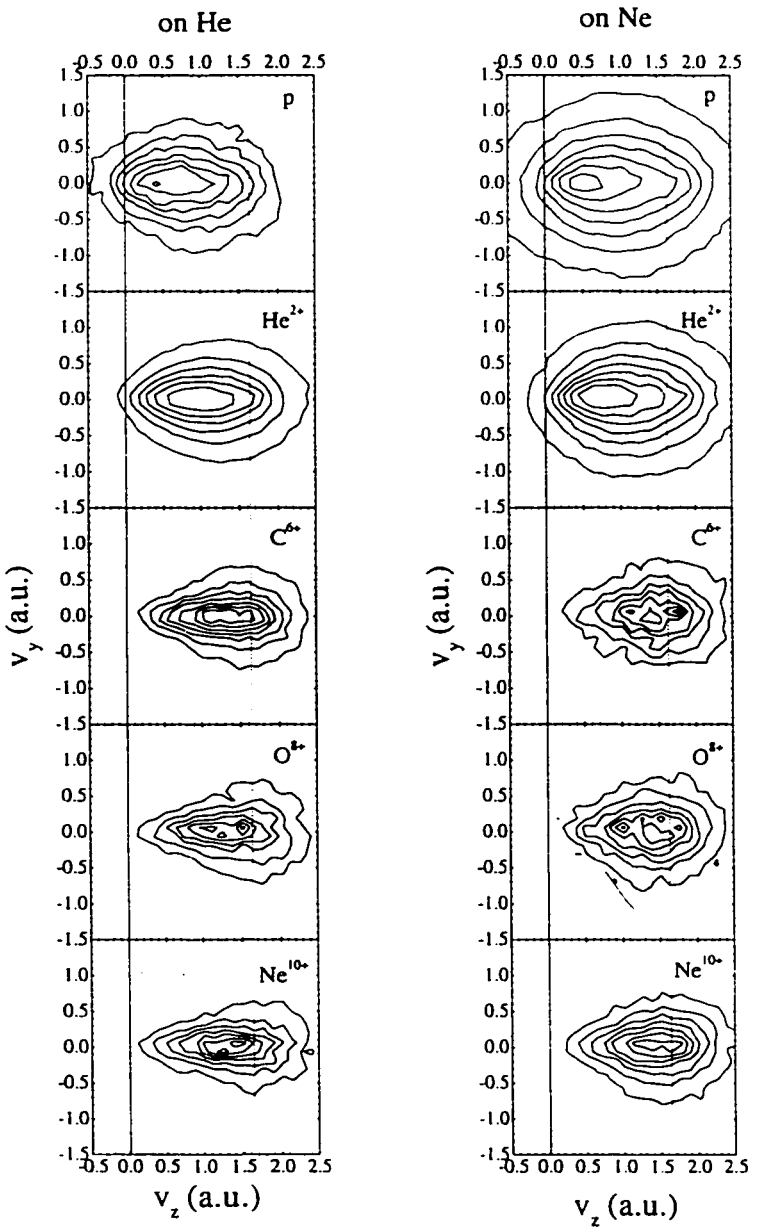

Figure 3.13: Contour plots of the two-dimensional electron-momentum distribution from p, He^{2+}, C^{6+}, O^{8+}, and Ne^{10+} + He, and Ne collisions for the ionization channel. The solid line guides the eye to the target velocity ($v_z = 0$). The dashed line guides the eye to the projectile velocity ($v_z = 1.63$ a.u.).

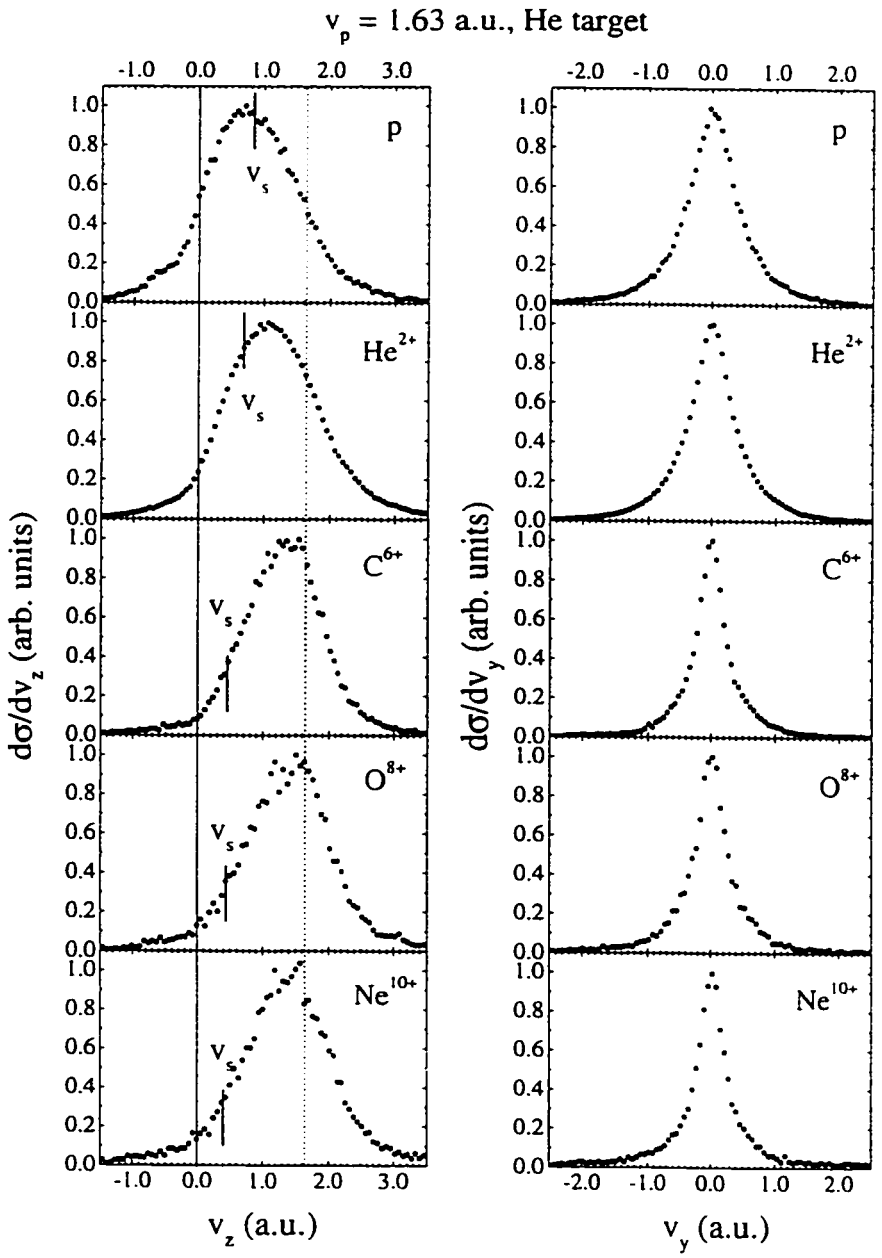

Figure 3.14: Z- and Y-electron momentum distributions from the ionization channel for p, He^{2+}, C^{6+}, O^{8+}, and Ne^{10+} + He collisions at $v_p = 1.63$ a.u. The short lines annotated by v_s indicate the position of the saddle-point-electron velocity calculated from Eq. (3.1). The projectile velocity is indicated by a vertical dashed line.

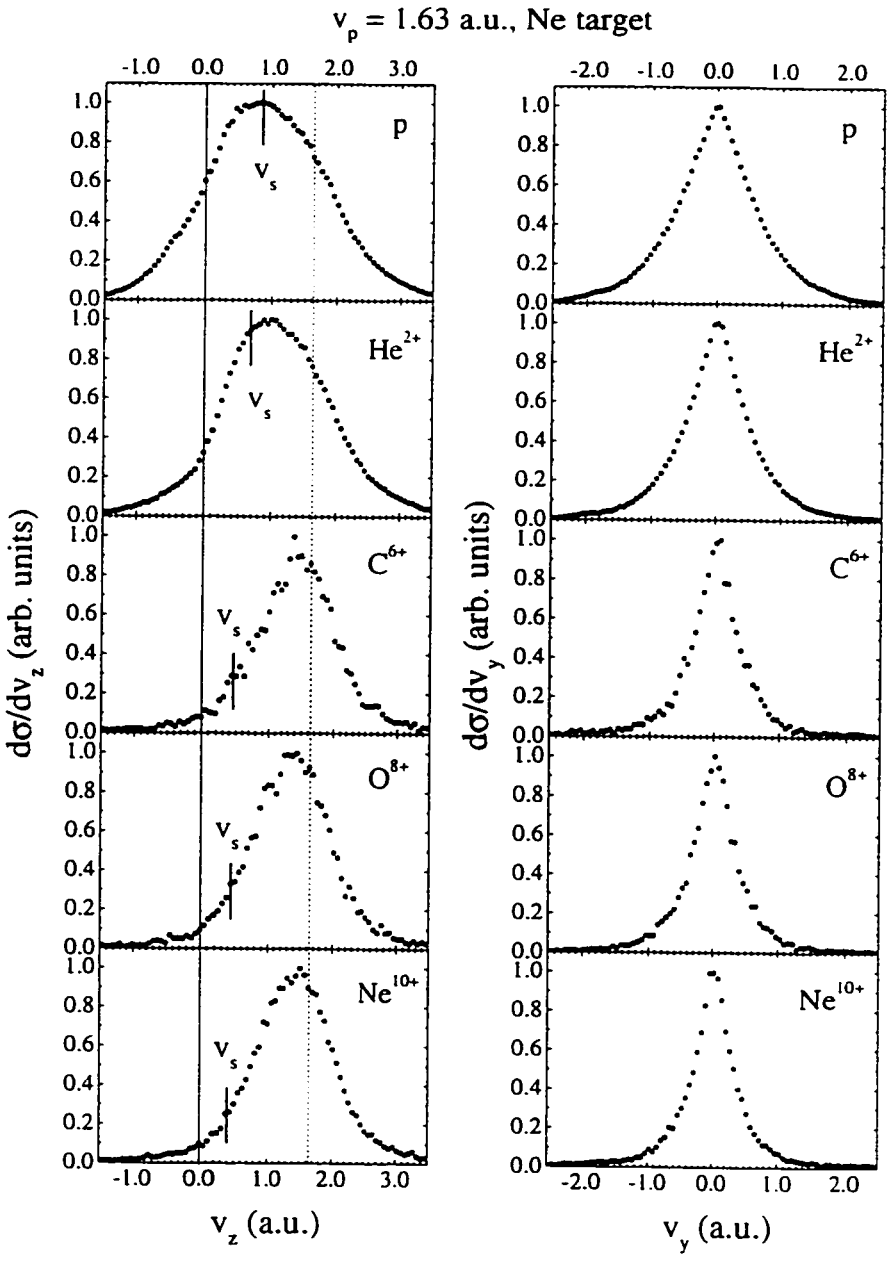

Figure 3.15: Z- and Y-electron momentum distributions from the ionization channel for p, He^{2+}, C^{6+}, O^{8+}, and Ne^{10+} + Ne collisions at v_p = 1.63 a.u. The short lines annotated by v_s indicate the position of the saddle-point-electron velocity calculated from Eq. (3.1). The projectile velocity is indicated by a vertical dashed line.

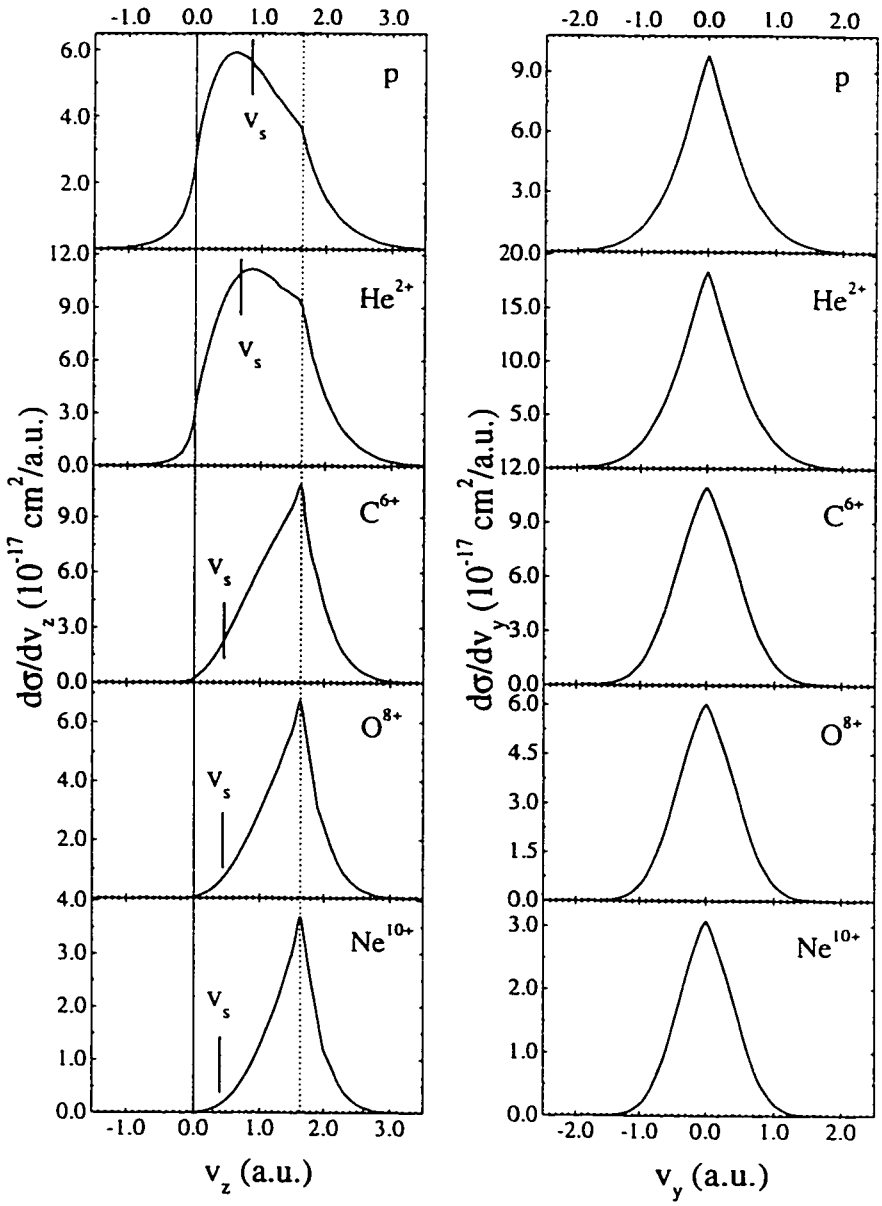

Figure 3.16: Theoretical CDW-EIS calculations for the systems shown in Fig. 3.14. The solid line guides the eye to the target velocity while the solid line guides the eye for the projectile velocity. The short solid lines indicate the saddle-point velocity.

capture to the continuum. This process is marked by a hump at $v_z = v_p$ for p + He and He^{2+} + He and a dominant cusp-like peak for the highest three projectile charges (C^{6+}, O^{8+}, and Ne^{10+}). This disagreement is expected since we apply this theory at the lower edge of its validity region.

The role of ECC can be emphasized in our data by selecting electrons emitted with a small v_y. We have to note that we cannot reproduce 0° electron spectroscopy spectra from our data since the third component of the electron momentum (v_x) was not measured. In Fig. 3.17 we present the longitudinal distributions for three systems with $| v_y |< 0.2$ a.u. so the ECC hump can be identified. Comparing the spectra for p + Ne at $v_p = 2.39$ a.u. and at 1.63 a.u. shows that the ECC process contribution to the total cross section becomes more important at lower projectile velocities. This is expected since single electron capture in this range of velocity increases by decreasing v_p. In addition, it is straightforward to see the shift of the DI process peak away from the target by decreasing v_p due to the increasing effect of the projectile charge at lower velocities. At the same velocity, the DI peak for He^{2+} + He is about $v_z = 0.35v_p$ while for p + He is about $0.2v_p$. This again supports the important role of the projectile-charge state in shaping the electron-momentum distribution.

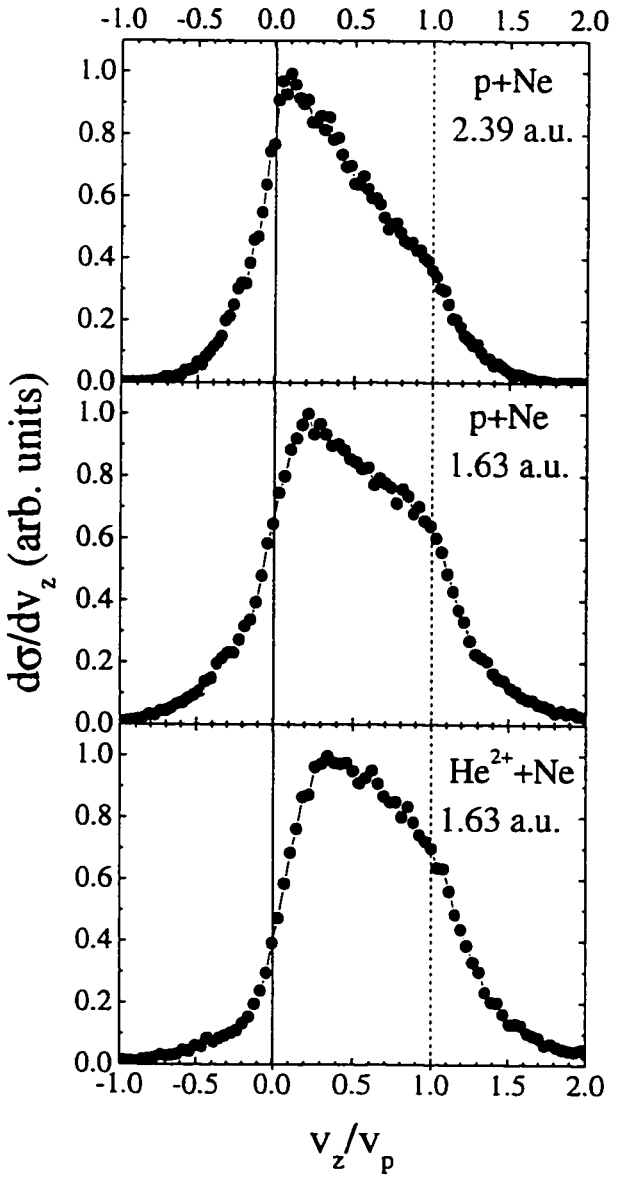

Figure 3.17: Slices of three selected two-dimensional momentum distributions projected into the longitudinal direction with $\mid v_y \mid < 0.2$ a.u. The humps at $v_z = v_p$ are due to electron capture to the continuum.

Chapter 4

Electron-Momentum Imaging: Fully Determined Recoil-Ion momentum

In the series of experiments that we discussed in the previous chapter, the coincidence detection of the recoil ions served the experiments by providing two things: (a) separating the target atoms that lost only one electron (He^+ and Ne^+) through their time-of-flight and (b) providing a spatial marker that indicates the place at which the collision happened and therefore electrons were born. This was necessary because the target gas was in the form of diffusive gas filling the whole space of the spectrometer. To develop the technique further so we can utilize the information carried by the recoil ions, we developed a new experimental setup in which target atoms are in the form of a supersonic gas jet. Measuring the position of the recoil ions and their time-of-flight allowed us to reconstruct, with a high accuracy, their full momentum vector at the time of their birth. Therefore, the scattering plane,

the impact parameter, and the Q-value of the collision, valuable information that could not be determined in our first-generation experiments, were determined.

4.1 Experimental Technique

4.1.1 Experimental Setup

The ion beam delivered by the ion source was collimated by an aperture in the entrance to the collision chamber to 1 mm in diameter. The target He was in the form of a supersonic gas jet. A general description of this type of atomic beam is given in appendix C. A detailed discussion of the jet employed in our experiment is given in appendix D.1. The width of the jet in the collision area was about 3.5 mm. Fig. 4.1 shows a schematic sketch of the experimental setup. The target gas was first cooled through thermal contact with a cold head of a cryopump. The temperature of the cold head was about 60 °K. The cooled gas escaped through a hole of 30 μm in diameter. This produced a supersonic flow of the gas where most of thermal velocity was converted into a directional velocity in the direction of flow of the gas. This cooling by supersonic expansion resulted in target atoms very well localized in space and in velocity. The gas jet was skimmed by a conical skimmer with an aperture of diameter of 0.5 mm thus keeping the cooler inner part of the jet. To minimize the hot gas in the collision area the gas jet was dumped to a differentially pumped region, called the catcher. The base pressure in the collision area, while the gas jet was off, was about 1×10^{-8} torr rising to 1×10^{-7} torr when the jet was turned on. Details of the differential pumping of the system are provided in appendix D.2. The spectrometer , Fig. 4.2, consisted of 96 electrodes with 1 mm separating every electrode and its neighbor. A resistor chain was used to supply every electrode with

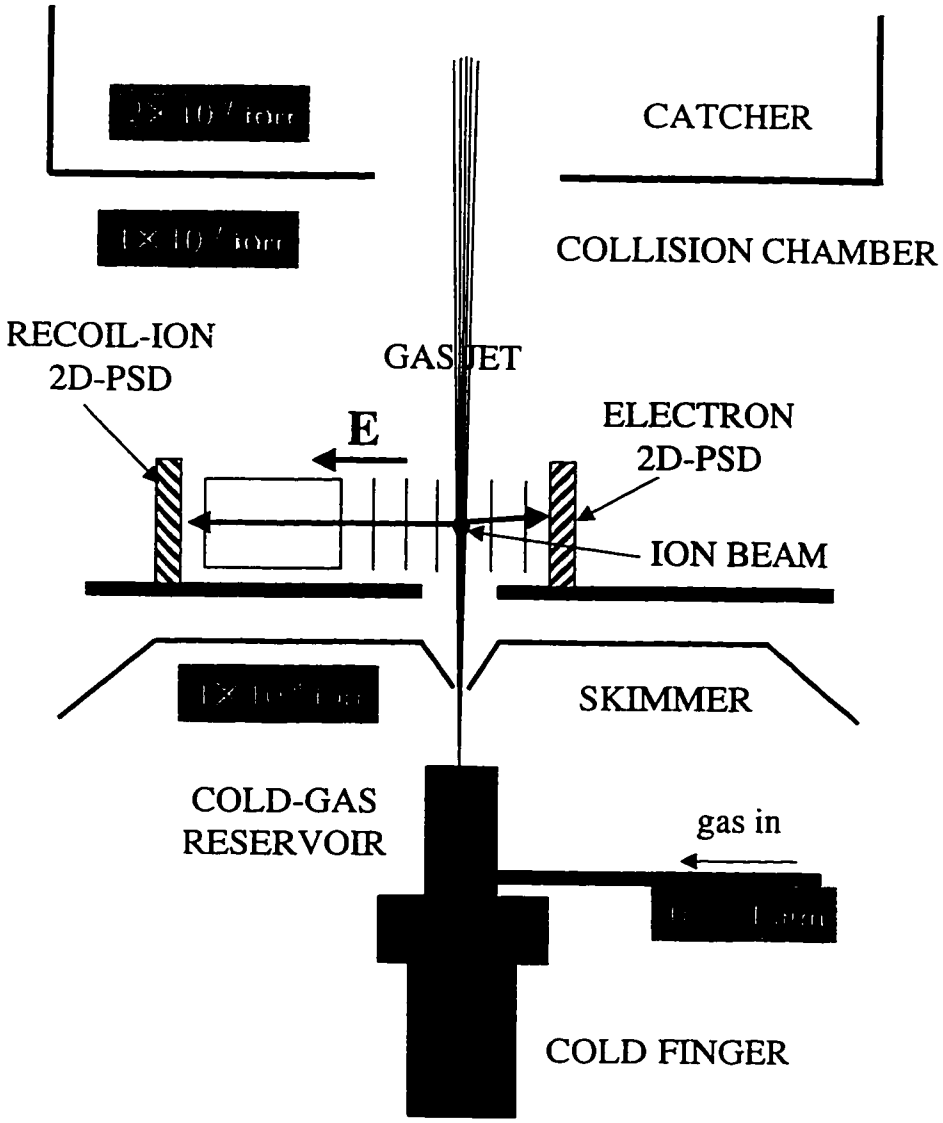

Figure 4.1: Schematic sketch of the experimental setup in the second-generation experiments using a supersonic gas jet.

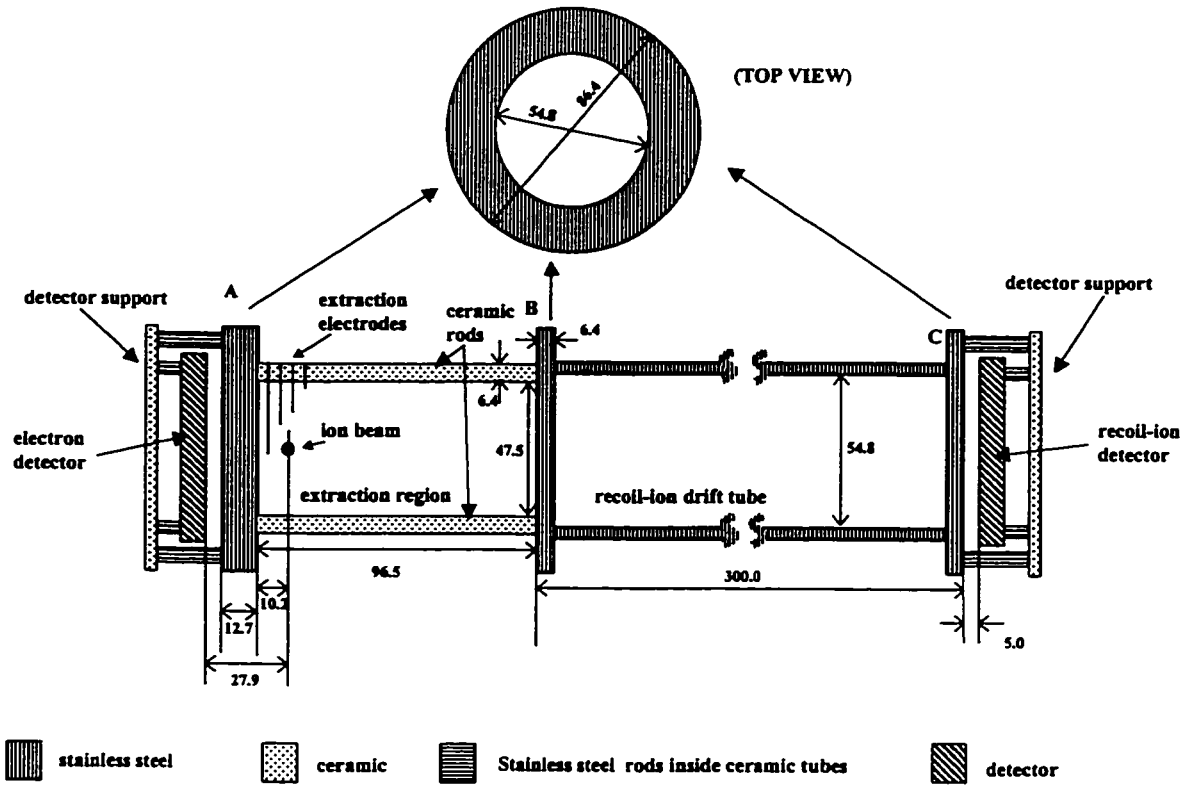

Figure 4.2: Time-of-flight-position spectrometer used in extracting and detecting electrons and recoil ions. The dimensions are in millimeters. Extraction electrodes displayed are not to scale and few are shown for illustration. Each detector is made of a stack of three micro-channel plates and a wedge-strip-type anode.

the required potential. This produced an electric field perpendicular to both the direction of flow of the gas jet and the direction of the projectile ion beam. Under this field, electrons produced during the collision were accelerated over a distance of 10.2 mm. Then they traveled a distance of 12.7 mm in a field free region. A small negative bias voltage was put on the top of the first channel plate to push away stray electrons which were mostly very slow electrons. Electrons then were detected by a two-dimensional position-sensitive detector (2d-psd). Recoil ions were accelerated in the opposite direction a distance of 86.3 mm. Then they traveled in a field free region a distance of 305.0 mm to be detected by a 2d-psd identical to the one used to detect the electrons on the other end of the spectrometer. A field gradient in the recoil-ion side of the spectrometer was used to position-focus the recoil ions.

A schematic sketch showing the voltage distribution on different parts of the spectrometer is shown in Fig. 4.3. The two ends of the resistors chain are connected to the two power supplies denoted by A and C. A third power supply (B) is connected between the resistors 42 and 43 (counting from left to right). This assembly was used to generate a field gradient in the recoil-ion side of the spectrometer. This field gradient served the experiment by position-focusing the recoil ions on the recoil-ion detector. This position focusing was necessary in order to minimize the effect of the finite width of the ion beam (1 mm) and the width of the gas jet at the collision area (3.5 mm) on the resolution in the recoil-ion momentum. This field gradient had no effect on the electrons since they were generated and accelerated in a uniform-field region. The two grids of the recoil-ion detector were connected to the power supplies RG1 and RG2. The top of the three channel plates was connected to a power supply RTCP and the back to a power supply RBCP. The anode was connected to a power supply RGe. Similar arrangement was made for the electron detector except that

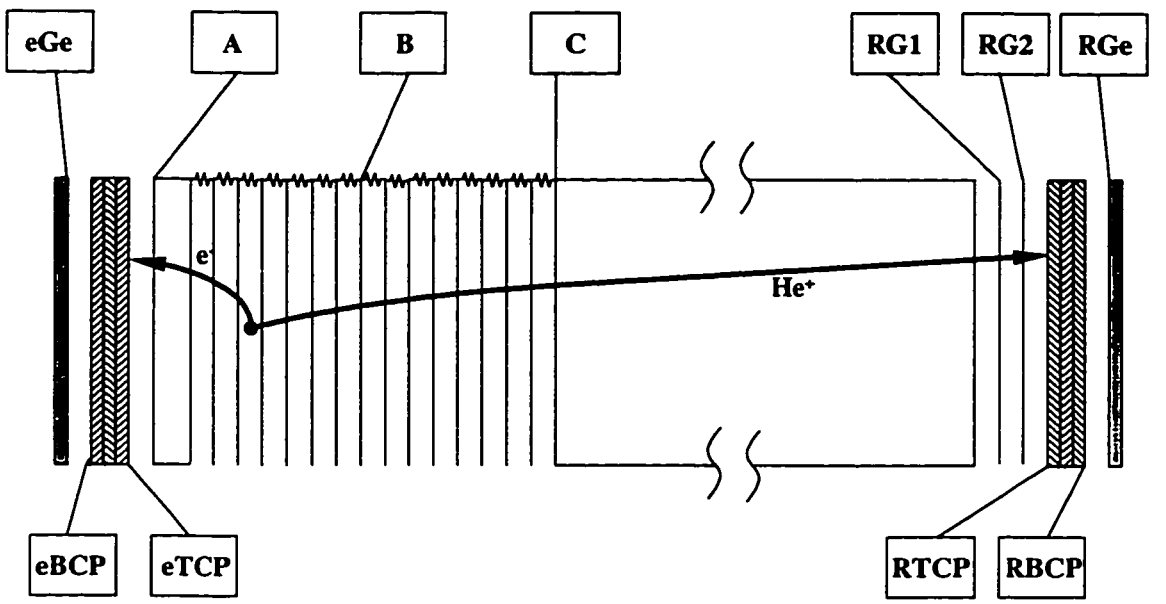

Figure 4.3: Schematic sketch of the voltage distribution on different parts of the second-generation spectrometer. Different power supplies are presented by rectangles.

the two grids were physically connected to the electrode A which resulted in a field-free region between the two grids. The applied voltages varied from one experiment to another depending on the studied system. A typical distribution of voltages is for example: 0 kV on A, -0.168 kV on B, -0.6 kV on C and RG1, -2.0 kV on RG2 and RTCP, +0.30 kV on RBCP, +0.40 kV on RGe, -0.015 kV on eTCP, +2.3 kV on eBCP, and +2.4 on eGe.

Fig. 4.4 shows a conventional coordinate system that will be used in describing the results of this experiment. The projectile-ion beam is in the positive z direction. The gas jet flows in the positive y direction. The extraction electric field points in the negative x direction. Thus electrons are accelerated in the positive x direction while recoil ions are accelerated in the negative x direction. Two components of the recoil-ion momentum (p_z and p_y) are reconstructed from the position on the recoil-ion detector (z and y). In the same way the two components of the electron velocity (v_z and v_y) are reconstructed from the position of the electron on the electron detector. Typically, the time of flight of the electrons was about 7 nsec. On the other hand, the time of flight of the recoil ions was in the order of few μseconds. The spread in the time of flight of the electrons was about 1 nsec. This made measuring the third component of the electron velocity (v_x) unachievable. However, the time signal of the electrons was used to give the start signal for the time-to-amplitude converter (TAC) which was stopped by the recoil-ion signal, thus resulting in measuring the time-of-flight of the recoil ions and hence their initial momentum in the x direction. Therefore, the complete momentum vector of the recoil ions was determined.

The resolution in the electron spectra was dominated by the width of the ion beam (1 mm) in the y direction and the width of the gas jet (3.5 mm) in the z direction. The position resolution of the electron detector itself was determined to

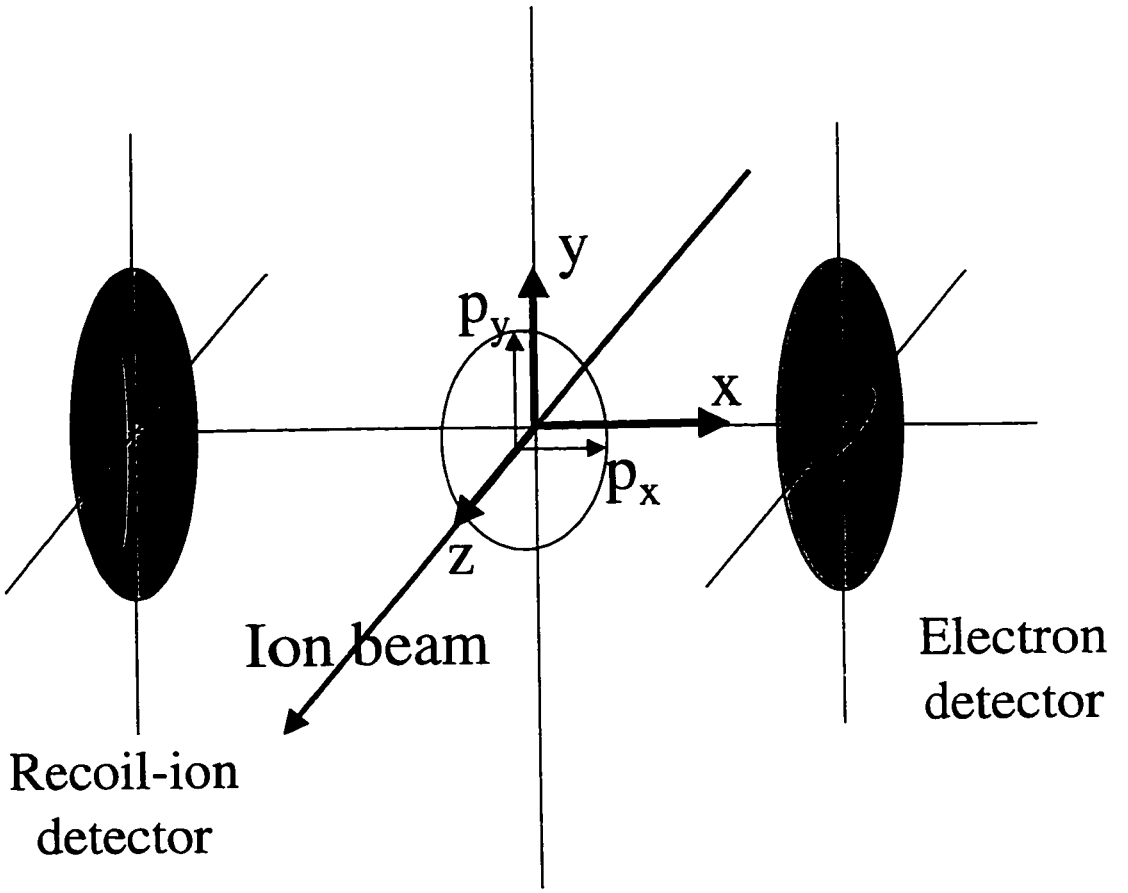

Figure 4.4: The coordinate system used in describing the results of this experiment.

be 0.35 mm, a negligible contribution. The extraction field ranged between 600 V and 2000 V over the total length of the extraction region (96 mm). In the y direction, resolution due to finite beam size ranged between 0.043 and 0.079 a.u. The biggest error was in the z direction caused by the thickness of the gas jet at the collision area. This error ranged between 0.15 and 0.27 a.u. depending on the strength of the applied electric field. another source of error resulted from the nonzero component of the electron momentum in the x-direction (toward or away from the electron detector). This unmeasured component of electron momentum resulted in slightly different times-of-flight for electrons with the same z- or the same y-components of momentum. Therefore electrons with the same p_z and p_y, for example, would hit the electron detector at slightly different locations depending on their initial p_x-component of momentum. This type of error was explained in detail in the previous chapter (section 3.1.3). Since the majority of the electrons are emitted with a transverse momentum of less than 0.2 a.u., the contribution of this sort of error to the total resolution can be neglected.

The recoil-ion detector had a position resolution similar to that of the electron detector. This resulted in an error that ranged between 0.36 and 0.67 a.u. of recoil-ion momentum depending on the strength of the applied electric field. Additional error is due to thermal motion of the recoil ions and the finite width of the gas jet and the ion beam. However, these errors are much smaller than the error due to the position resolution of the detector because of the position focusing of the recoil ions.

4.1.2 Data Reduction

The measured longitudinal momentum of recoil ions was used to calculate the energy loss of the projectile (the Q-value). Since the energy and momentum should be conserved in the collision, it is straightforward to prove that the Q-value of the ionizing collision is given by

$$Q \simeq -v_p(p_{r\|} + p_{e\|}) \quad , \tag{4.1}$$

where v_p is the projectile velocity and $p_{r\|}$ and $p_{e\|}$ are the longitudinal components of recoil-ion momentum and the electron momentum, respectively. In the present geometry, $p_{r\|} = p_z$ and $p_{e\|} = v_z$.

The transverse components of the recoil-ion momentum (p_x and p_y) were used to calculate the radial transverse momentum $p_{r\perp}$ for every collision event

$$p_{r\perp} = \sqrt{p_x^2 + p_y^2} \quad . \tag{4.2}$$

The transverse momentum of the recoil ions to very good precision balances the transverse momentum of the projectile ions after the collision. This is true since the transverse momentum of the ejected electrons in this range of velocity is much smaller than that of the recoil ions. Therefore, the laboratory scattering angle of the projectiles (θ_{lab}) can be calculated from the recoil ion transverse momentum ($p_{r\perp}$) by dividing by the initial momentum of the projectile ion (p_o).

$$\theta_{lab} = p_{r\perp}/p_o \quad . \tag{4.3}$$

Therefore, the impact parameter can be calculated from the transverse momentum if the scattering potential is known. However, we did not do that in this experiment,

but rather selected different ranges of impact parameter by selecting certain ranges of recoil-ion transverse momentum.

The direction of scattering of a certain recoil ion was used to determine a certain scattering plane. Here the scattering plane is defined as the plane that both the initial projectile momentum vector ($\mathbf{p}_o$) and the transverse momentum vector of the recoil ion ($\mathbf{p}_{r\perp}$) lie in. In particular, two cases were of interest: the case where the scattering plane is parallel to the electron detector and the case where the scattering plane is perpendicular to the electron detector. Selecting recoil ions scattered in the y direction defines a scattering plane that is parallel to the (y,z) plane and therefore parallel to the electron detector. On the other hand, selecting recoil ions that are scattered in the x direction defines a scattering plane that is parallel to the (x,z) plane and therefore perpendicular to the electron detector. Since electrons are detected in coincidence with recoil ions, this results in mapping electrons in the scattering plane in the first case and out of the scattering plane in the second case. Effectively this can be looked at as fixing a certain scattering plain, in this case in the yz plane, while electrons are detected as they will appear when viewing the scattering plane from the top (top view) or from the side (side view).

4.2 Results and Discussion

4.2.1 $He^+ + He$

Fig. 4.5 shows recoil-ion transverse momentum distribution for the collision of He^+ + He at a projectile velocity of 0.64 a.u. The two-dimensional distribution in the xy plane is shown in Fig. 4.5 (a). To calculate the radial transverse momentum, this distribution was integrated over all azimuthal angles. The result is presented

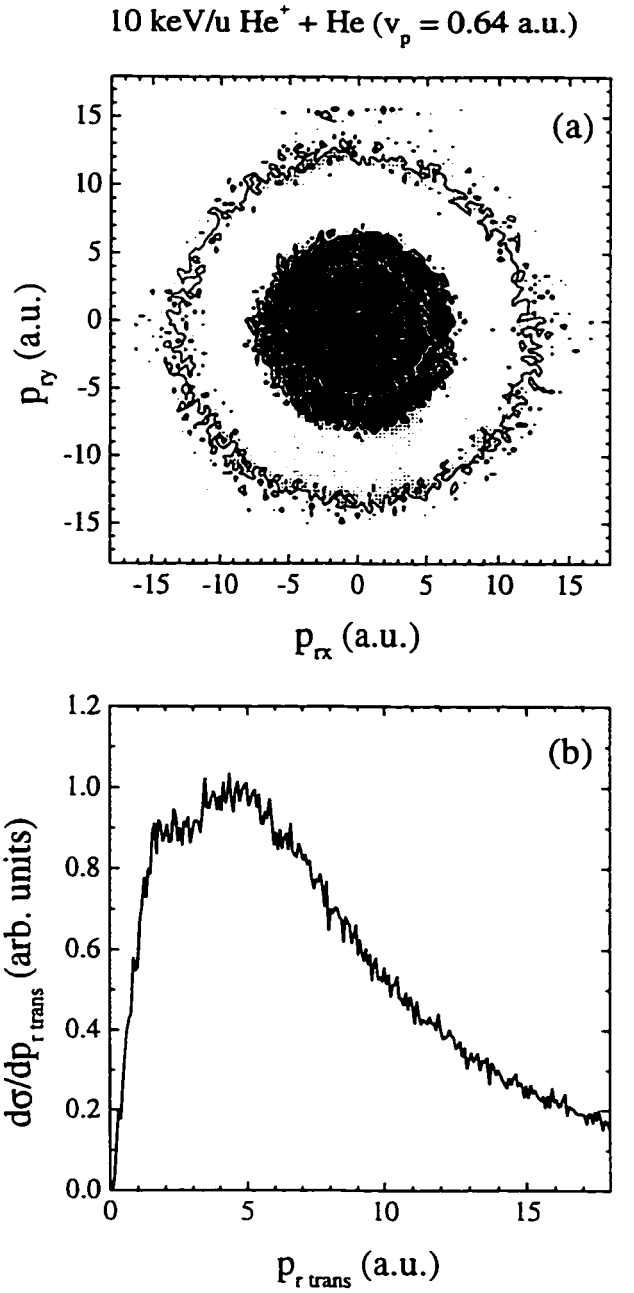

Figure 4.5: Recoil-ion transverse momentum distribution in the collision He^+ + He leading to single ionization. (a) is the distribution in the plane perpendicular to the ion beam. (b) is the radial distribution obtained by summing over all azimuthal angles according to eq. (4.2).

in Fig. 4.5(b). The slight asymmetry in the two-dimensional distribution is caused by the hot-gas component of the target He. The distribution shows a very sharp peak near $p_{r\perp} = 0$. This peak sits on top of much wider distribution. Although this peak is very pronounced, its contribution to the total cross section is small. This contribution can be seen in the form of a shoulder in the distribution shown in Fig. 4.5(b) located about $p_{r\perp} = 2$ a.u. This suggests that the ionization process in this system happens over a range of impact parameters where the contribution of small impact parameters is dominant. To have a more quantitative idea about this impact parameter range, we can apply the Rutherford scattering formula:

$$p_\perp = \frac{2q_t q_p}{bv_p} \quad , \tag{4.4}$$

where q_t and q_p are the effective charges for the target and the projectile, respectively, and b is the impact parameter. Assuming the distribution is peaked about $p_\perp = 4$ a.u., and that $q_t = q_p = 1$, we find that $b \sim 0.8$ a.u. This impact-parameter-distribution peak position is in general agreement with the impact parameter distribution calculated using the CTMC method for 15 keV p + He presented by Dörner *et al.* [49].

Fig. 4.6(a) shows recoil-ion transverse momentum plotted versus longitudinal momentum. In the longitudinal direction, most of the distribution is centered about 1.25 a.u. This corresponds to single electron ejection from the He atom. This can be verified by calculating the Q-value distribution. The calculated Q-value distribution is presented in Fig. 4.7. The main peak is located at about -30 eV which is 5.4 eV below -IP_1(He) where IP_1(He) is the first ionization potential of He. This difference accounts for the average energy of the ejected electrons. Another peak can be seen in Fig. 4.6 and Fig. 4.7. This peak is at about 4 a.u. in longitudinal

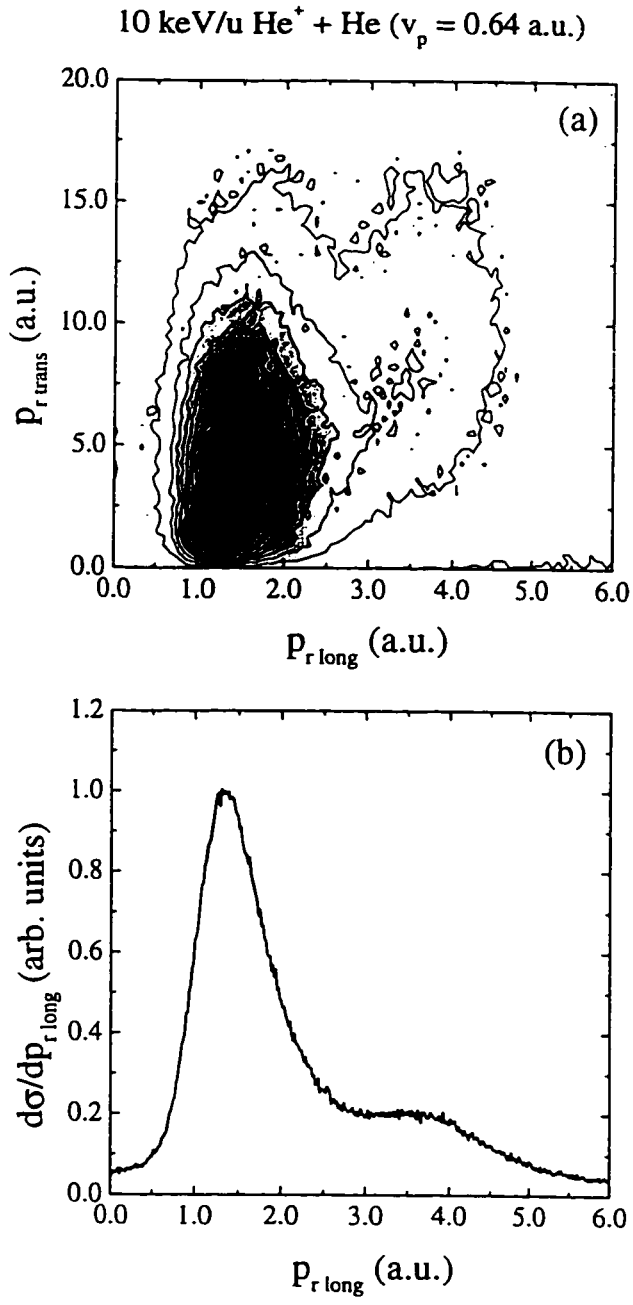

Figure 4.6: (a) Recoil-ion transverse momentum vs longitudinal momentum for 10 keV/u He^+ + He. Note that the two scales are different for convenience. (b) Longitudinal transverse momentum (summed over all transverse momentum).

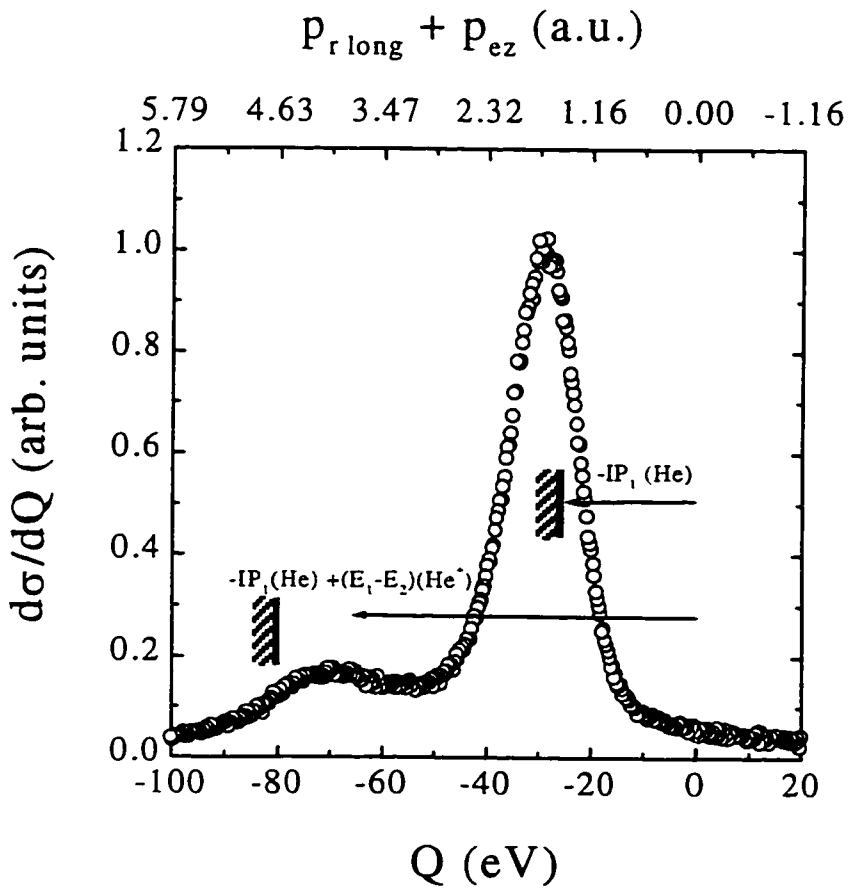

Figure 4.7: Q-value distribution in the collision 10 keV/u He^+ + He. This distribution was calculated from the longitudinal momentum distribution presented in Fig. 4.6(b) using Eq. (4.2).

momentum or -70 eV in the Q value. This peak corresponds to ionization of He accompanied by excitation of either the target ion or the projectile ion from $n = 1$ to $n = 2$. The tail of this peak indicates the possibility of excitation to higher levels. The distribution in Fig. 4.7 can be compared directly to the distributions obtained using translational energy spectroscopy. For example you can compare the distribution in Fig. 4.7 to the distributions presented earlier in Fig. 2.4 and Fig. 2.5. Although the impact velocity for the data presented in Fig. 2.4 and Fig. 2.5 is well below the velocities in the present experiment, it is noted that the distributions are very similar. The role of the ionization-excitation mechanism is noted to be of similar importance at these different velocities. It is interesting to note that the scattering angles corresponding to ionization-excitation are considerably larger than those for ionization events without excitation as can be seen in Fig. 4.6(a). This indicates that in general, to have excitation in addition to ionization, impact parameter should be smaller than what is needed, on the average, for pure ionization without excitation. This also agrees with early experiments at low velocities using translational energy spectroscopy. One can compare the distribution in Fig. 4.6(a) to the angular distributions in Fig. 2.6. In analyzing the results of this experiment, we did not discriminate against events of ionization accompanied by excitation. The contribution of these events to the electron spectra is small.

An event of double electron ejection from the target atom is discriminated against since we gate on the He^+ peak in the recoil-ion time-of-flight spectrum. On the other hand, an event involving single electron ejection from the target accompanied by the projectile electron ejection is not discriminated against. However, such an event will result in an energy loss by the projectile equal to IP(He)+IP(He^+) which is about 79 eV. By looking at the Q-value distribution in Fig. 4.7, we find that the contribution

of such a process is small. Detailed studies of projectile electron ejection in low energy collisions have been carried out by many groups. For example, refer to Hsu *et al.* [137, 138]

A "side view" of the ejected electrons is presented in Fig. 4.8(a). The same range of recoil-ion momentum is used. As expected, this distribution is symmetric around the inter-nuclear axis. It is interesting to see that the distribution is very narrow. This indicates that the ejected electrons prefer to stay in the scattering plane. This can be understood as the ejected electrons try to follow the nuclear motion which is in the scattering plane by definition. A projection of Fig. 4.8(a) similar to Fig. 4.9(b) is given in Fig. 4.8(b). It shows clearly the collimation of the ejected electrons to the scattering plane.

A top view of the ejected electron momentum distribution is given in Fig. 4.9(a). This spectrum includes all electrons in coincidence with recoil ions that have transverse momentum in the range of 0 - 15 a.u. and emitted parallel to the electron detector. It should be noted that most of the scattered recoil ions have transverse momentum below 15 a.u. (see Fig. 4.5). The recoil ion is chosen to be ejected in the negative y direction, indicated by an arrow. It is noted that most of the electron distribution is in the forward direction and with velocities that lie between the target velocity and the projectile velocity. This agrees with the results described in the previous chapter with no determination of any scattering planes. The distribution is narrow in the transverse direction, yet it shows a local minimum along the inter-nuclear axis. The branch of the distribution in the same direction as the recoil ions is less intense than in the opposite direction. To see this "two-branch" distribution in a more quantitative way, a slice of the two-dimensional distribution with width of $0.25v_p$ was taken at $v_{ez}/v_p = 0.5$ and projected sideways. The result

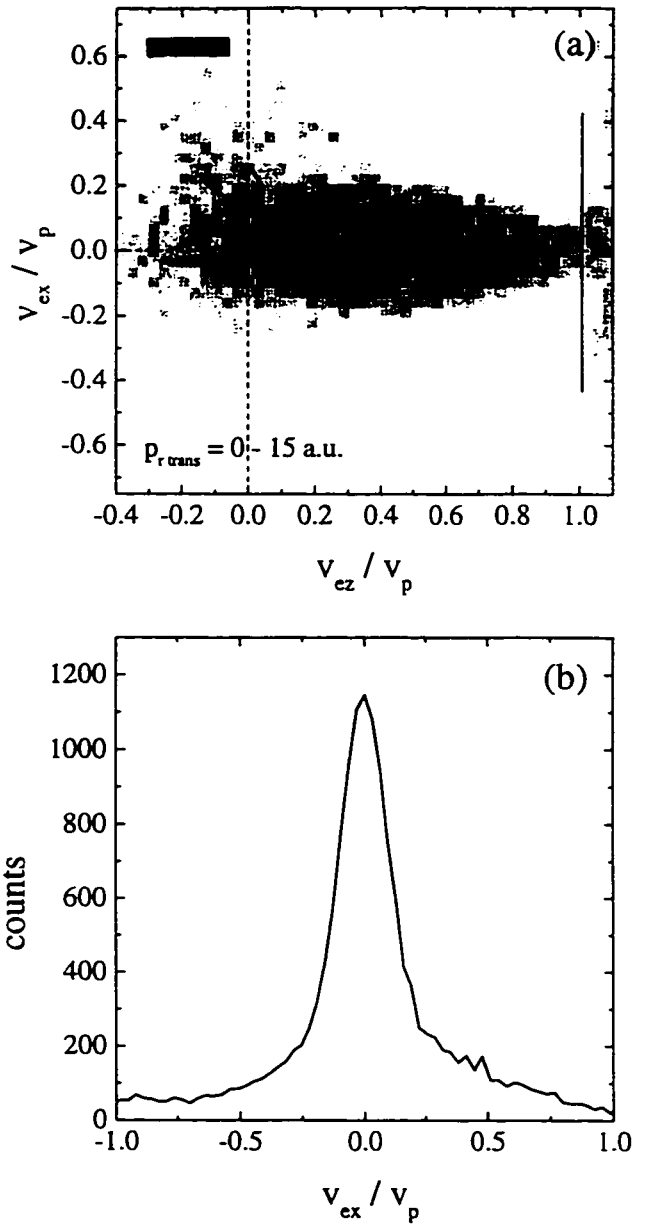

Figure 4.8: (a) Side view of ejected electron momentum distribution in the collision 10 keV/u He^+ + He. The electron velocity components v_{ez} and v_{ex} are scaled by the projectile velocity (v_p). Dashed lines are used to guide the eye to zero-velocity electrons in both directions, parallel and perpendicular to the ion beam. A solid line guides the eye to the projectile velocity. The rectangle represents the error bars in the two directions. (b) Transverse projection of the distribution in (a) for a slice centered at $v_{ez}/v_p = 0.5$.

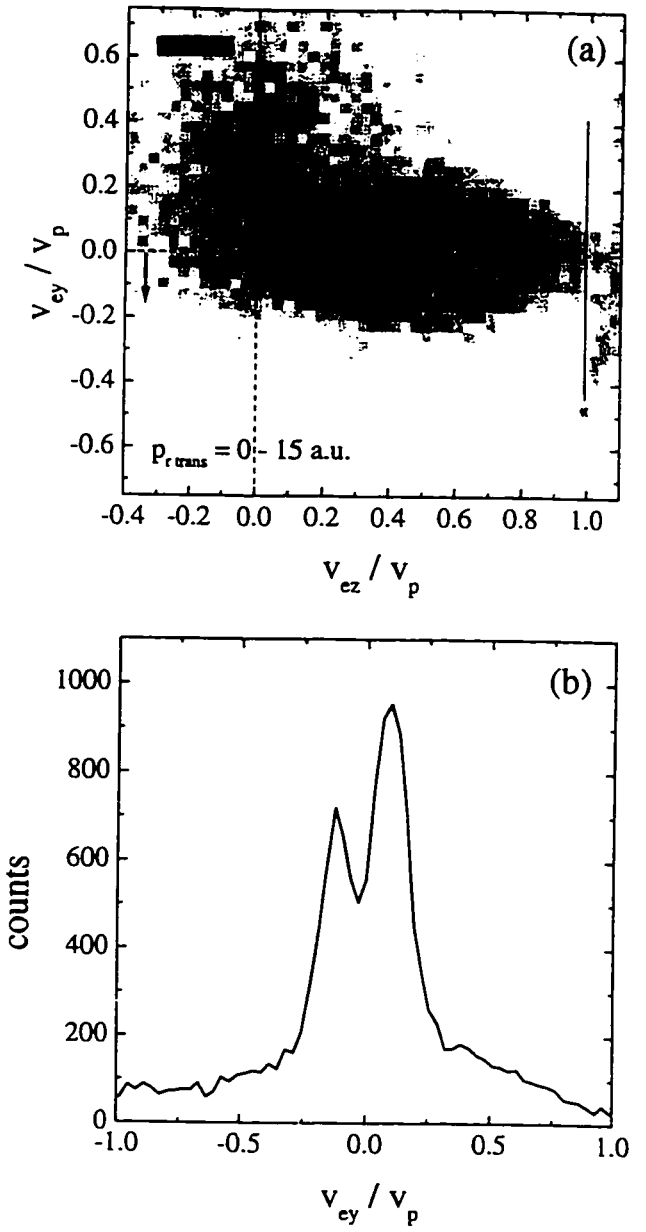

Figure 4.9: (a) Top view of the ejected electron momentum distribution in the collision 10 keV/u He^+ + He. The electron velocity components v_{ez} and v_{ey} are scaled by the projectile velocity (v_p). Dashed lines are used to guide the eye to zero-velocity electrons in both directions, parallel and perpendicular to the ion beam. A solid line guides the eye to the projectile velocity. The rectangle represents the error bars in the two directions. (b) Transverse projection of the distribution in (a) for a slice centered at $v_{ez}/v_p = 0.5$.

of this projection is shown in Fig. 4.9(b).

A similar kind of structure was reported by Dörner *et al.* [49] for 5 - 15 keV p + He. In that work this structure was qualitatively explained in terms of hidden crossing theory. According to this explanation [32, 68], two series of transitions can contribute to the saddle-point-ionization mechanism. The first is the so called $T00$ series and involves no angular momentum transfer and thus leads to a σ state with a maximum on the saddle. The second series is $T01$ series which starts with a rotational coupling from $2p\sigma$ to the $2p\pi$ orbital of the quasi-molecule and leads to a π state with a node on the saddle. The two states should add coherently, which leads to the observed asymmetry depending on the relative amplitudes of the two states. In this experiment we show that this behavior is not limited to p-He collision system. Rather it can be observed in a variety of other systems.

To study the impact-parameter dependence of the emitted electron momentum distribution in the scattering plane, the electron distribution was gated on different ranges of recoil-ion transverse momentum. The results are shown in Fig. 4.10. In the figures (a-e), the top view of the emitted electrons is gated on different ranges of transverse momentum and hence impact parameters. In these figures the recoil-ion transverse momentum increases by moving from figure (a) to figure (e) and therefore, the impact parameter decreases by moving the same way (according to Eq. (4.4)). The corresponding projections of each distribution at $v_{ez}/v_p = 0.5$ is given in the Figs. 4.10(f-j). The figures show that the distribution exhibits the two off-axis peaks in all ranges of impact parameters. However, the distribution becomes more symmetric at smaller impact parameters (larger recoil-ion transverse momentum). This suggests that the relative contributions of σ and π orbitals depends on the impact parameter. At small impact parameters the π orbital is dominant over σ

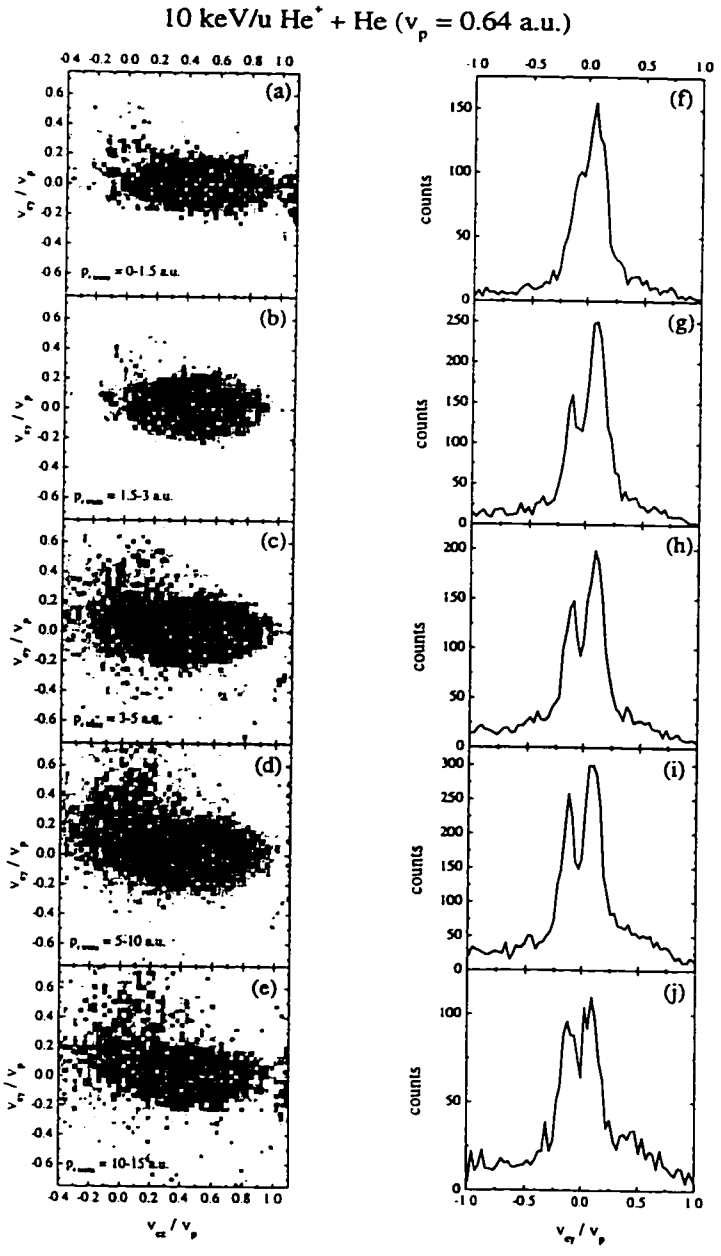

Figure 4.10: Top view of the ejected electron momentum distribution in the collision 10 keV/u He^+ + He. The electron-velocity components v_{ez} and v_{ey} are scaled by the projectile velocity (v_p). The impact parameter decreases in the figures by moving from (a) to (e). slices at $v_{ez}/v_p = 0.5$ projected sideways are given in the figures (f - j).

orbital. This leads to a symmetric distribution around the inter-nuclear axis. At large impact parameters the σ orbital contribution increases relatively, leading to the asymmetry of the distribution.

Fig. 4.11 shows the recoil-ion transverse momentum distribution for projectile velocities in the range 0.45 - 1.00 a.u. The figure shows a strong change in the size and the shape of the distribution as the projectile velocity is changed. The distribution is wide at low impact velocity and becomes very narrow and peaked at larger impact velocities. This is partly due to a kinematic effect that can be explained by the Rutherford scattering formula (Eq. (4.2)). For collisions with the same impact parameter (b), the recoil ion transverse momentum $p_{r\perp}$ is inversely proportional to the impact velocity v_p. This leads to wider $p_{r\perp}$ distributions at smaller projectile velocities. However, this effect is not enough to explain all the changes in the distribution. Specifically, we can identify two contributing shapes: a large $p_{r\perp}$ component which becomes stronger for at small v_p ($v_P \leq 0.64$ a.u.) and small $p_{r\perp}$ component which is dominant at large v_p ($v_P \geq 0.64$ a.u.). This suggests that the low velocity ionizing collisions happen at relatively small impact parameters compared to higher velocity ($v_P \sim 1$ a.u.) ionizing collisions. This is in agreement with the idea of the "molecular" nature of ionization in low velocity collisions and the onset of a large-b process at high v_p.

A top view of the emitted electrons at different impact energies (0.45 - 1.00 a.u.) is given in Fig. 4.12 . Except for the highest velocity, the distributions look similar. The distribution tends to become more symmetric around the inter-nuclear axis by moving toward smaller impact velocities. On the other hand, σ transitions become more important at larger impact velocity which leads to asymmetric distributions.

The persistent π-shape of these spectra appears to be clear evidence for the

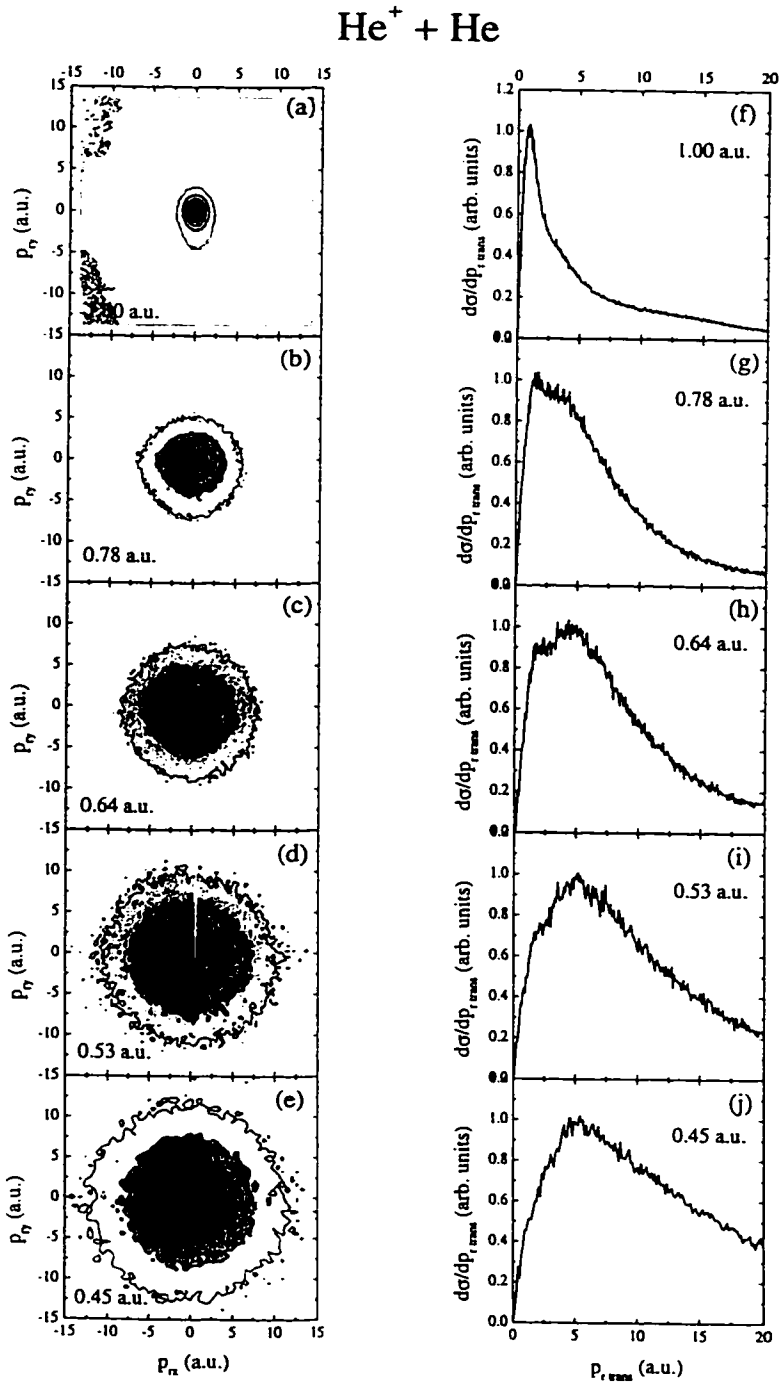

Figure 4.11: Recoil-ion transverse momentum distribution in the collision He^+ + He leading to single ionization at projectile velocities v_p = 0.45 - 1.00 a.u.

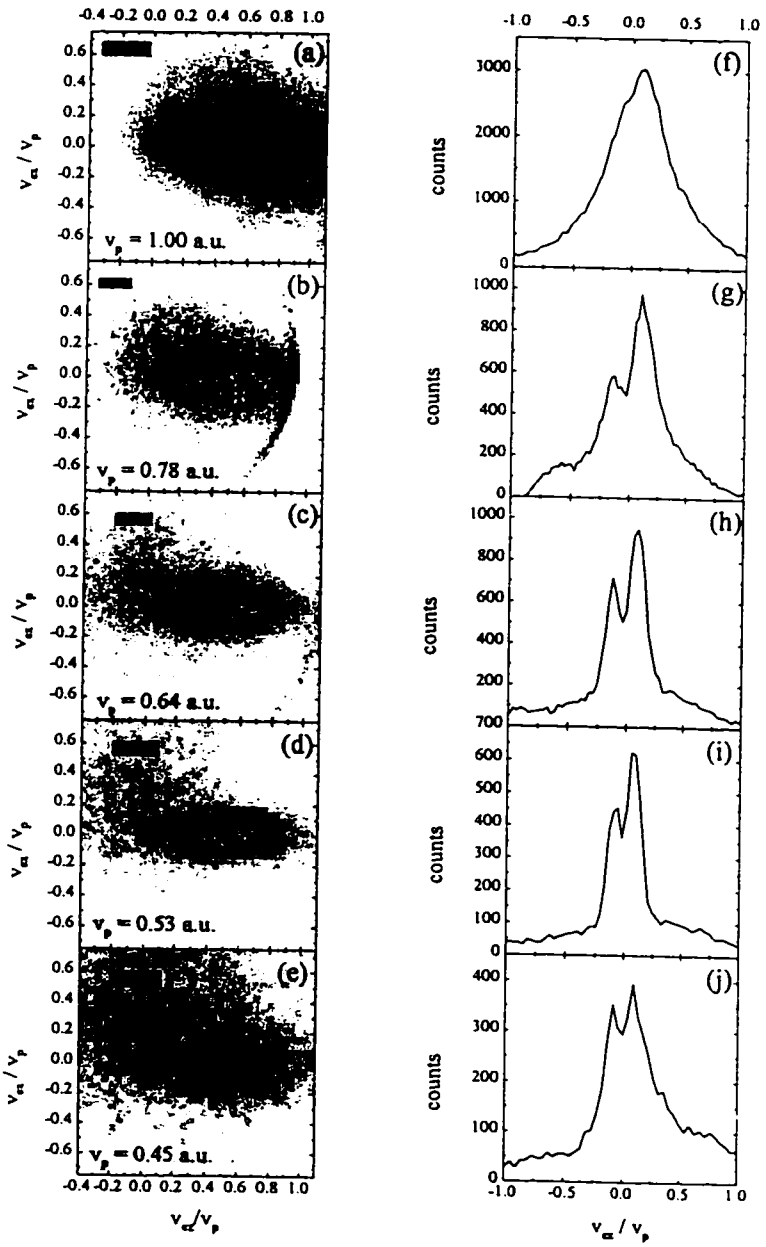

Figure 4.12: Top view of the ejected electron momentum distribution in the collision of He^+ + He at v_p = 0.45 - 1.00 a.u. The electron velocity components v_{ez} and v_{ey} are scaled by the projectile velocity (v_p). The impact parameter decreases in the figures by moving from (a) to (e). The rectangles represent the error bars in the two directions. Slices at v_{ez}/v_p = 0.5 projected sideways are given in the figures (f - j).

dominance of the promotion of a π orbital into the continuum as the basic ionization process. We attribute this to a small-b $2p\pi - 2p\sigma$ coupling, followed by a T-type promotion of the $2p\pi$ electron. This mechanism appears to dominate the ionization process for all the studied velocities. The contribution of the σ-type orbitals results in an asymmetry of the distributions which is dependent on the impact velocity and the impact parameter.

4.2.2 He^{2+} + He

The He^{2+} + He system was studied over the same range of velocity as He^{+} + He. In Fig. 4.13 we show the recoil-ion transverse momentum distributions in the range of impact velocity 0.45 - 1.00 a.u. In general, the distributions are similar to those of He^{+} + He. In particular, we notice again the two components are forming the distribution: a small $p_{r\perp}$ component visible for $v_P \geq 0.85$ a.u., which contributes to a small fraction of the total cross section, and a large $p_{r\perp}$ component for $v_P \leq 0.70$ a.u. which dominates the distribution. While the small $p_{r\perp}$ component is absent in the lowest velocity distribution (0.45 a.u.), its contribution to the total cross section is the largest at the highest velocity (1.00 a.u.). A systematic development of the small $p_{r\perp}$ component can be seen in the distributions by increasing projectile velocity.

An artifact can be seen in the distributions presented in Figs. 4.13(b-d). A small peak can be seen about 5 a.u. to the right of the center of the two-dimensional distribution. This peak is due to the nonzero detection efficiency of the electron detector for photons. In this range of velocity, the single capture channel is stronger than single ionization. A very probable process is single capture to an excited state followed by radiative stabilization:

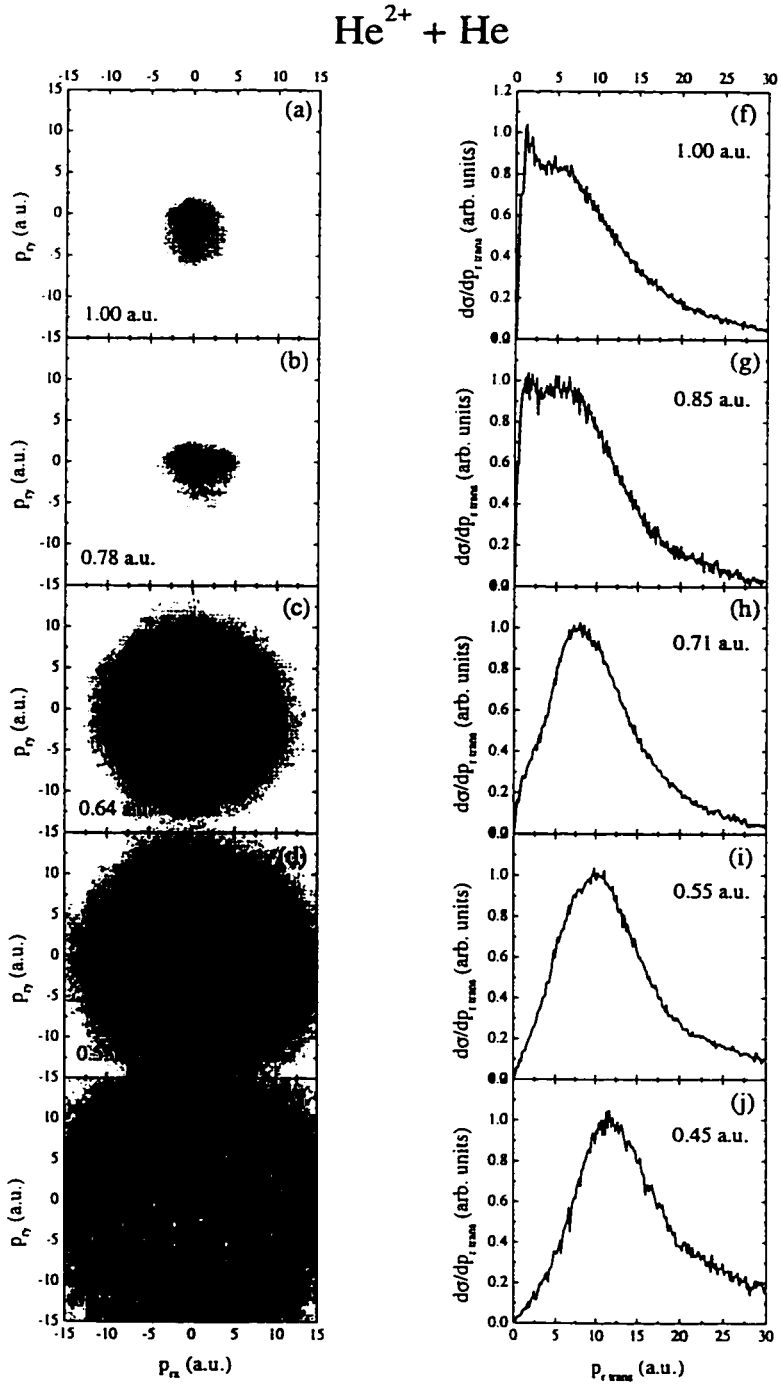

Figure 4.13: Recoil-ion transverse momentum distribution in the collision He^{2+} + He leading to single ionization at projectile velocities v_p = 0.45 - 1.00 a.u.

$$He^{2+} + He \longrightarrow (He^{+})^{*} + He^{+} \; (\longrightarrow He^{+} + He^{+} + \gamma)$$

The emitted photons have a chance to be detected by the (close) electron detector in coincidence with the recoil ion He^{+}. The p_{rx} is calculated from the time of flight of the recoil ions. The electron (photon) time signal is used to start the TAC which measures the time of flight of recoil ions. Since the electrons hit the electron detector about seven nanoseconds after their birth, there will be a displacement in time and therefore in p_{rx} between recoil ions in coincidence with photons and in coincidence with electrons. This produces the 5 a.u.-shift in momentum that can be seen in the distributions. In integration to calculate the radial distribution presented in Figs. 4.13(f-j), we did not include this (photon) peak.

In comparing the distributions for this system (Fig. 4.13) and the distributions for He^{+} + He (Fig. 4.11), we notice that the distributions for the He^{2+} systems are wider than those for He^{+} systems. Mostly this can be explained by the larger charge of the projectile which produces larger scattering angles according to Eq. (4.4). In general, ionization for the two systems happens over a similar range of impact parameters (peaked near 0.8 a.u.).

Fig. 4.14 shows a top view of the ejected electron-momentum distribution for this system. In general the distributions are similar to the distributions for the He^{+} systems, except that the two off-axis peaks can be recognized only for the two velocities 0.55 and 0.71 a.u. One striking difference is that while the distribution is almost symmetric around the inter-nuclear axis for collisions at $v_p = 0.71$ a.u., it is asymmetric at $v_p = 0.55$ a.u. and it prefers the same direction of the recoil ions. This is opposite to the general behavior seen in the He^{+} electron distributions. No explanation of this behavior is available at this moment.

To have a more quantitative comparison of this symmetry for the two systems,

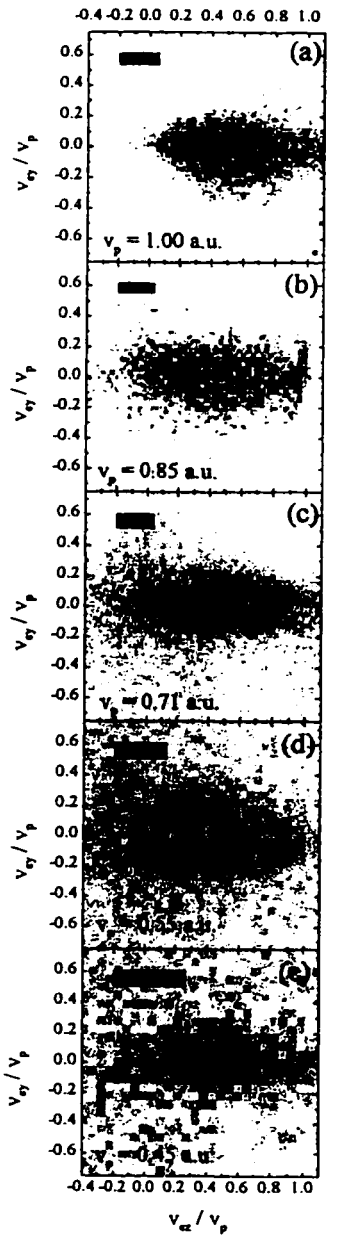

Figure 4.14: Top view of the ejected electron-momentum distribution in the collision of He^{2+} + He at v_p = 0.45 - 1.00 a.u. The electron velocity components v_{ez} and v_{ey} are scaled by the projectile velocity (v_p). The impact parameter decreases in the figures by moving from (a) to (e). The rectangles represent the error bars in the two directions.

we calculated the average transverse velocity of the electrons in a slice around the middle of the internuclear velocity. A transverse slice of width $0.25v_p$ was taken around $v_{ez}/v_p = 0.5$. This slice was projected sideways to produce distributions of v_{ey}/v_p like the one shown, for example, in Fig. 4.12(f - j). These distributions were used to calculate the average transverse velocity $\overline{v}_{ey}$ weighted by the projectile velocity v_p. The result is shown in Fig. 4.15. The results for p + He and He^+ + He are also presented for comparison. We define electron transverse velocity to be positive if the electron is emitted in the same direction of deflection as the projectile (opposite to the direction of the recoil ion). We note that in the two systems p + He and He^{2+} + He the average transverse velocity changes from one side to another. In He^+ + He it remains in the same side favoring the side of the projectile. One may guess that this oscillatory behavior is related to the bare ions (p and He^{2+}).

There is no physical argument to support this conclusion or to deny it yet, but we can use the following model [53, 54] to suggest a possible source of oscillation. One can write the final electron wave function as a superposition of model σ and π amplitudes. This can be written as [53, 54]

$$\Psi = \alpha|\pi> + \beta e^{i\phi}|\sigma> \quad , \tag{4.5}$$

where ϕ is the difference in phase between the two amplitudes and is given by

$$\phi = -Re\int_{t_o}^{\infty}[\varepsilon_\sigma(R) - \varepsilon_\pi(R)]dt = -\frac{1}{v_p}Re\int_{R_o}^{\infty}[\varepsilon_\sigma(R) - \varepsilon_\pi(R)]dR \quad , \tag{4.6}$$

where ε_σ and ε_π are the energies of σ and π paths along which the promotion occurs, respectively. t_o and R_o are constants. The integral in the last part of Eq. (4.6) ($\equiv \phi_o$) is independent of v_p. Therefore one can write

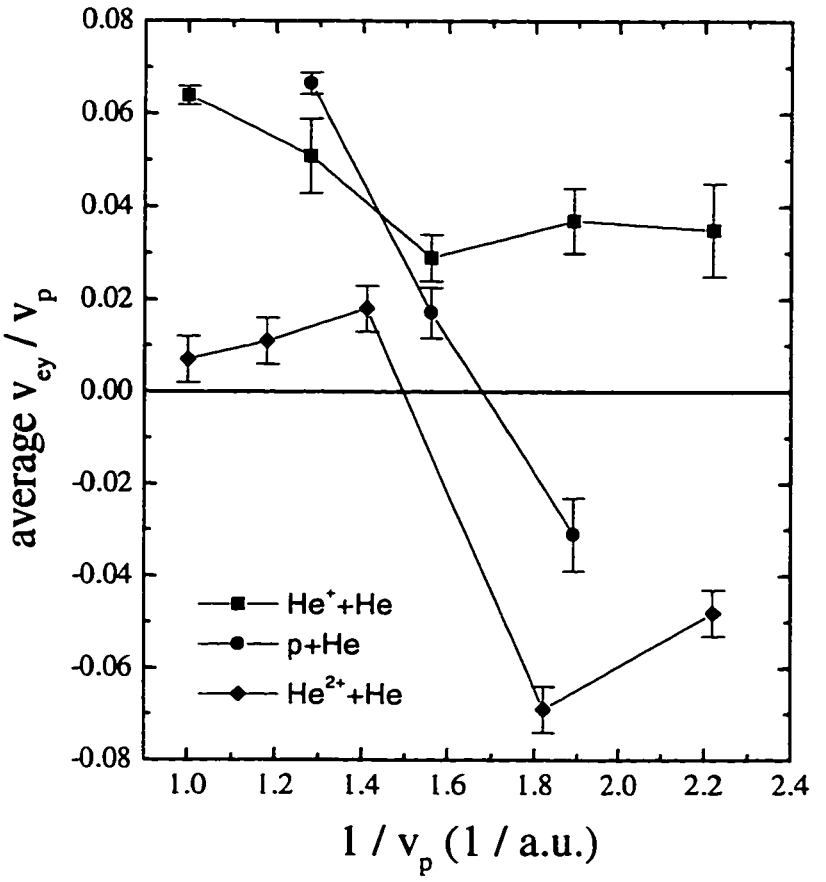

Figure 4.15: Average transverse velocity in the scattering plane for v_{ez} around $0.5v_p$ plotted versus the reciprocal of the projectile velocity v_p. The solid lines are to guide the eye. The electron transverse velocity is defined to be positive if the electron is emitted in the same direction of the deflected projectile (opposite to the direction of the recoil ion).

$$\phi = \frac{\phi_o}{v_p} \quad . \tag{4.7}$$

Therefore, the oscillation frequency depends on the constant ϕ_o and the reciprocal of the collision velocity v_p. The constant R_o and therefore the constant ϕ_o depend on the collision system. For instance, for the p + H system, it was found that [53, 54] $R_o \approx 2.2$ and $\phi_o = 8/\sqrt{R_o} \approx 5.4$. This seems in a good agreement with the results for the p + He system. However, a detailed consideration of the system seems to be of critical importance. No work within the theory of hidden crossings that take into consideration the exact nature of the collision system is reported yet. Specifically, no explanation of why ϕ appears to be velocity dependent for p and He^{2+} projectiles (as Eq. (4.7) predicts) but not for He^{+} has appeared.

4.2.3 C^{6+} + He

In this section we study single ionization of He by C^{6+} impact at three velocities; 1.63, 1.36, and 1.17 a.u. The electron capture channel is strongly dominant over ionization in this range of velocity [135, 136, 139, 48]. We can extract the ratio of single ionization to single capture for C^{6+} on He at these three velocities from the measurements of Wu *et al.* The result is $\sigma_{si}/\sigma_{sc} \simeq$ 0.004, 0.014, and 0.083 for v_p = 1.17, 1.36, and 1.63 a.u., respectively. This results in experimental difficulties, especially from photon detection by electron detector. Those photons come from radiative stabilization of electrons captured into excited states as explained on page 99. Fortunately, the electron peak and the photon peak are separated in time by about 7 nsec, and the peaks are thus separated in the x component of the recoil-ion momentum. This made it possible to exclude the contribution of photons to electron spectra.

Fig. 4.16 shows the recoil-ion transverse momentum ($p_{r\perp}$) vs longitudinal momentum ($p_{r\parallel}$) for the collision C^{6+} + He at $v_p = 1.36$ a.u. The figure shows that most of the recoil ions are pushed backward. This balances the electron momentum which is mostly in the forward direction as we will see later. The transverse momentum is seen to be very small compared to the transverse momentum in the collisions of He^{+} and He^{2+} which were also at smaller projectile velocities. In Fig. 4.17 we show the transverse momentum distributions for the three velocities under study. We see that the recoil-ion transverse momentum has very little dependence on the projectile velocity over this range of velocities. The peak of the distribution is about 0.7 a.u. for the three velocities. This disagrees with the measurements reported by Wu *et al.* [48] for O^{8+} on He at $v_p = 1.34$ a.u. which showed a transverse momentum distribution peaked about 3.0 a.u. for both single ionization and single capture. Applying the Rutherford scattering formula to our results yields an impact-parameter distribution that is peaked about 12 a.u. This is in a strong disagreement with the close coupling calculations by Wang *et al.* [136]. Wang *et al.* found that for the collision system C^{6+} + He at $v_p = 1.40$ and 1.64 a.u., both single electron capture and single ionization have impact-parameter distributions which are similar and peaked about 3.0 a.u. This favors Wu's results. On the other hand, Wu's measurements of the recoil-ion transverse momentum and Wang's calculations of the impact parameter distribution for single electron capture by highly charged ions are in strong disagreement with extensive unpublished measurements done recently by our group. We measured the recoil-ion transverse momentum distributions for Ar^{8+}, Ar^{16+}, and Ne^{10+} over wide range of velocities. From our results we can estimate that most of the capture events happen with impact parameters of about 10 a.u. This disagrees with the previously mentioned results. However, our recoil ion transverse momen-

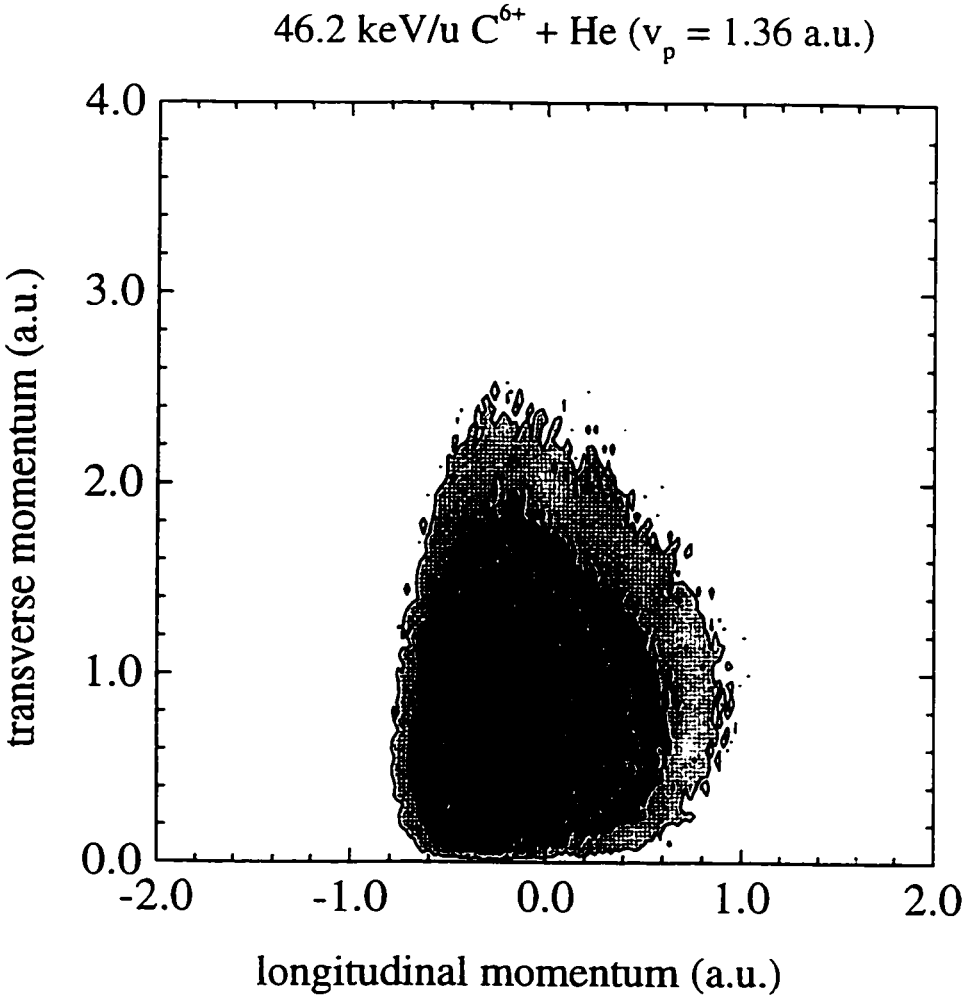

Figure 4.16: Recoil-ion transverse momentum ($p_{r\perp}$) vs longitudinal momentum ($p_{r\parallel}$) for the collision C^{6+} + He at v_p = 1.36 a.u.

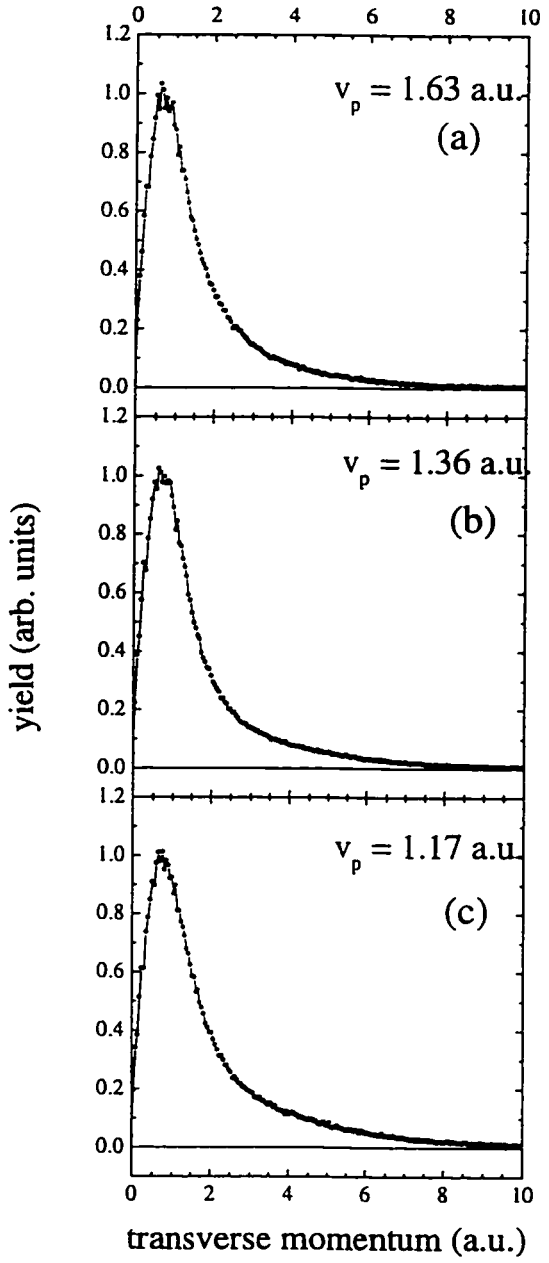

Figure 4.17: Recoil-ion transverse momentum for the collision C^{6+} + He at v_p = 1.63, 1.36, and 1.17 a.u.

tum distributions agree with the distribution in the collision of Ne^{10+} + He at v_p = 2.0 a.u. calculated using the CTMC method and reported by Olson *et al.* [140].

In Fig. 4.18 we present the two-dimensional electron-momentum distribution for v_p = 1.63 a.u. A top view of the emitted electrons (in the scattering plane) is given in Fig. 4.18(a). A side view of those electrons is given in Fig. 4.18(b). The spectrum shown in Fig. 4.18(c) is averaged over all azimuthal angles, and thus has no scattering plane defined. The last distribution can be compared to the distributiion obtained in the first-generation-experiments for the same system, shown in Fig. 3.10(a) on page 64. The distribution in Fig. 4.18(c) is narrower than the one in Fig. 3.10(a) since the latter has no limit on recoil ion transverse momentum while the former is gated on recoil ions with transverse momentum between 0 and 1.8 a.u. As we will see later, recoil ions with large $p_{r\perp}$ are in coincidence with electrons with relatively larger v_{ez} and v_{ey}. Therfore, including those events contributes to making the distribution wider in both directions.

The distribution as noted before is strongly collimated in the forward direction. A very small fraction of the electrons are emitted in the backward direction. The distribution in the scattering plane is noted to be asymmetric. More electrons prefer to be scattered in a direction opposite to the direction of recoil ions, therefore in the direction of deflection of the projectile. This may be a dynamical signature of the electrons trying to follow the highly charged projectile ion. Similar asymmetry was calculated by Olson *et al.* [140] in the collision of Ne^{10+} + He at energies of 100, 300, 500 keV/u using the CTMC calculations.

Fig. 4.19 and Fig. 4.20 show similar distributions but with projectile velocities 1.36 and 1.17 a.u., respectively. In general the distributions at these two velocities show much less collision-plane correlated structure than does the highest velocity.

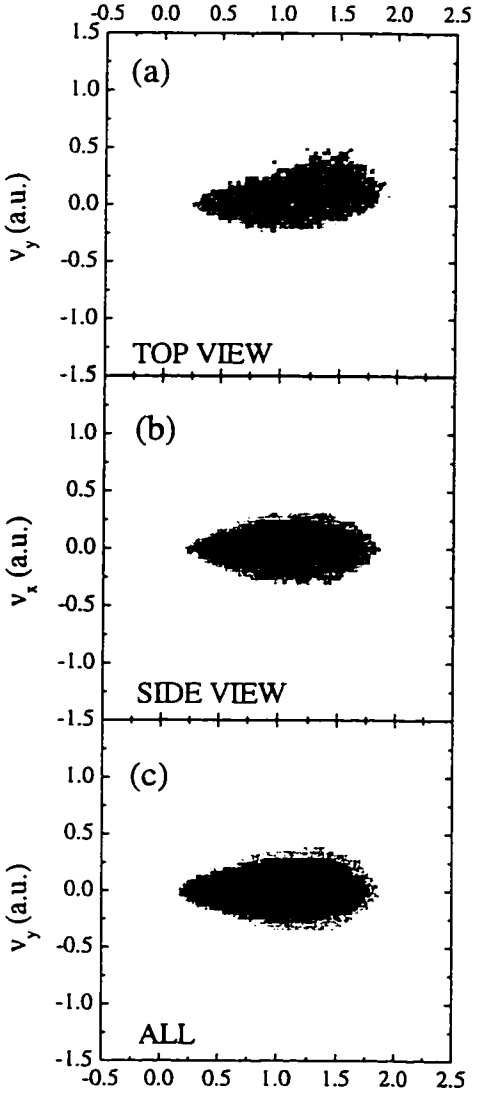

Figure 4.18: Top view (a), side view (b), and the total distribution (c) of the emitted electrons in C^{6+} + He at v_p = 1.63 a.u. In (c) no scattering plane is defined and the distribution is summed over all scattering planes. The transverse momentum of recoil ions is limited between 0 and 1.8 a.u. for technical reasons.

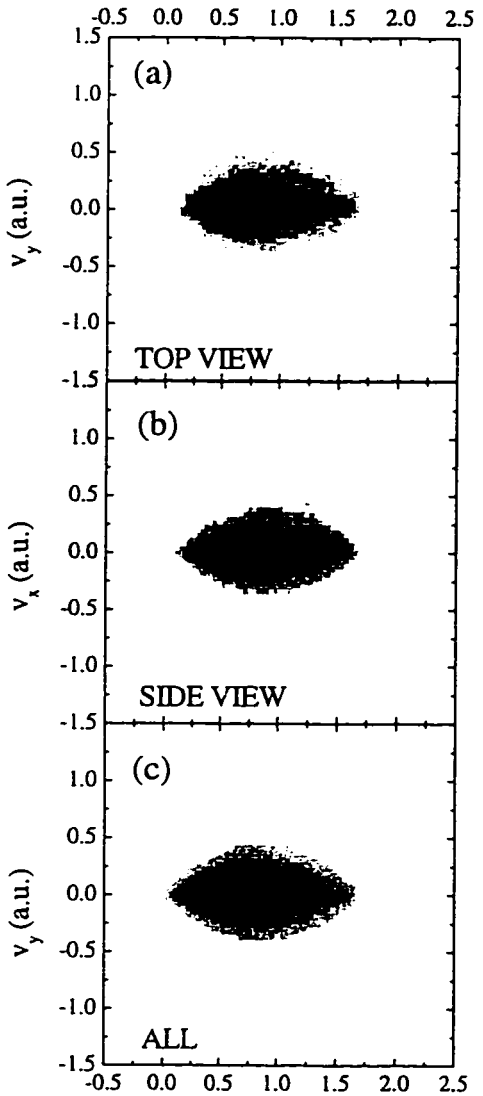

Figure 4.19: Top view (a), side view (b), and the total distribution (c) of the emitted electrons in C^{6+} + He at $v_p = 1.36$ a.u. In (c) no scattering plane is defined and the distribution is summed over all scattering planes. The transverse momentum of the recoil ions is limited between 0 and 1.8 a.u. for technical reasons.

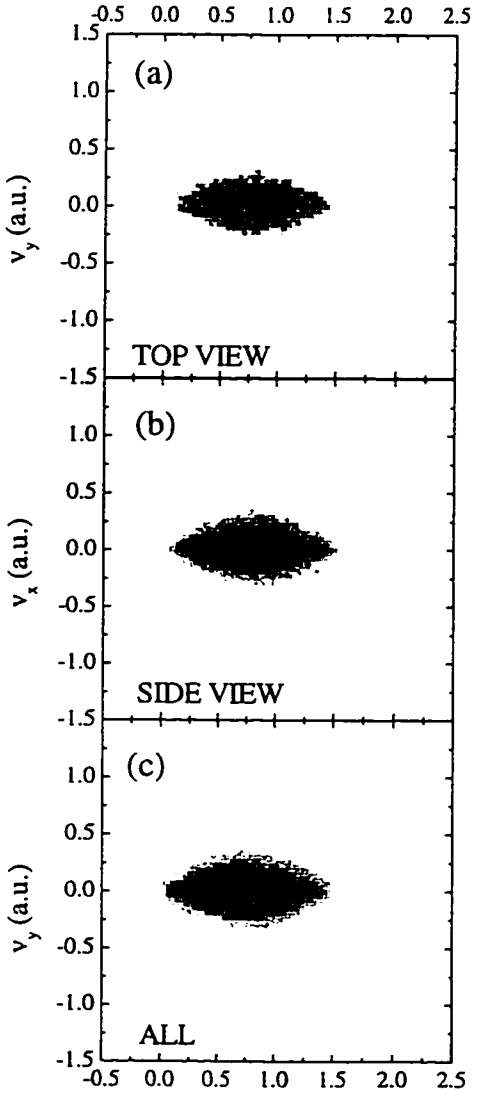

Figure 4.20: Top view (a), side view (b), and the total distribution (c) of the emitted electrons in C^{6+} + He at v_p = 1.17 a.u. In (c) no scattering plane is defined and the distribution is summed over all scattering planes. The transverse momentum of recoil ions is limited between 0 and 1.8 a.u. for technical reasons.

The distributions in the scattering plane are again noticed to be asymmetric but with less pile up near the projectile velocity.

Returning to the more interesting $v_p = 1.63$ a.u. case, in order to study the impact parameter dependence of the electron distribution in the scattering plane, we gated this distribution on different ranges of recoil-ion transverse momentum. The results are shown in Fig. 4.21. The impact parameter on the average increases in moving from Fig.(c) to Fig.(a). The sum of the three distributions (all impact parameters) is given in Fig.(d). It is noted that at large impact parameters (a), the distribution is narrow and nearly symmetric. In addition, a large fraction of the distribution is close to the target. In Fig.(b) the distribution becomes very asymmetric and a peak is noticed to grow near the projectile velocity. This peak indicates the increasing importance of the process of electron capture into the continuum. By decreasing the impact parameter, the distribution shifts even to velocities larger than the projectile velocity while the fraction of electrons near the target becomes smaller. We can see this behavior in a more quantitative way in Fig. 4.22 which shows the longitudinal and the transverse projections of these spectra. At the largest impact parameter range (Fig.(a)), the longitudinal momentum distribution is peaked about $v_{ez} = 1.0$ a.u. At smaller impact parameters (Fig.(b)) the distribution shifts toward the projectile velocity to peak about $v_{ez} = 1.6$ a.u. For the smallest impact parameter range the distribution has a peak about $v_{ez} = 1.8$ a.u. which is ahead of the projectile velocity. The sum is shown in Fig.(d) where the distribution is peaked about $v_{ez} = 1.4$ a.u., in agreement with the electron longitudinal momentum distribution obtained with the first generation experiment (see at Fig. 3.11(a) on page 66). This also agrees qualitatively with the CTMC predictions for 100 keV/u Ne^{10+} + He by Olson *et al.* [140] where it was found that the electron-momentum distribution is

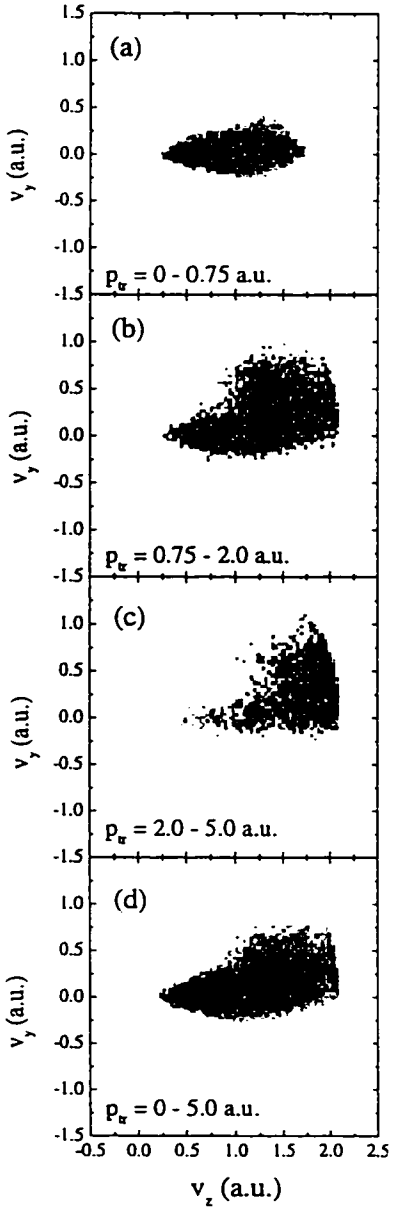

Figure 4.21: Top view of the emitted electrons in C^{6+} + He at v_p = 1.63 a.u. gated on different ranges of recoil- ion transverse momentum.

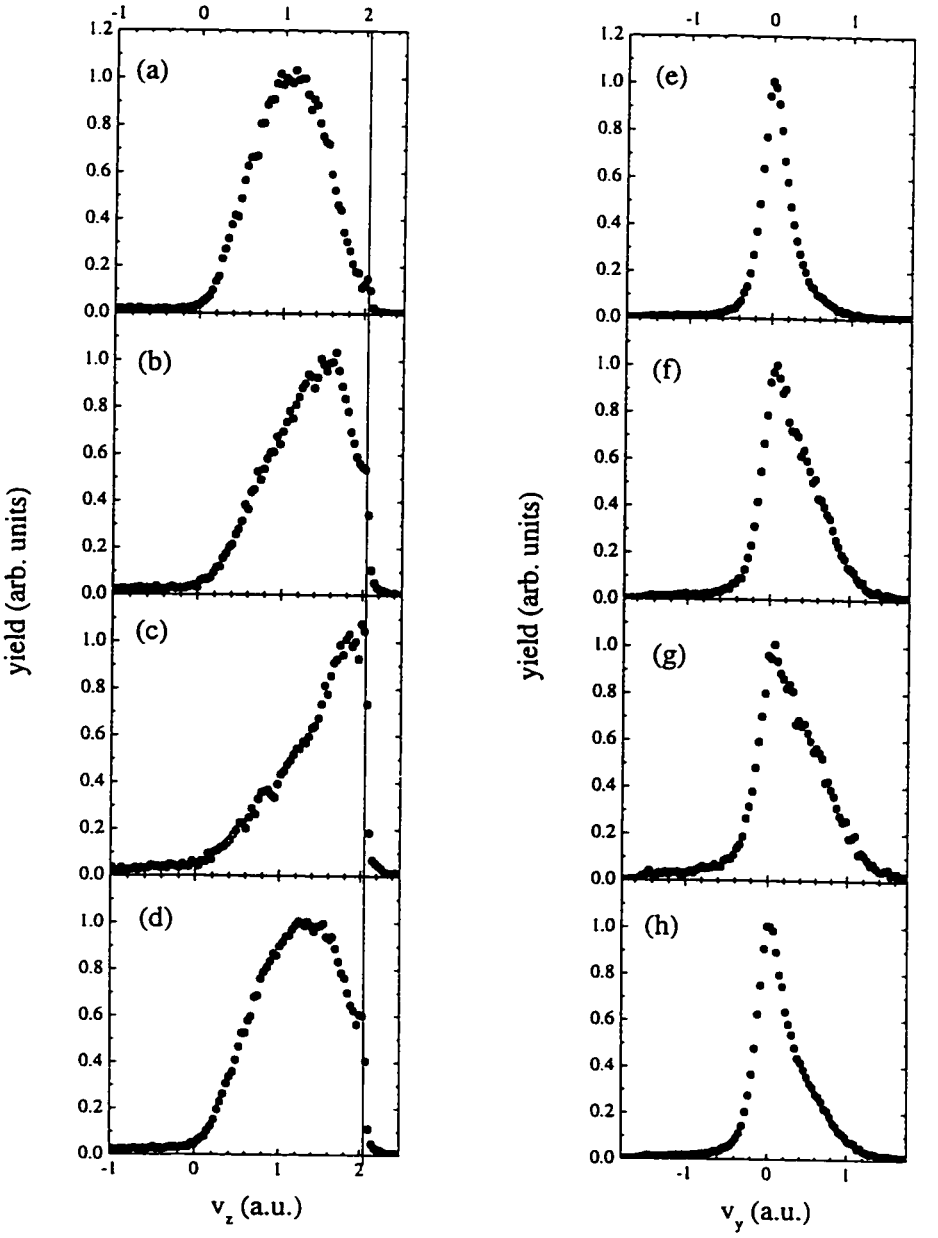

Figure 4.22: (a-d) Longitudinal projection of the 2-D distributions in Fig. 4.21. (e-h) transverse projection of the same distributions.

peaked near the target at large impact parameters while it tends to peak near the projectile at small impact parameters.

In addition we notice that, in the transverse direction, the distribution becomes wider at smaller impact parameters (look at Figs.(e-g)). This also agrees with the previously mentiond CTMC calculations by Olson *et al.* This behavior can be understood in a simple picture of the ionization process where close encounter collisions (small impact parameter) lead to larger "kick" of the electron to the continuum. Collisions with larger impact parameters (soft collisions) are more perturbative in nature and they lead to situations where the ionized electron stays in the vicinity of the mother atom.

The behavior at the two other velocities (1.36 and 1.17 a.u.) is somewhat different from what was seen at the highest velocity (1.63 a.u.). The top view of the ejected electrons gated on different impact-parameter ranges for the two velocities can be seen in Fig. 4.23 and Fig. 4.24. The distribution is noticed to become wider in both directions at smaller impact parameters. However, in the forward direction it does not favor the projectile velocity at small impact parameters. On the other hand, the fraction of electrons ejected in the backward direction increases at smaller impact parameters. Generally speaking there is a big difference in the behavior at $v_p = 1.63$ a.u. and at the two other velocities. We can see this more quantitativly in Fig. 4.25. and Fig. 4.26. where we can see the longitudinal distribution getting wider at smaller impact parameters but hardly shifting in any direction.

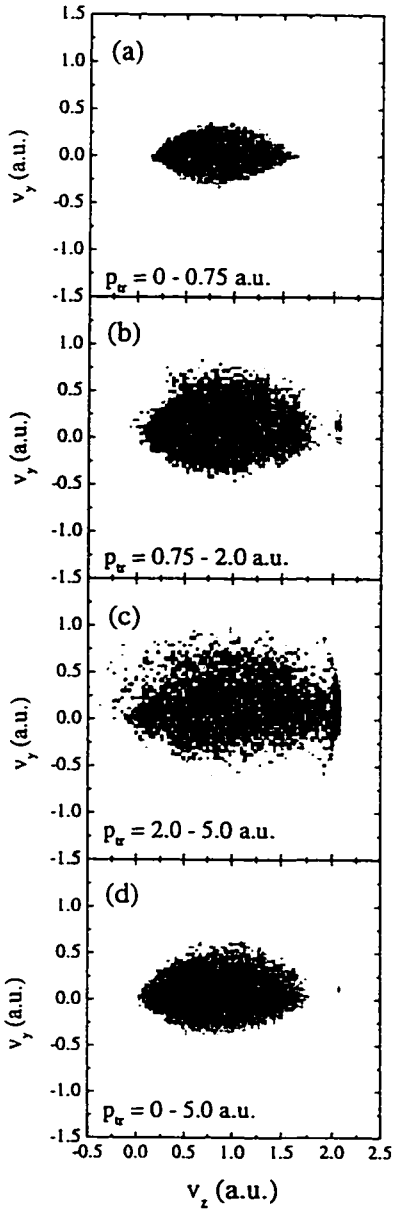

Figure 4.23: Top view of the emitted electrons in C^{6+} + He at v_p = 1.36 a.u. gated on different ranges of recoil- ion transverse momentum.

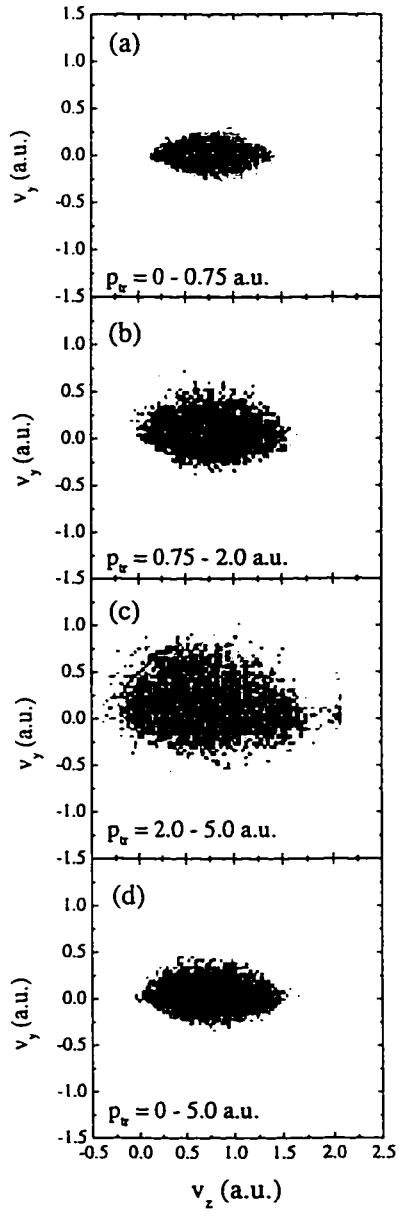

Figure 4.24: Top view of the emitted electrons in C^{6+} + He at $v_p = 1.17$ a.u. gated on different ranges of recoil- ion transverse momentum.

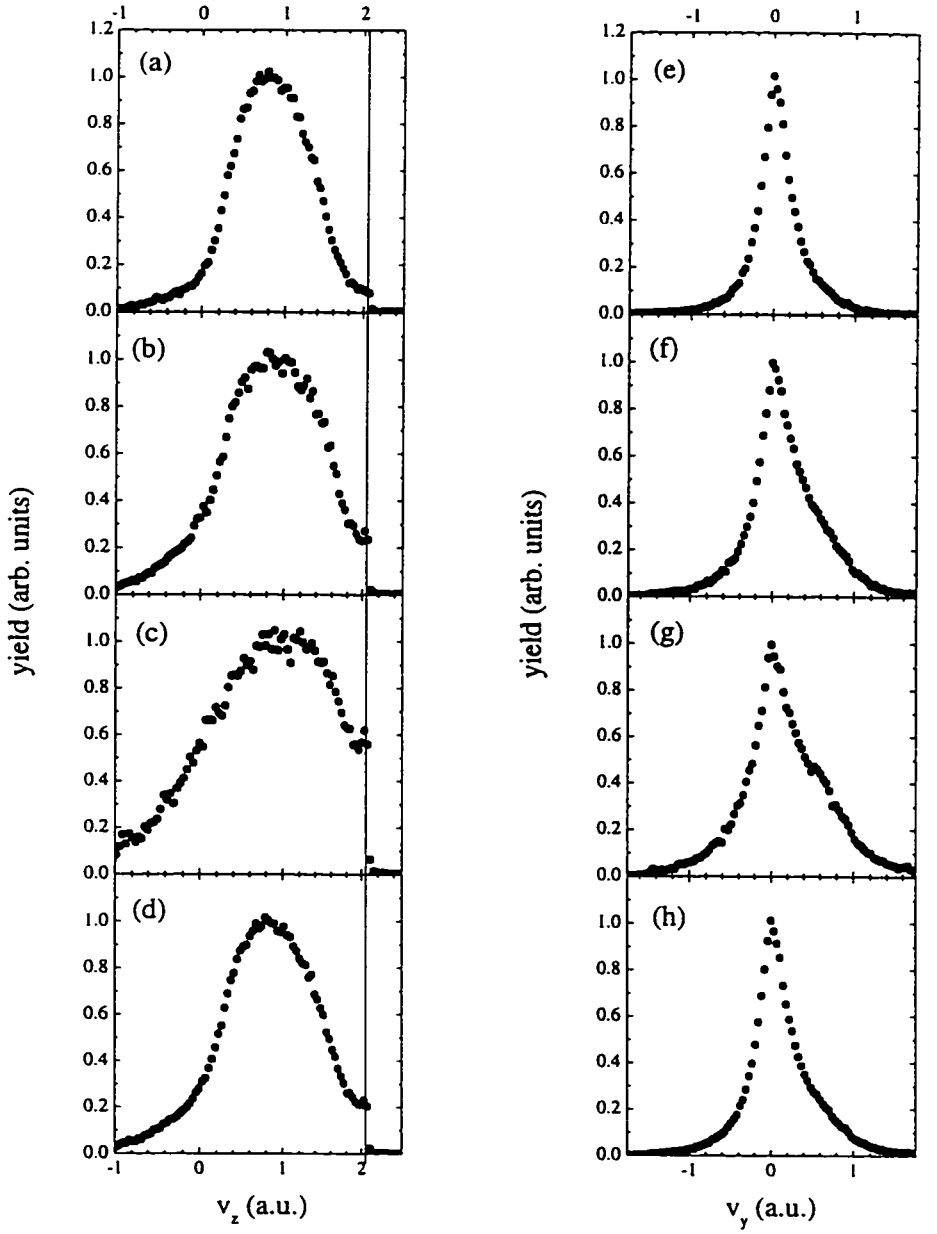

Figure 4.25: (a-d) Longitudinal projection of the 2-D distributions in Fig. 4.23. (e-h) transverse projection of the same distributions.

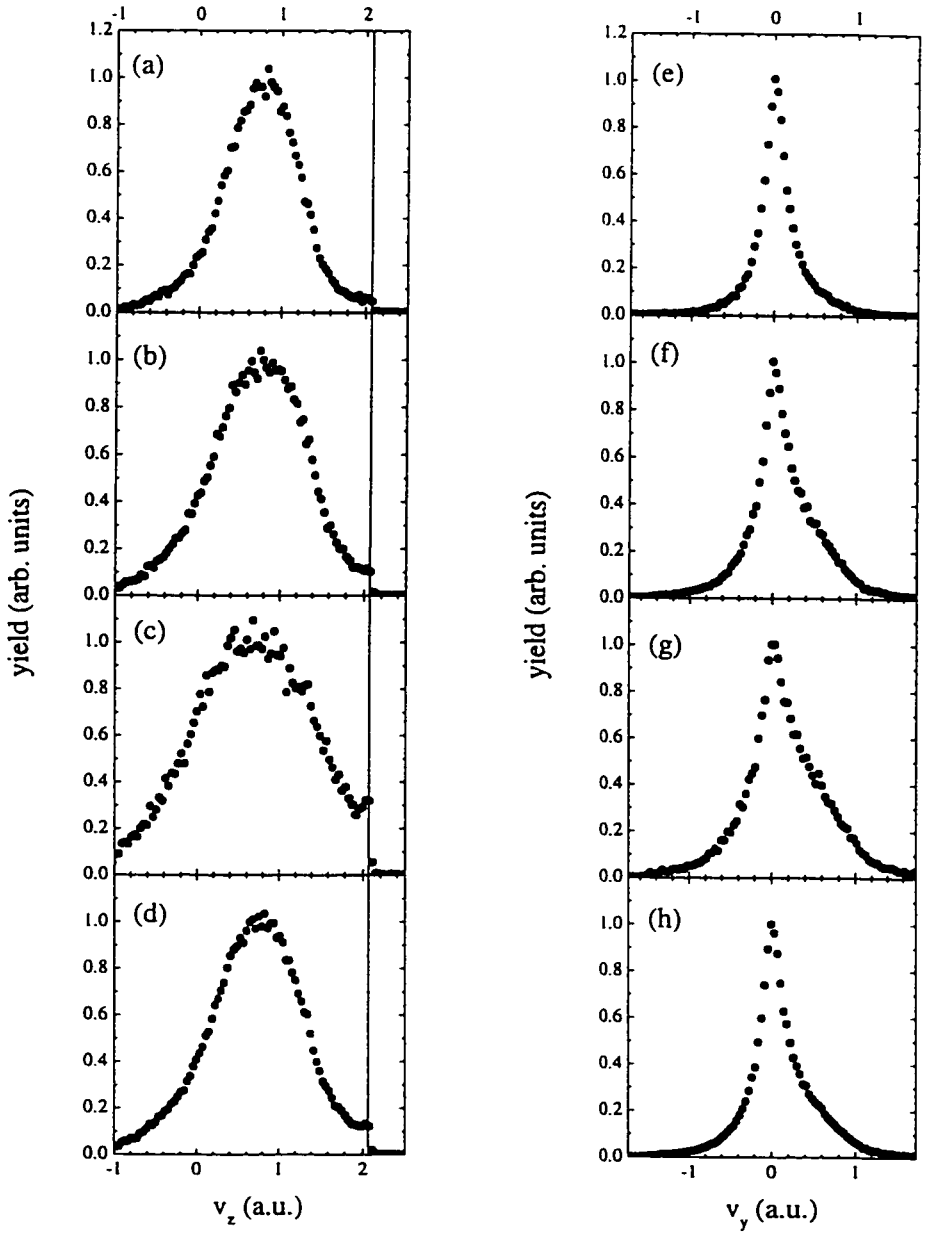

Figure 4.26: (a-d) Longitudinal projection of the 2-D distributions in Fig. 4.24. (e-h) transverse projection of the same distributions.

Chapter 5

Concluding Remarks

The results reported in this dissertation were an important addition to the general understanding of the ionization process in slow to intermediate ion-atom collisions. The imaging technique used in extracting and detecting slow electrons overcomes many of the problems encountered in measuring low energy electrons with traditional electron spectroscopy. Such a development was necessary, since the largest fraction of the ionization total cross section lies in a range of electron velocities near 0 eV. The simultaneous (coincident) detection of the momentum analysed recoil ions gave this technique a unique power which enabled us to determine the scattering plane, energy loss (Q-value), and impact parameter for collisions resulting in single electron ejection. Such highly differential measurements for electron momentum spectra revealed structures that were not possible to be seen using traditional techniques of electron spectroscopy. In addition the resulting distributions contained all the information in one picture unlike the traditional methods which involved determining the energy spectrum every time at a certain angle.

The first generation experiments, reported in chapter 3, ended the decade-long

debate about the velocity distribution of the ejected electrons for highly charged projectiles. It showed clearly that, for $q_p \geq 2$, the ejected electron momentum distributions have a projectile charge-state dependence that does not follow the simplest expectations for a saddle-point feature. This result showed that the simple picture of electrons "riding" on the saddle on the way to the continuum is too simple to explain the ionization process in the low velocity region where high-charge projectiles are involved. On the other hand, the velocity dependence for low charge states (p, He^+) in collisions with He and Ne indicates the possibility of an important saddle-point ionization contribution at low velocities, as the peak of the electron momentum distribution is seen to be centered near the saddle-point velocity.

The second-generation experiments were more powerful as they gave more differential results. Of major importance is the possibility of determining electron spectra in a certain scattering plane and at a certain imapct parameter. This series of experiments revealed the importance of the quasimolecular nature of the ionization process. This leads us to much earlier studies of the ionization process based on the quasimolecular orbitals. The older studies were conducted for projectile velocities well below the velocities in our experiments. To our surprise and against the common belief, quasimolecular features of the collision remain evident even when the projectile velocity becomes comparable to the "classical" orbital velocity.

While explicit theoretical calculations of the electron momentum distributions as a function of impact parameter have not yet been carried out for these systems, we can speculate on the major mechanisms which we believe our data reveal. Molecular promotion to the continuum seems to remain as the major mechanism of ionization even for projectile velocities compared to electron orbital velocity. In collisions of p, He^+, and He^{2+} with He, the promotion process starts via the rotational coupling

of the molecular orbital $2p\sigma$ and the molecular orbital $2p\pi$. In early studies it was mentioned that this coupling promotes the electron to excited bound (autoionizing) states. However, it can also lead to the continuum through a series of "hidden crossings" while the two Coulomb centers are receeding from each other. This process is termed the T process following the hidden crosssings theory. The T process is the quantum mechanical equivalent of the naive "classical" saddle-point-ionization mechanism. Other promotion paths are possible. Of major importance to the ionization process is the S series of hidden crossings which promotes the electron to the continuum while the two centers are appproaching each other.

The electron spectra for these three collision systems carry a unique structure. This structure includes a narrow ridge between the target and the projectile (in velocity space). A local minimum appears at the internuclear axis, with two peaks off the internuclear axis. We interpret this structure as a "signature" of the π orbitals through which the electron starts in its way to the continuum. This is an unmistakable evidence for the quasi-molecular nature of the ionization process in this range of velocities. Interference with other orbitals, mainly σ orbital, results in an asymmetry in the transverse distribution of the emitted electrons momentum.

For higher projectile charge states, no molecular orbital scheme is available. The electron spectra do not reflect any pattern that can be interpreted on a molecular basis. The velocity dependence of the momentum distributions indicates that the saddle-point ionization mechanism does not explain the ionization process for higher projectile charge states. On the other hand, the electron momentum spectra for higher charges shows an asymmetry in the transverse direction which results from the strong electron-projectile interaction. One can think of this interaction as a post-collision interaction. This picture agrees with the CTMC calculations and is

expected to hold for highly-charged projectiles at higher collision velocities.

For future research on this subject, we suggest extending the velocity range studied in our experiments. This is expected to give more universal picture of the ionization process as the projectile velocity is changed from very low to very high compared with the electron orbital velocity. Small adjustments in the prersent experimental setup can result in improving resolution in both the electron-momentum distributuion and the recoil-ion momentum distribution. A triple coincidence, by simultaneous detection of charge analysed projectile, can be useful in minimizing the contamination of the small-cross-section ionization process with other processes that have relativly large cross sections.

However, the biggest task lies on the shoulders of theoreticians. Up to this moment no rigorous theoretical treatment has been developed that could reproduce the measured differential cross sections in this range of velocity. Although the CTMC calculations and the CDW-EIS calculations give a good agreement with electron momentum distributions for low charge states and high velocities, they are poor at higher charge states and lower velocities. Several attempts by different authors are carried out at the moment. Up to this point the theory of hidden crossings remains the most acceptable basis to give qualitative explanations of our results.

Appendix A

Simulation of the Time-of-Flight-Position Spectrometer; First Generation

The program SIMION [131] allows us to do very accurate representation and simulation of the electrostatic system (spectrometer) used in extracting and detecting electrons and recoil ions. We used such simulation to calibrate the recoil-ion detector and the electron detector. In addition it was used to calculate the time of flight of recoil ions and electrons which was in a very good agreement with calibration based on first principles.

An illustration of this simulation is given in Fig. A.1. where we can see the extraction of electrons and recoil ions under a field of 420 V/cm. 7 electrons with energy of 30 eV are extracted. The angle between the direction of the projectile ion beam and the initial direction of every electron is varied between 0 and -180 degrees in steps of 30 degrees. Time markers are indicating every 1 nsec of the time-of-flight.

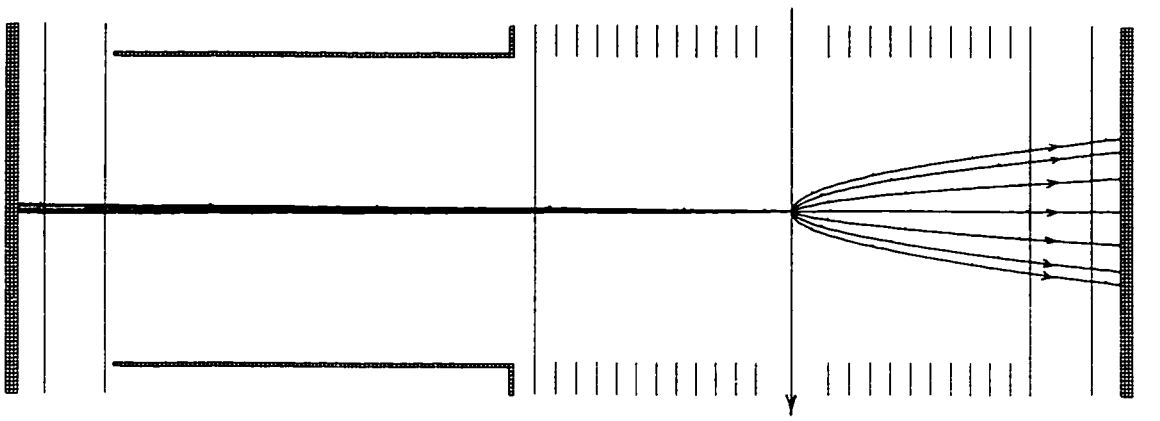

Figure A.1: Simulation of the time-of-flight-position spectrometer of the first-generation experiments (chapter 3). For illustration 7 electrons with energy of 30 eV are projected on the electron detector with angles 0 - 30 degree relative to beam direction. Time markers of electrons are at 1 nsec. Similarly 7 recoil ions (He^+) with momentum of 10 a.u. are projected on the recoil detector.

Similarly we the trajectories of 7 recoil ions (He^+) are shown. The recoil ions are extracted in the direction opposite to the direction of the electrons. Momentum of those recoil ions is 10 a.u. The direction of ejection of those recoil ions is varied, like the electrons, between 0 and -180 degrees in steps of 30 degrees. Time markers are indicating every 1 μsecond. We can see clearly how recoil ions tend to have small transverse displacement under the large applied electric field.

The calibration of both detectors using SIMION was carried out in the following way. An electron (or recoil ion) is generated with a known initial energy. Through the view screen of SIMION we decide where it hits on the electron (recoil-ion) detector. This number is converted from SIMION-grid points to distance (in mm) from the known geometry of the system. This leads to the conversion factor to go from position (on the detector) to energy (momentum) in atomic units. Our SIMION calibration was within 10 % deviation from the calibration carried out using first principles and using the transfer ionization channel as explained on page 50.

Appendix B

Simulation of the Time-of-Flight-Position Spectrometer; Second Generation

The same software (SIMION) was used to simulate and calibrate the spectrometer used in the second-generation experiments (chapter 4). In this spectrometer the applied electric field was not completely uniform. In the recoil ions side of the spectrometer, a lens-like distribution of the electric field was used to position-focus the recoil ions on the recoil-ion detector. This was necessary to minimize the error due to the finite width of the gas jet at the point of intersection with the projectile-ion beam. This technique of position focusing of recoil ions was very well explained and illustrated by M. V. Frohne [129] in her Ph.D. dissertation. This lens-like distribution can be seen in Fig. B.1. In this simulation we use the voltage distribution described on page 81. Electrons experience a very uniform electric field which accelerates them toward the electron detector. On the other hand, recoil ions are

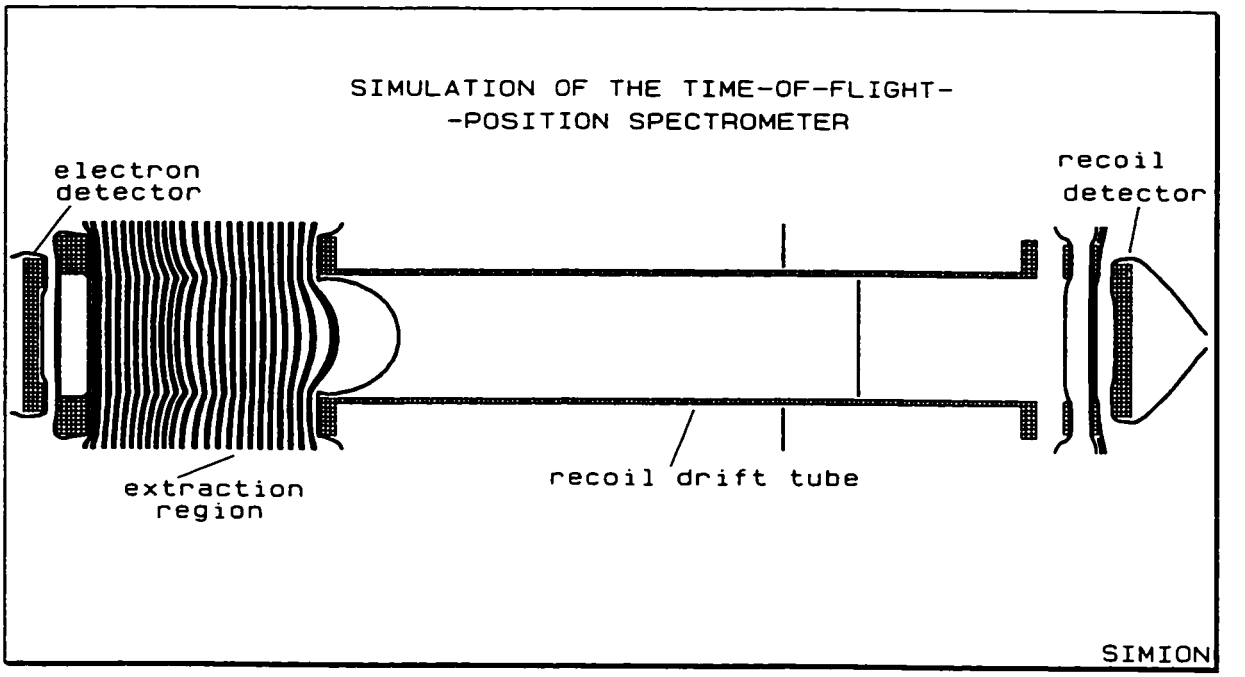

Figure B.1: Simulation of the time-of-flight-position spectrometer of second-generation experiments (chapter 4). The lens setting can be seen through the equi-potential curves. The applied voltages are the same as those described on page 81.

accelerated and focused by the nonuniform field then they travel in the field-free drift region to be finally detected by the recoil detector. The appropriate setting for the electric field needed to get the best focusing of recoil ions on the recoil detector was achieved by trial and error.

An illustration of the simulation of the trajectrories of recoil ions and electrons is given respectively in Fig. B.2. and in Fig. B.3. Through such figures we could calibrate both the recoil-ion detector and the electron detector and calculate the time of flight of both species. For electrons the result was used to convert the electron position on the detector to momentum. For the recoil ions, the result was compared to the calibration carried out through the Q-value distribution in the capture channel. The two calibrations were within 10 % error. The result achieved experimentally from the single capture channel was used.

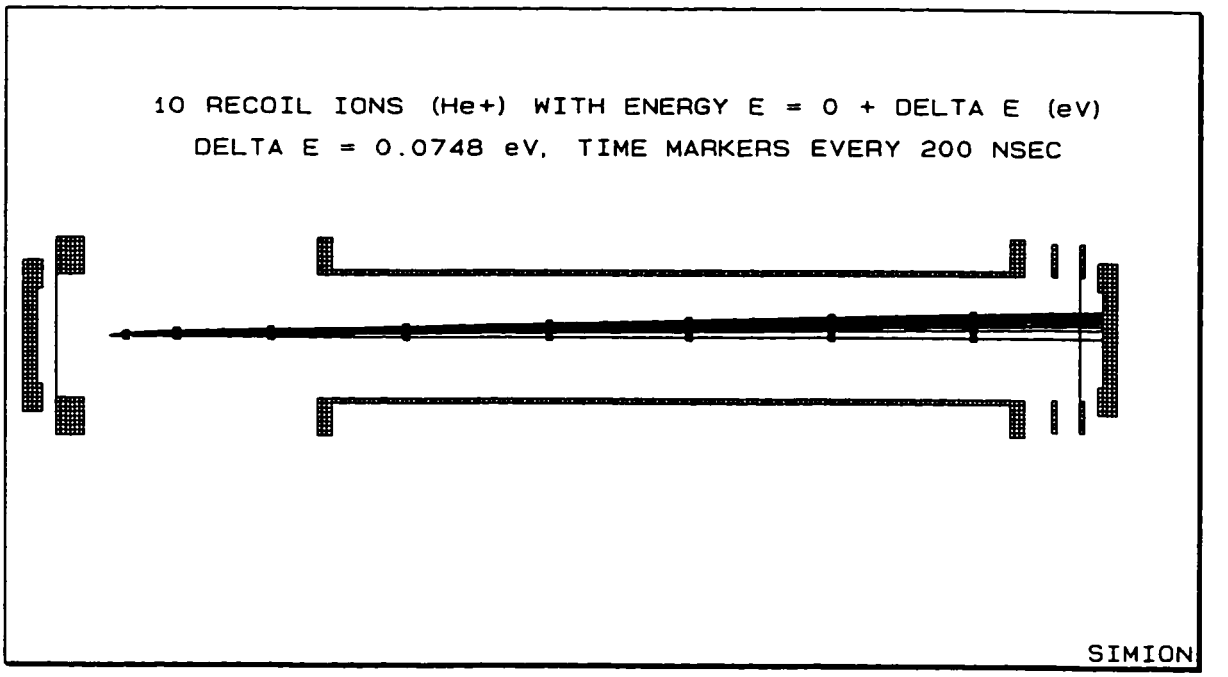

Figure B.2: Simulation of the trajectories of some of the recoil ions in the second-generation time-of-flight-position spectrometer.

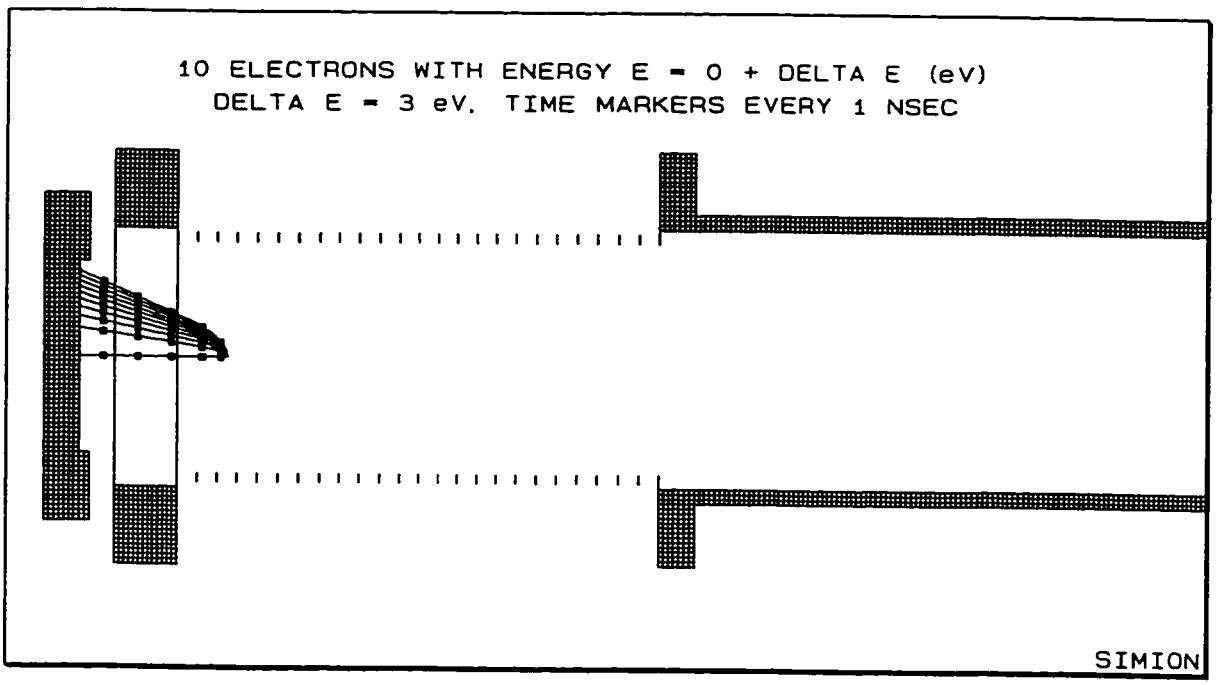

Figure B.3: Simulation of the trajectories of some of the electrons in the second-generation time-of-flight-position spectrometer.

Appendix C

Atomic Beam Sources

Slow atomic and molecular beams were used since the beginning of the century in studying atomic processes in the low velocity regime. The general principle for atomic sources is the effusive (molecular) flow or the aerodynamical flow of the atoms (molecules) from a gas container to a differentialy pumped region. The flowing gas is collimated in one or more stages to form a molecualr beam that intersects with another molecular or ionic beam in the collision chamber. In the following we will explain briefly the general charactaristics of each of the two flow modes with emphasis on the supersonic expansion for it is the method applied in our experiments. More details about this subject can be found, for example, in *Atom and Ion Sources* by L. Vályi [141] and in *Atomic and Molecular Beam Methods* edited by G. Scoles [142]. A discussion of this subject is given also by J. B. Hasted [143].

C.1 Effusive Atomic Beam

In a limiting case the atoms (molecules) will leave the gas container through a slit or an aperture to the surounding space without any change in their spatial or velocity

distribution. Such flow is called effusive (molecular) flow. Consider a gas container with an aperture of diameter d and thickness l. In all of the discussion to follow we will assume a circular aperture (nozzle). In the case where the thickness of the aperture $l \sim 0$, the gas flow is effusive if

$$d \ll \lambda \quad , \tag{C.1}$$

where λ is the mean free path of atoms in the source (container). λ can be calculated using the kinetic theory for an ideal gas. It is given by the formula

$$\lambda = \frac{kT}{\sqrt{2}\sigma_k P} \quad , \tag{C.2}$$

where P and T are the gas pressure and temperature in the source, respectively. k is the Boltzmann constant. σ_k is the collision cross section of the atoms. In a solid sphere model this cross section is given by $\sigma_k = \pi(\frac{\delta}{2})^2$, where δ is the atomic diameter.

The number of atoms flowing within a solid angle $d\Omega$ in the direction defined by the angle θ is given by

$$dN = \frac{d\Omega}{4\pi} n\bar{v} A_s \cos\theta \quad , \tag{C.3}$$

where n is the number of atoms per unit volume in the source, A_s is the aperture area ($A_s = \pi(\frac{d}{2})^2$), and $\bar{v}$ is the mean particle velocity. The latter can be shown to be

$$\bar{v} = \sqrt{\frac{8kT}{\pi m}} \quad , \tag{C.4}$$

where m is the particle mass. To find the total number of particles effusing in all directions, one can integrate Eq. (C.3) over all angles, the result is

$$N = \frac{1}{4} n \bar{v} A_s \quad . \tag{C.5}$$

As can be seen in Eq. (C.3), the particles have a cosine distribution with the flow, basically, is in all directions. More directional beams can be obtained by putting some thickness to the aperture. The directionality of the effusive beam increases by increasing the factor l/d. In the case where $l \gg d$, it has been shown that Eq. (C.5) can be modified by introducing a reduction factor ξ. It becomes

$$N = \frac{1}{4} \xi n \bar{v} A_s \quad . \tag{C.6}$$

The reduction factor ξ in this case is given by

$$\xi = \frac{4d}{3l} \quad . \tag{C.7}$$

Using this, Eq. (C.6) reduces to

$$N = \frac{\pi d^3}{12l} n \bar{v} \quad . \tag{C.8}$$

To achieve larger target densities and therefore larger atomic beam current, the single aperture (capillary) is usually replaced by an array of such aperture. Every capillary collimates the particles that pass through it. Yet a larger number of particles is allowed to escape from the source. Such capillary system is usually made of glass. The diameter of the capillary can be in the range $d = 30$ μm to 1 mm while $l = 300$ μm to 10 mm. In this case the number of particles effusing is given by

$$N = N_{ch} \frac{\pi d^3}{12l} n \bar{v} \quad , \tag{C.9}$$

where N_{ch} is the total number of capillaries in the surface.

C.2 Supersonic Atomic Beam

This method of producing atomic beams was first proposed by Kantrowitz and Grey [144]. In this case a dense gas is allowed to expand through a very narrow nozzle. The condition in this limit is that

$$d \gg \lambda \quad , \tag{C.10}$$

This results in many inter-atomic and atom-wall collisions before the particles escape the nozzle. These conditions result in thermal cooling of the particles in which the random motion is converted into directional energy in the direction of flow. The jet envelope is elliptical in shape with the long axis in the direction of flow of the gas. This shape is due to the superposition of the directional velocity of the jet and the random effusive velocity. After a distance l_s the particles pass through a *skimmer*. The skimmer permits only the inner core particles to pass. The skimmer role is to (a) add more directionality to the atom beam, (b) throw away the slower part of the jet envelope, and (c) reduce the number of scattered particles in the collision chamber. Usually, the skimmer has a conical shape which contributes in reducing the effect of scattered particle on the gas-jet flow through the orifice.

An important parameter in describing the supersonic gas flow is the Mach number M. The Mach number is defined as the ratio of the the local flow velocity to the the local speed of sound.

$$M = \frac{v}{c} \quad . \tag{C.11}$$

The speed of sound is given by

$$c = \sqrt{\frac{\gamma P}{\rho}} \quad , \tag{C.12}$$

P and ρ are the local pressure and density . γ is the heat capacity ratio; $\gamma = C_P/C_V$ ($\gamma = \frac{5}{3}$ for mono-atomic gas and $\gamma = \frac{7}{5}$ for diatomic gas). For an ideal gas ($P = nkT$), The last equation be rewritten as

$$c = \sqrt{\frac{\gamma kT}{m}} \quad , \tag{C.13}$$

where T is the temperature and m is the atomic mass.

The atom's directional velocity is related to the sound speed in the source (c_o) through the formula

$$v_{jet} = uM = c_o \frac{M}{[1 + \frac{\gamma-1}{2}M^2]^{(\frac{1}{2})}} = \frac{M}{[1 + \frac{\gamma-1}{2}M^2]^{(\frac{1}{2})}} \sqrt{\frac{\gamma kT_o}{m}} \quad , \tag{C.14}$$

where T_o is the temperature in the source. In the nozzle, the Mach number $M = 1$ and therefore Eq. (C.14) reduces to

$$v_{jet(nozzle)} = u = \sqrt{\frac{2}{\gamma+1}} \sqrt{\frac{\gamma kT_o}{m}} \quad . \tag{C.15}$$

On the other hand, to find the downstream velocity of the jet, one can assume $M \gg 1$ and therefore Eq. (C.14) gives

$$v_{jet(downstream)} \simeq \sqrt{\frac{2}{\gamma-1}} \sqrt{\frac{\gamma kT_o}{m}} \quad . \tag{C.16}$$

For mono-atomic gas $\gamma = \frac{5}{3}$ and therefore Eq. (C.16) reduces to

$$v_{jet(downstream/monoatomic)} \simeq \sqrt{\frac{5kT_o}{m}} \quad . \tag{C.17}$$

One can calculate the atomic density (n_s) and atomic velocity (v_s) at the skimmer orifice. The results are

$$n_s = n_o[1 + \frac{\gamma - 1}{2} M_s^2]^{(-\frac{1}{\gamma-1})} \quad , \tag{C.18}$$

and

$$v_s = uM_s = c_o \frac{M_s}{[1 + \frac{\gamma-1}{2} M_s^2]^{(\frac{1}{2})}} \quad , \tag{C.19}$$

where n_o and c_o are the atomic density and sound velocity in the source (nozzle chamber). M_s is the Mach number at the orifice of the skimmer u is the velocity of the atoms flying out from the nozzle. Accordingly the beam current passing the skimmer can be evaluated as

$$j = n_s v_s A_s = n_o c_o A_s \frac{M_s}{[1 + \frac{\gamma-1}{2} M_s^2]^{(\frac{1}{2}+\frac{1}{\gamma-1})}} \quad , \tag{C.20}$$

where A_s is the area of the skimmer orifice. The Mach number can be estimated as

$$M_s \approx b\sqrt{\frac{l_s}{d}} \quad , \tag{C.21}$$

where b is a constant that can be determined experimentally ($b = 2.75$).

Appendix D

Gas Jet Operation

D.1 Jet-Skimmer Parameters

We can utilize the formulas presented in the previous appendix to estimate few important parameters for the supersonic gas jet system employed in our experimental setup. Among the important parameters are the jet velocity and density at the point of intersection with the projectile ion beam. Since most of the experiments used He as a target, we will limit our calculations to He.

In Fig. D.1(a). we show the exact dimensions of the jet-skimmer system. The diameter (d_s) of the jet at the point of intersection with the ion beam is determined geometrically to be 3.5 mm. This agrees very well with the width determined experimentally. The skimmer is conical in shape with an angle of 45°. The distance from the 30-μm nozzle to the orifice of the skimmer is l_s = 9 mm. The height of the skimmer is 6.4 mm. The distance from the base of the skimmer to the point of intersection with the beam is 50.8 mm. Those dimensions were kept constant for all experiments.

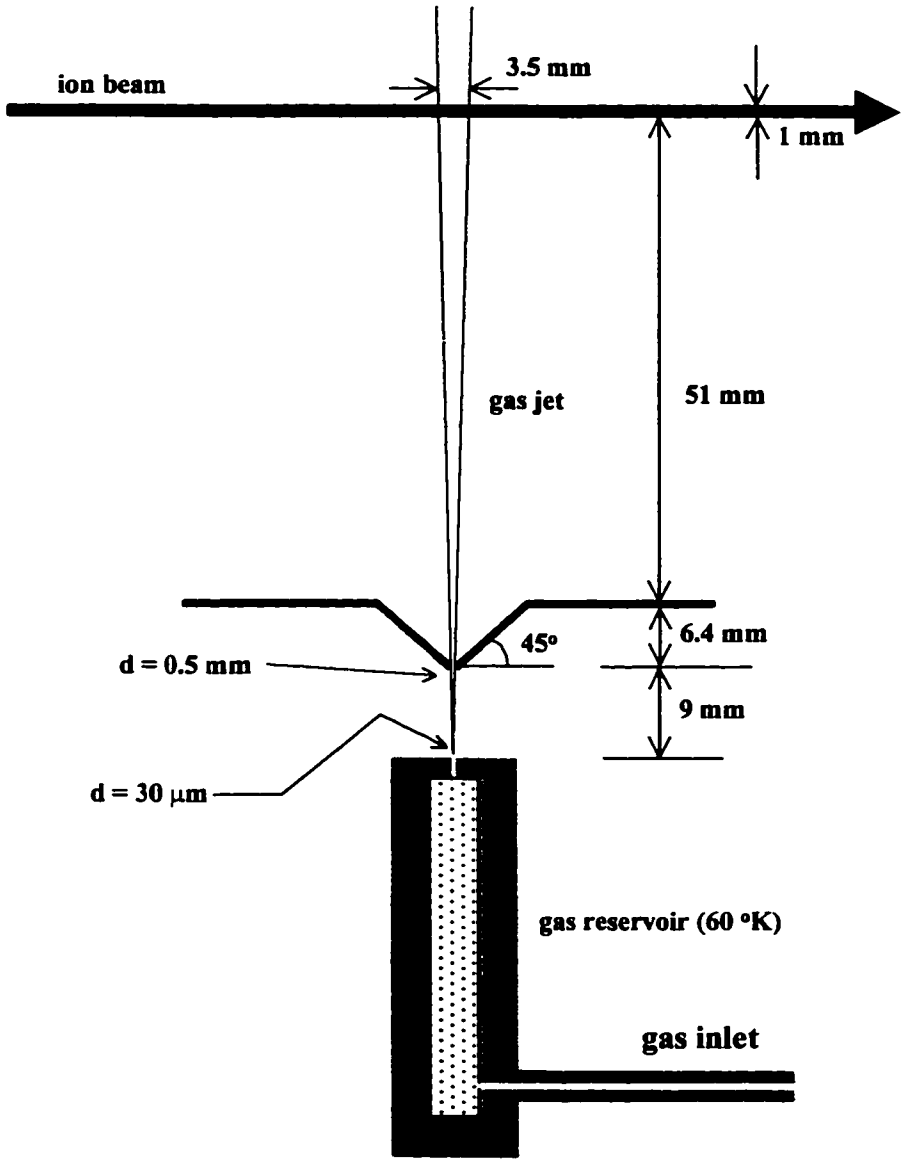

Figure D.1: Jet-skimmer system employed in the experiment. Distances in mm.

The gas inlet (reservoir) pressure P_o was usually about 0.1 atm. In MKS units this pressure translates to $P_o \approx 10^4$ Pascal. The reservoir and therefore the contained gas was kept at a temperature $T_o \approx 60$ K. This temperature was the lowest temperature achievable by the cryogenerator used in the cooling process.

At room temperature ($T_o \approx 300$ K) the jet velocity, according to Eq. (C.17), is $v_{jet} \approx 1759$ m/s. This corresponds to momentum $p_{jet} \approx 5.9$ a.u. Note that the jet velocity depends on the square root of the source temperature ($v_{jet} \sim \sqrt{T_o}$). Therefore, at the operational temperature $T_o = 60$ K, the jet velocity is reduced by a factor of 2.23. The jet momentum then is $p_{jet} \approx 2.6$ a.u. These momenta were confirmed experimentally. The jet momentum reduction, in fact, can be used as a measure of the reservoir temperature.

Eq. (C.20) can be applied directly to estimate the jet current after passing through the skimmer. The Mach number at the skimmer can be estimated using Eq. (C.21). The result is $M_s \approx 48$. The atomic density in the source (n_o) depends on the gas mass density (ρ_o) in the following way

$$n_o = \frac{W}{\rho_o N_o} \quad , \tag{D.1}$$

where $N_o = 6.023 \times 10^{23}$ is Avogadro's number and W is the mass of 1 mole of gas (in kg). Assuming ideal gas conditions in the reservoir, one can use Eq. (C.18) and Eq. (D.1) to show that

$$n_o = \frac{P_o N_o m}{k T_o W} \quad . \tag{D.2}$$

Thus for Helium gas in the reservoir at $P_o \approx 10^4$ Pascal and $T_o \approx 300$ K, ($m = 6.7 \times 10^{-27}$ kg and $W = 4 \times 10^{-3}$ kg), we find that $n_o \approx 2.5 \times 10^{24}$ atom/m^3. Plugging these numbers in Eq. (C.20) we find that the jet current after passing the

skimmer is $j \approx 4 \times 10^{16}$ atoms/second. Using the jet velocity and the jet diameter at the point of intersection with the beam, we find that the atomic density n_b is 2.4×10^{12} atoms/cm^3.

Note that the jet current scales with the reciprocal of the square root of the reservoir temperature ($j \sim \sqrt{T_o}$). Therefore, the jet current at the operational temperature $T_o \approx 60$ K is $j \approx 9.1 \times 10^{16}$ atoms/second and the atomic density of the jet at the intersection with the projectile ion beam is $n_b \approx 1.2 \times 10^{13}$ atoms/cm^3. It is obvious that, for a given P_o, the target density depends on the reciprocal of the temperature ($n_b \sim 1/T_o$). Thus, reducing the gas temperature from 300 K to 60 K results in a target which is 5 times more dense for the same P_o. The largest possible error in the previous estimation of target density arises from the uncertainty in the driving pressure P_o in the gas reservoir. The gas pressure was measured in the tube that supplies gas to the reservoir. However, a needle valve was used to regulate the gas entrance to the reservoir (appendix D.3). This could contribute to a certain inaccuracy in the value of P_o.

D.2 System Differential Pumping

The experimental system was differentially pumped. The differential pumping divided the setup into five regions. An illustration of this differential pumping of the experimental setup is given in Fig. D.2. The five regions are: The main collision chamber (II). Collisions take place in this region. This region is pumped by a turbopump. In addition a liquid Nitrogen cold trap is sometimes used to lower the pressure in this area. The skimmer area (III) where the the excess gas flowing from the 30-μm nozzle is skimmed to leave the coolest part of the jet to pass through the 0.5 mm hole of the conical skimmer. The jet-dump region (catcher) (IV) which

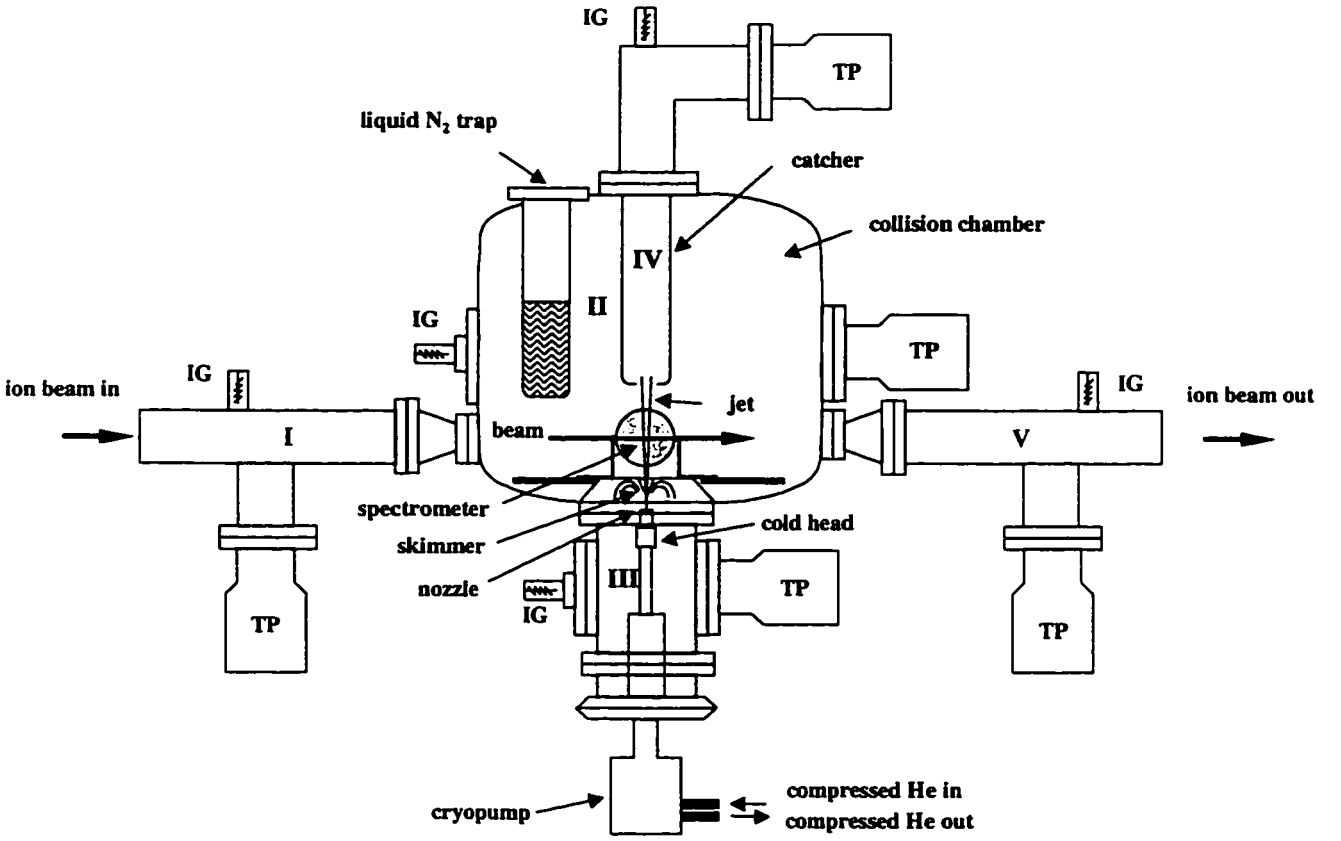

Figure D.2: Schematic diagram of the experimental setup. The five differentially pumped regions are marked by the Roman letters I-V. TP: turbopump, IG: ion gauge. The elements shown in this diagram are not to scale.

catches most of the gas jet to be dumped to a turbopump. This minimizes the fraction of the jet gas scattered in the collision area. Finally the beam-lines outside the collision chambers both upstream (I) and downstream (V). The main chamber (II) is separated from the the upstream tube (I) and the downstream tube (V) by two 2-cm apertures (not shown in the figure). The skimmer 0.5-mm hole is the only opening between the skimmer region (III) and the collision chamber (II). The catcher has an aperture of 2.5-cm diameter. This aperture is wide enough to catch the whole jet but also it minimizes the amount of gas flowing back into the collision chamber. The pressure in the five differentially pumped regions is measured simultaneously. In table D.1 we give typical values of the pressure in different regions during the operation of the gas jet. In the first column we record the driving pressure which is the gas pressure in the reservoir behind the 30-μm nozzle. These pressure readings are for He at room temperature. The pressure change in different regions of the system gives an indication of the quality of jet flow and skimming. The best situation would be achieved if all the jet is dumped to the catcher resulting in no pressure rise in the collision area. Technically this is not possible. However, we could minimize the pressure rise in the collision area by appropriately aligning the nozzle-skimmer-catcher system. The quality of the jet can be described by the ratio of the pressure rise in the catcher ($\Delta P_{catcher}$)to the pressure rise in the chamber ($\Delta P_{chamber}$). This can be written as:

$$R = \Delta P_{catcher}/\Delta P_{chamber} \quad , \tag{D.3}$$

We tried to keep the number R as high as possible during the experiment. In Fig. D.3(a). we show the typical behavior of the catcher pressure and the chamber pressure plotted versus the pressure in the skimmer area. It is noted that the

driving P	$P_{skimmer}$ *(torr)*	$P_{downstream}$ *(10^{-7} torr)*	$P_{chamber}$ *(10^{-8} torr)*	$P_{catcher}$ *(10^{-8} torr)*
----------	2.7×10^{-7}	3.8	4.4	7.6
24 in Hg vac	1.3×10^{-5}	3.8	5.4	10
23 in Hg vac	1.7×10^{-5}	3.8	6.0	12
21 in Hg vac	2.9×10^{-5}	4.0	7.4	15
19 in Hg vac	3.4×10^{-5}	4.0	8.5	17
17 in Hg vac	4.4×10^{-5}	4.0	9.9	20
15 in Hg vac	5.6×10^{-5}	4.1	11	22
13 in Hg vac	6.8×10^{-5}	4.1	13	25
11 in Hg vac	8.0×10^{-5}	4.2	14	27
9 in Hg vac	9.5×10^{-5}	4.3	16	30
7 in Hg vac	1.1×10^{-4}	4.3	17	32
5 in Hg vac	1.2×10^{-4}	4.4	19	34
3 in Hg vac	1.4×10^{-4}	4.5	21	36
1 atm	1.6×10^{-4}	4.6	23	39
1.5 psi	1.9×10^{-4}	4.7	26	43
3.0 psi	2.2×10^{-4}	4.8	29	45
5.0 psi	2.6×10^{-4}	5.0	33	50
7.0 psi	3.1×10^{-4}	5.2	37	54

Table D.1: Table of the pressure in the five differentially pumped regions depending on the driving pressure in the gas inlet.

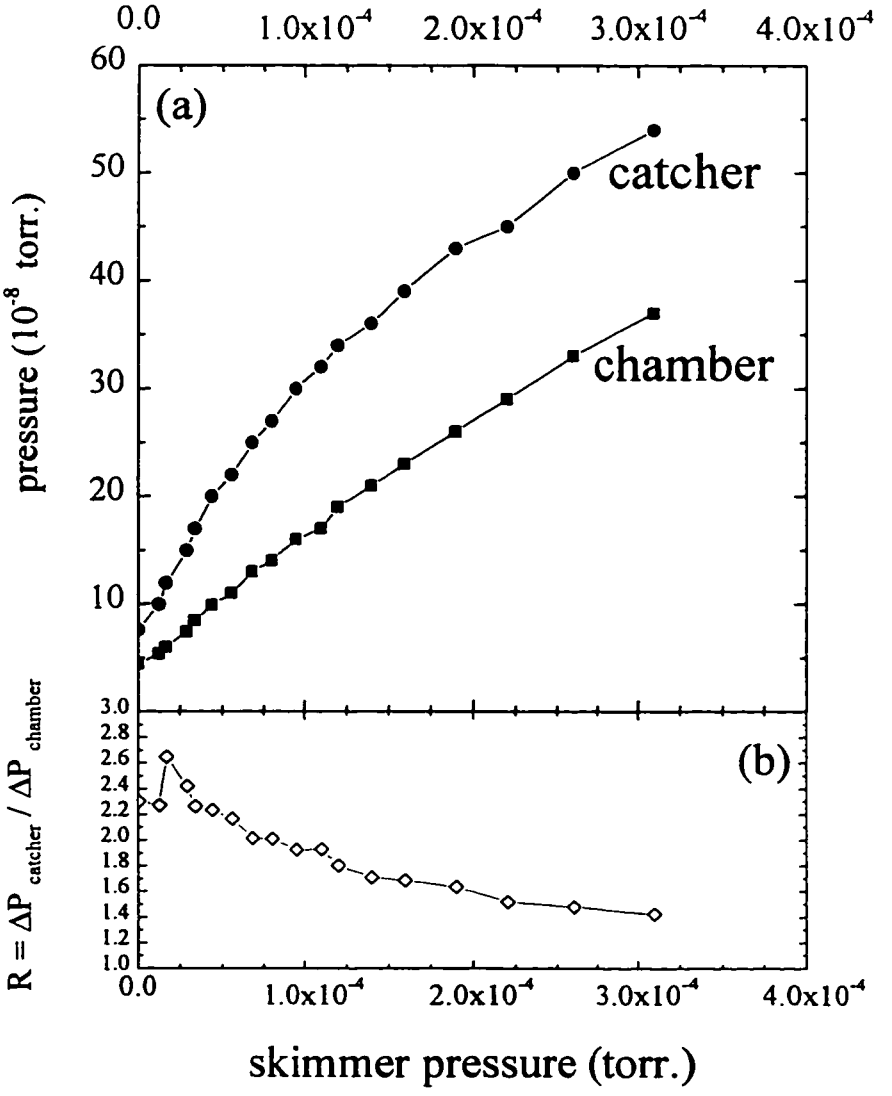

Figure D.3: (a) Pressure in the catcher and the chamber regions plotted versus the pressure in the skimmer area. (b) the ratio of the pressure rise in the catcher to the pressure rise in the chamber plotted versus the pressure in the skimmer area.

pressure increase in the two regions tends to "saturate" at higher driving pressures. This behavior is understood as the excess gas interferes with the gas jet at higher pressures which results in a partial destruction of the gas jet. The rise in the catcher pressure is larger than the rise in the chamber pressure which is a positive sign. In Fig. D.3(b), we note that the ratio R decreases by increasing the driving pressure. This is mainly due, again, to the interference of the scattered gas and the jet at the skimmer pinhole. We operated the jet at a skimmer pressure of about 1.0×10^{-4} torr. where the ratio R is about 2 and still we had reasonable target density. The ratio of double collisions to the total number of collisions was negligible at this pressure in the main collision chamber.

D.3 Gas Input Control

The gas flow to the reservoir behind the 30-μm nozzle was controlled by several valves in the fore-line. This was necessary to generate a certain pressure in the reservoir and therefore in the rest of the system. The control system is displayed in a schematic way in Fig. D.4. A rouging pump is used to clean the gas tube before opening the gas bottle. The rate of flow from the gas bottle is controlled by a needle valve. The pressure just outside the bottle can be read by a pressure gauge which is sensitive to pressure values less than one atmosphere. The typical pressure in the gas tube was in the range of 0.1 to 1.0 atmosphere. To have an accurate control over the pressure in the reservoir, another needle valve is used to control the flow just before entering the skimmer chamber. During the operation of the jet, the cryopump cold head and the reservoir had a temperature of 60 °K. To minimize thermal contact to the outside environment and to prevent freezing of the gas tube entering the chamber, the gas capillary tube inside the skimmer chamber

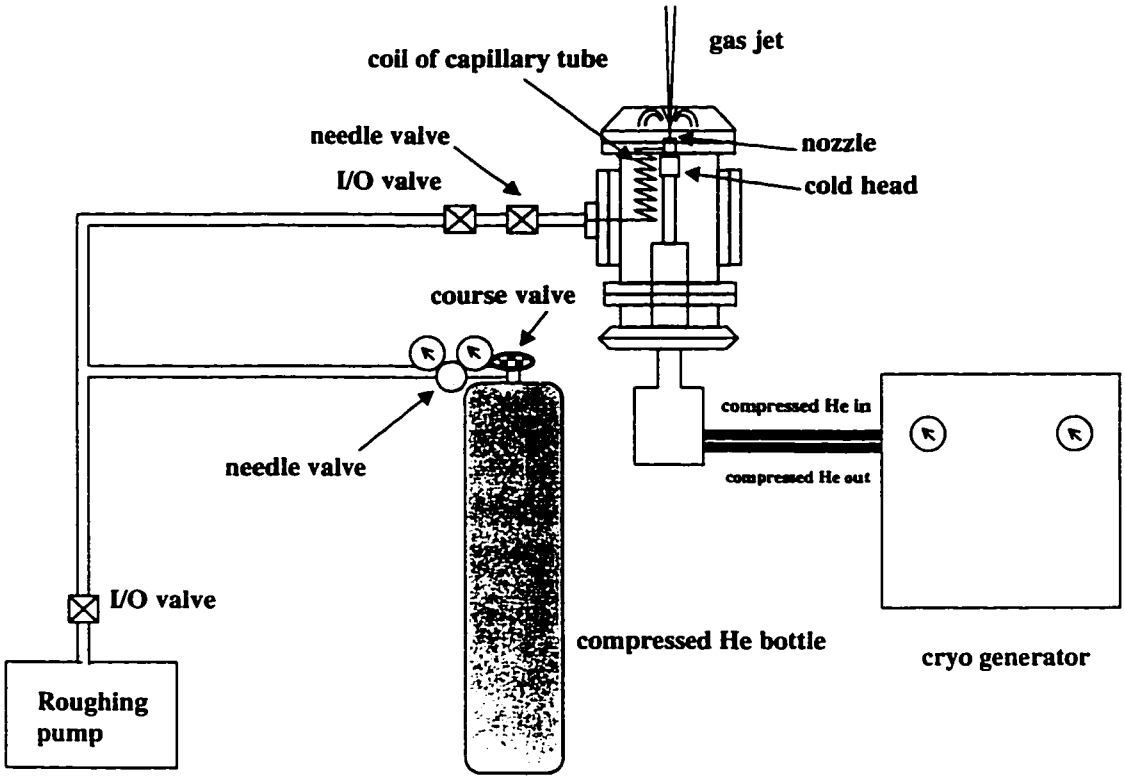

Figure D.4: Schematic sketch of the target-gas flow control system.

was shaped into a coil. This increased its length and therefore reduced thermal exchange. Note that the capillary tube is too narrow.

Appendix E

Signal Extraction from the Detectors

In the first series of experiments presented in chapter 3, we used electron and recoil detectors with two channel plates for each. In the next generation of experiments presented in chapter 4, we used detectors with stacks of three channel plates. The addition of one channel plate improved the gain and therefore improved the ratio of signal to noise. A channel plate is usually operational at a voltage drop of about 700 - 1000 Volts between its two sides. The electrons generated by the channels due to ion (electron) impact on the surface of the first plate are accelerated by a small potential drop (usually about 50 - 100 Volts) to hit the anode. This potential drop is usually termed the *bias voltage* which is the potential difference between the back of the last channel plate and the anode.

In all of the experiments we used a wedge-strip-type anodes in detecting electrons and recoil ions and a resistive anode in the projectile detector. In the following we will limit our discussion to the wedge-strip-type anode. The other type is very

similar. The wedge-strip-type anodes used have two faces. The upper face has a semi-conducting Germanium layer. The other face has the wedges-and-strips pattern of conducting material. The two surfaces are separated by an insulating material which is ceramic. Electrons leaving the back of the last channel plate are accelerated toward the Germanium layer. As they accumulate on the layer, the capacitive coupling to the other face (with the pattern) results in a signal proportional to the signal of the original electrons. It is the signal distribution among the wedges, strips, and the minder that is used to reconstruct the position information. The signals from the three areas (w,s,R or equivilantly x,y,R)) are passed through three capacitors (see Fig. E.1). The absolute voltages applied on the two sides of the channel-plate sandwich and the anode are determined by the voltage distribution on the rest of the system including the extraction electrodes, bias grids and the detector on the other end of the spectrometer. Therefore it is very common to apply high voltage on the anode. To extract the signal with the presence of the high voltage on the anode it was necessary to use the capacitors C1.

The element F was used to protect the CATSA preamplifier . This element is made simply of two electrodes contained in a sealed glass tube with a gas filling the space between the two electrodes. In normal conditions where a reasonable-size signal is passed by the capacitors, the element F is passive since it forms an open circuit to ground. However, in the case of unusually large signal, the gas in the element F discharges and F forms an open circuit to ground. Therefore the large signal is sent to ground rather than the *sensitive* CATSA preamplifier. Such large signals may appear from time to time and it is usually caused by electrical discharge in one of the high-voltage elements in the extraction-detection system. The time signal is extracted from the back of the last channel plate. A capacitor C2 is used

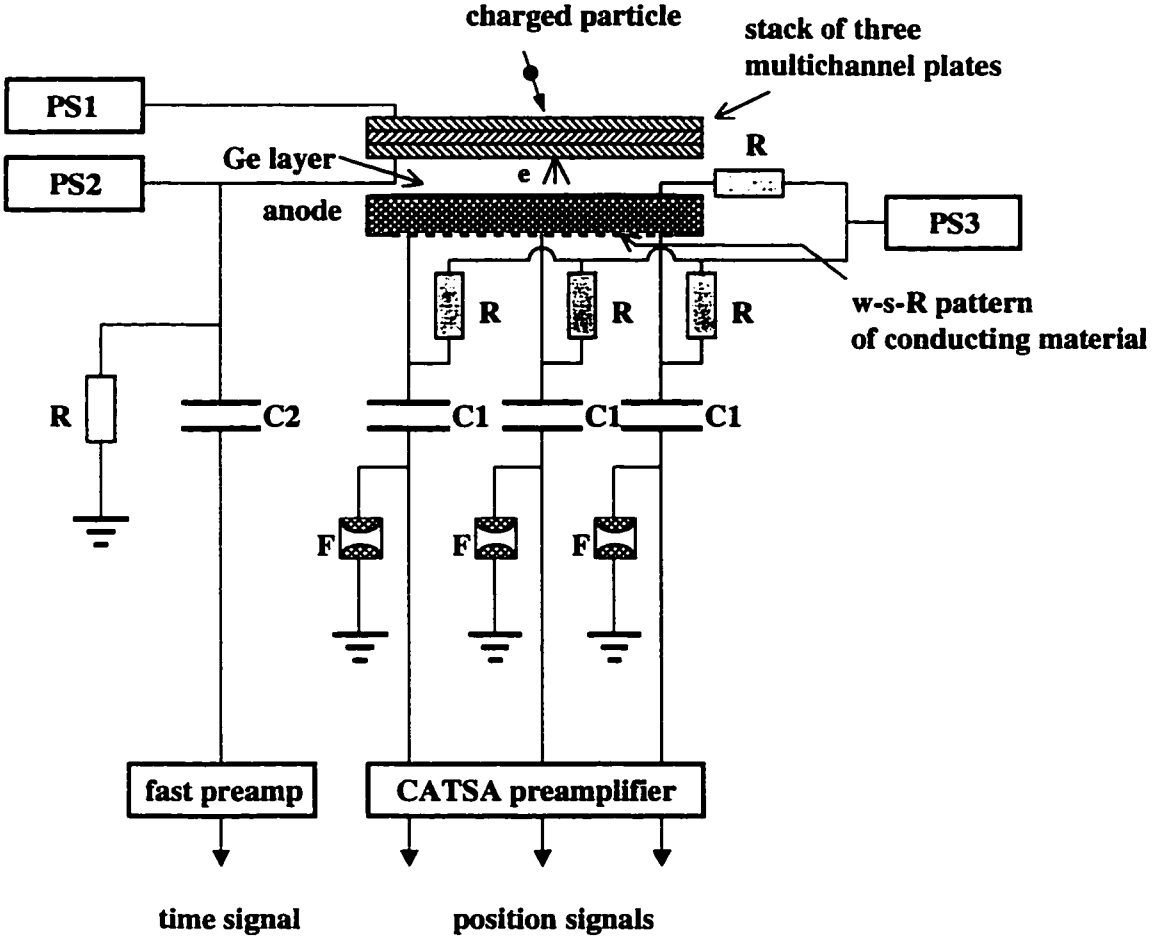

Figure E.1: Time and position signals extraction from a wedge-strip-type position sensitive detector.

to pass the time signal. The signal is then sent to the fast preamplifier.

Appendix F

Other Collision Systems

In addition to the collision systems studied and presented in chapter 4 (He^+ + He for v_p = 0.45 - 1.0 a.u., He^{2+} + He for v_p = 0.45 - 1.0 a.u., and C^{6+} + He for v_p = 1.17 - 1.63 a.u.), we studied several other systems at different velocities. The collision of Ne^+ with Ne was studied in the velocity range v_p = 0.25 - 0.55 a.u., the collision of He^+ with Ne was studied in the range v_p = 0.33 - 0.78, and the collision of Ne^+ with He at a projectile velocity v_p = 0.35 a.u. In addition protons collisions with He were studied at v_p = 0.53 - 0.78 a.u. The results of p + He system are in a very good agreement with the results obtained by Dörner *et al.* [49] using a similar technique.

In this appendix we present some of the results for these mentioned systems without much details. The most interesting feature in the electron spectra presented in this appendix is the absence of the two-branches distribution seen in electron spectra of He^+ + He, He^{2+} + He, and p + He. This indicates that electron promotion to the continuum happens via molecular orbitals different from those in the previously mentioned system. In general one can think of the electron spectrum as a signature

of the molecular orbitals involved in the promotion process.

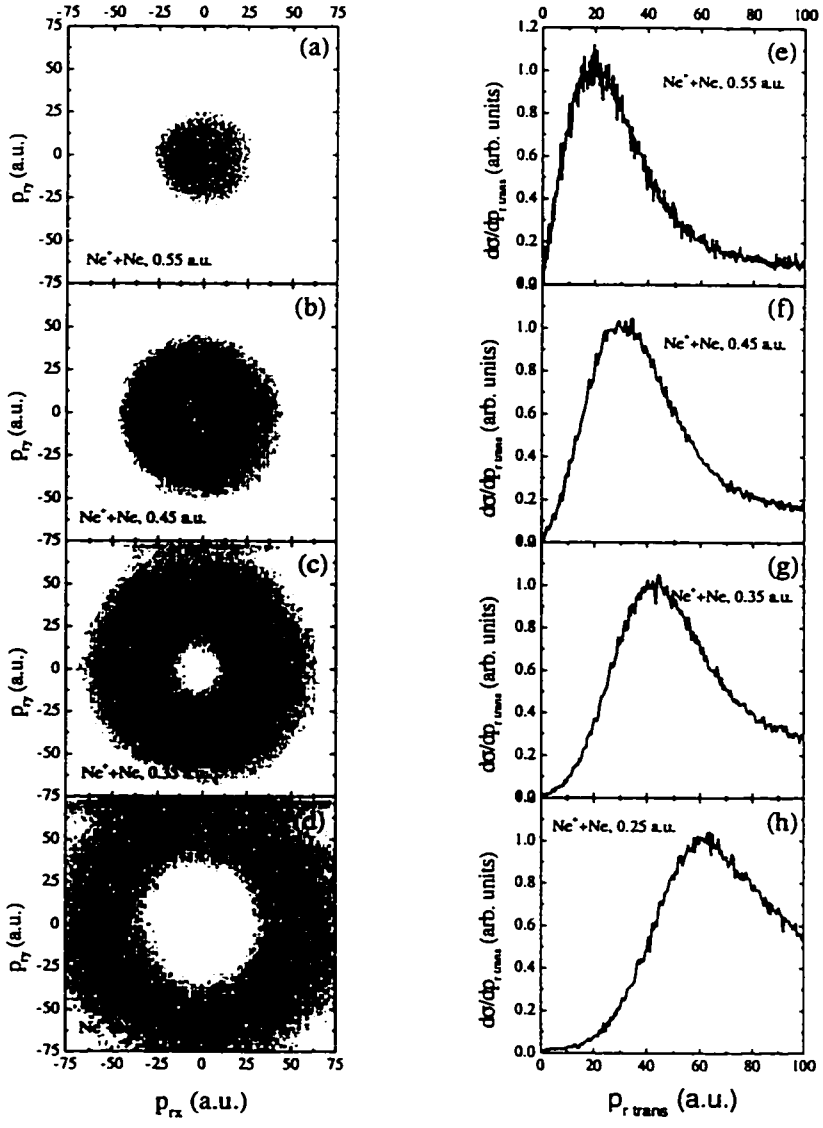

Figure F.1: Recoil-ion transverse momentum distributions in the collision Ne^+ + Ne leading to single ionization at projectile velocities v_p = 0.25 - 0.55 a.u. (a - d) are the two-dimensional distributions. (e - h) are the radial distributions calculated by integrating the distributions (a - d) over full azimuthal angle.

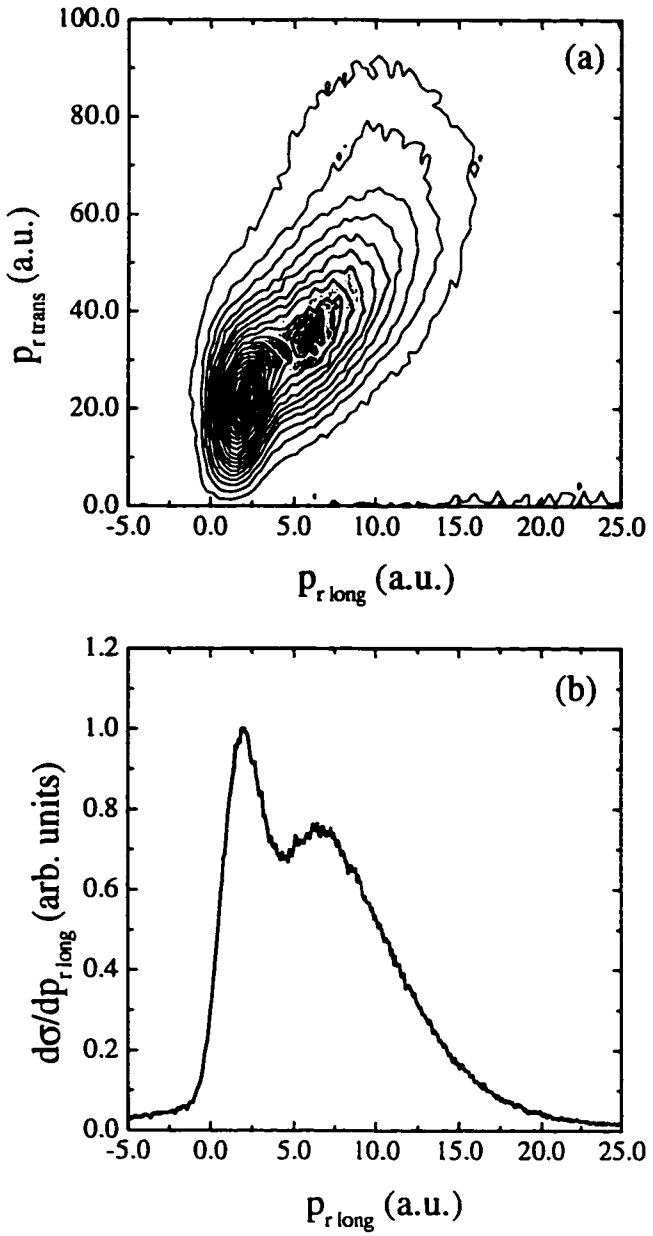

Figure F.2: (a) Recoil-ion transverse momentum versus longitudinal momentum for the collision Ne^+ + Ne at v_p = 0.45 a.u. Note that the scales in the two axes are different for convenience. (b) Longitudinal momentum distribution summed over all transverse momentum.

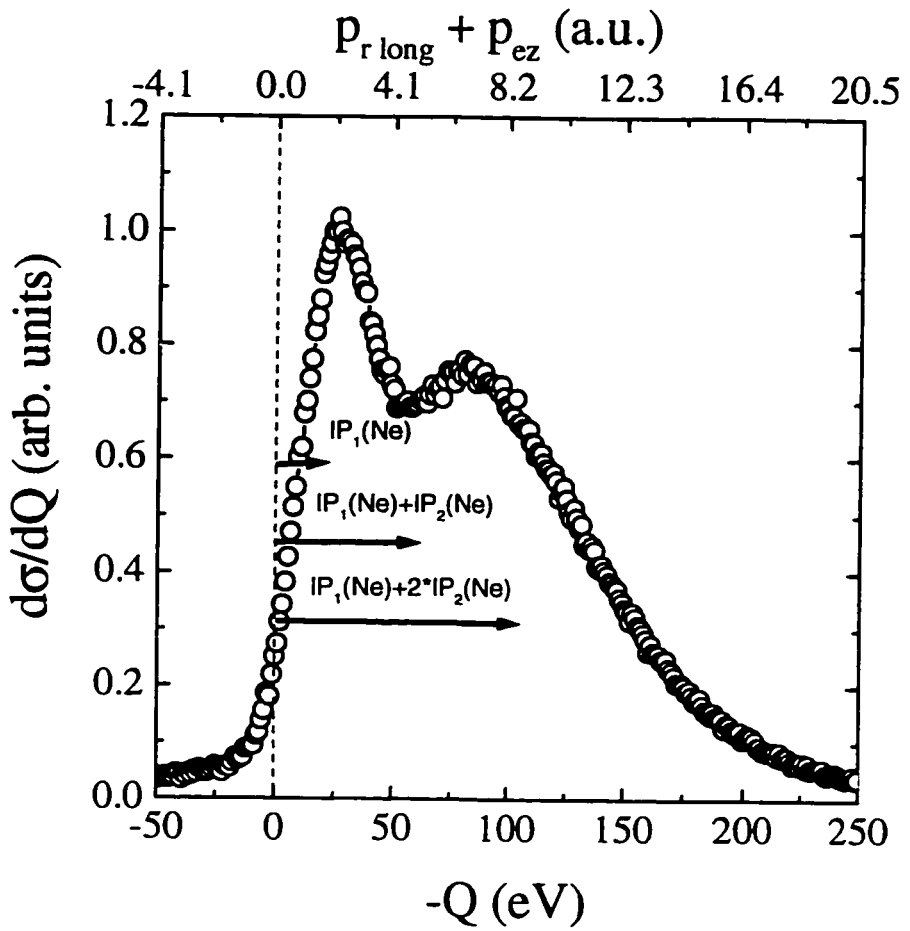

Figure F.3: Q-value distribution for the collision Ne^+ + Ne at $v_p = 0.45$ a.u. $IP_1(Ne)$ and $IP_2(Ne)$ are the first and the second ionization potentials of Ne respectively.

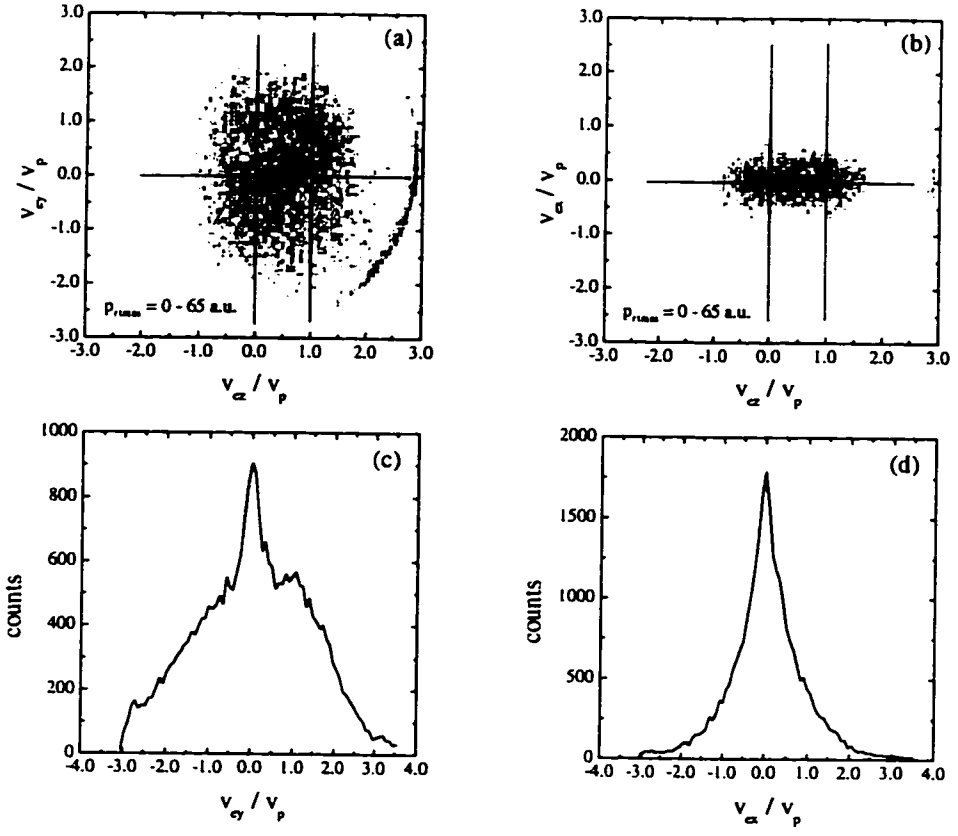

Figure F.4: (a) Top view and (b) side view of the ejected electrons in the collision of Ne^+ + Ne at v_p = 0.45 a.u. (c) and (d) are sideway projections of (a) and (b) respectively.

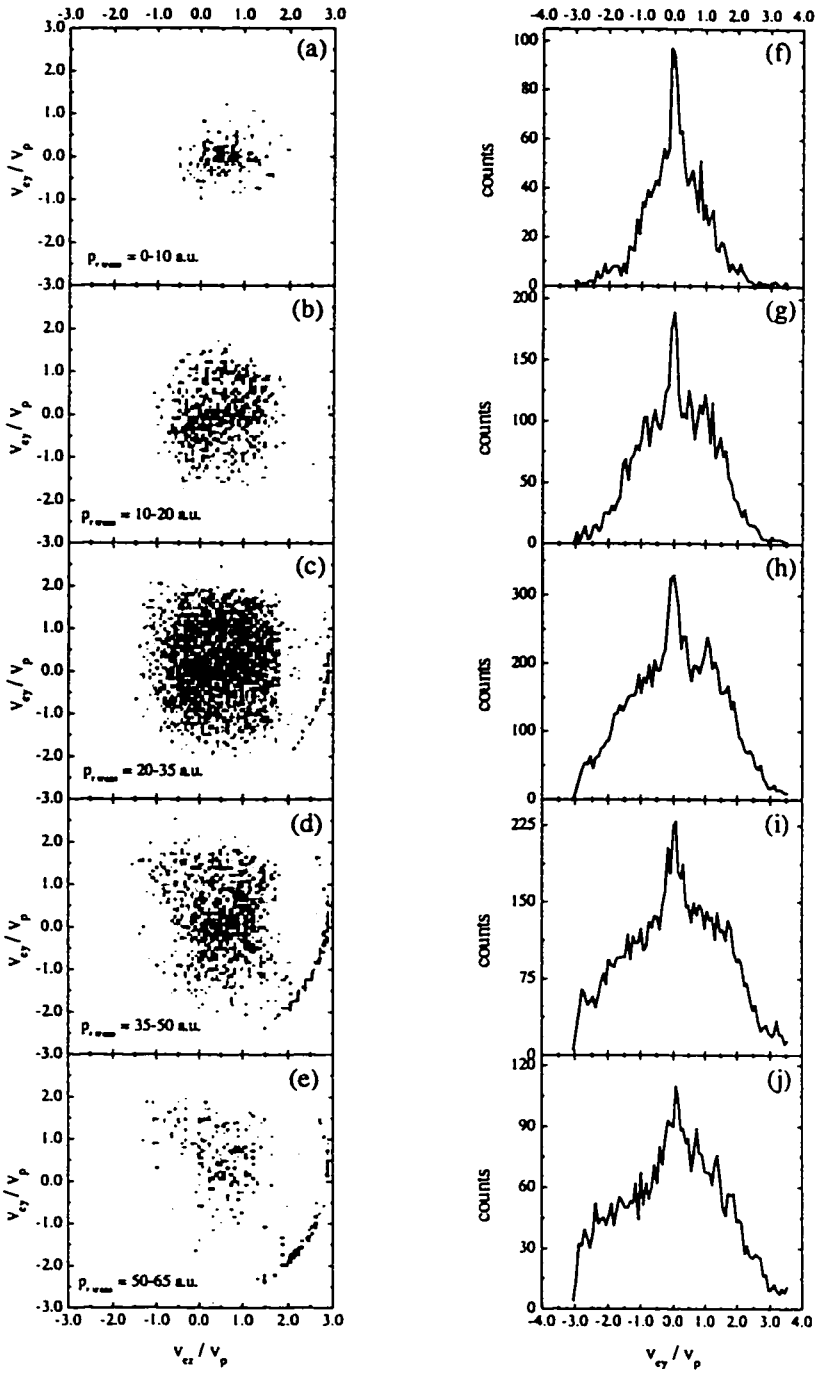

Figure F.5: (a - e) Top view of the ejected electrons in the collision of $Ne^+ + Ne$ at v_p = 0.45 a.u. gated at different ranges of recoil-ion transverse momentum. Sideways projections are given respectively in (f - j).

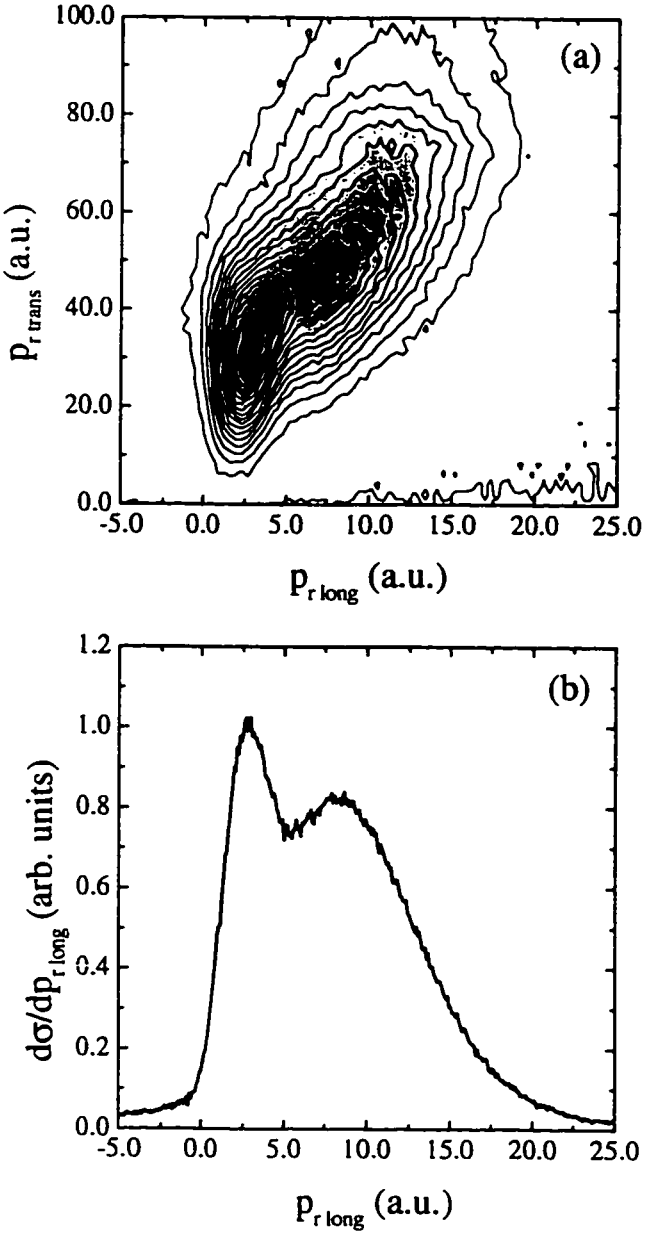

Figure F.6: (a) Recoil-ion transverse momentum versus longitudinal momentum for the collision Ne^+ + Ne at v_p = 0.35 a.u. Note that the scales in the two axes are different for convenience. (b) Longitudinal momentum distribution summed over all transverse momentum.

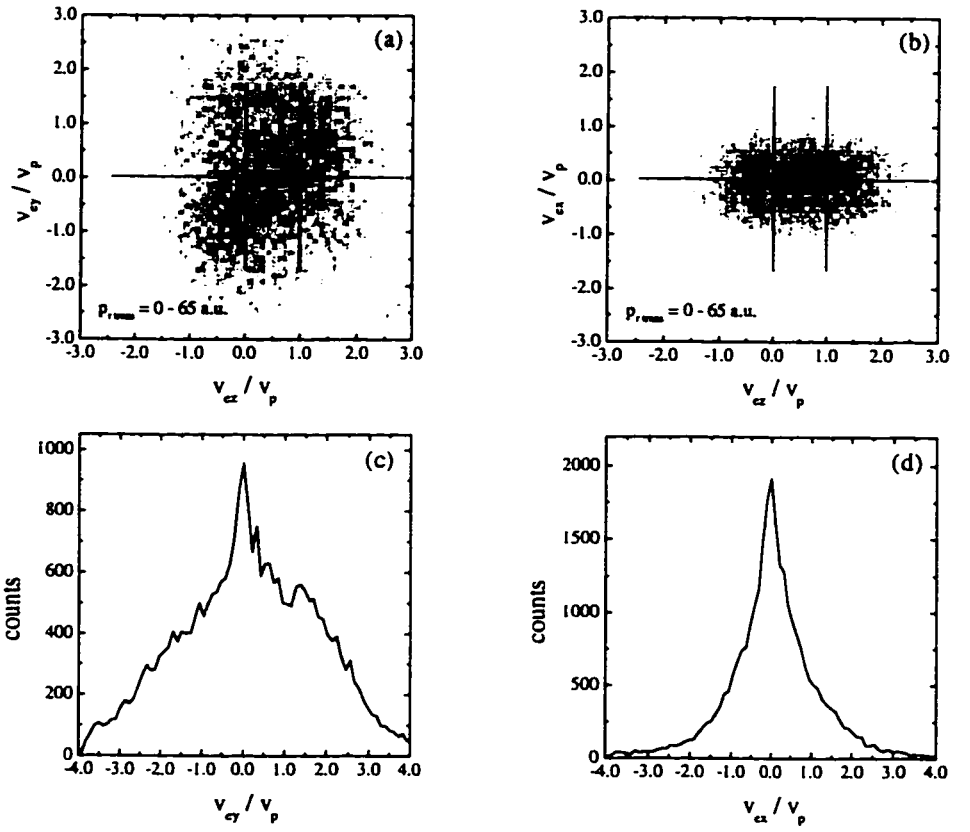

Figure F.7: (a) Top view and (b) side view of the ejected electrons in the collision of Ne^+ + Ne at $v_p = 0.35$ a.u. (c) and (d) are sideway projections of (a) and (b) respectively.

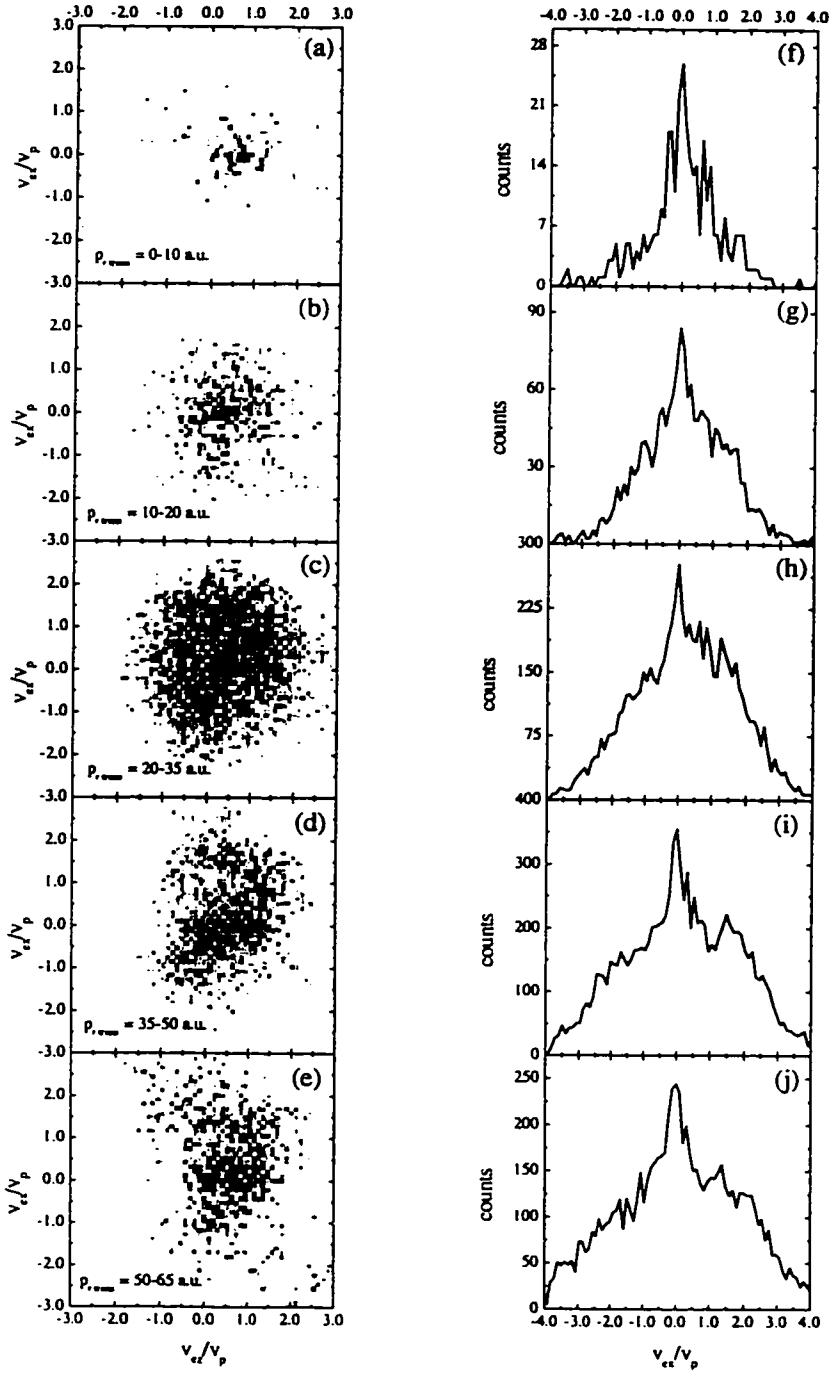

Figure F.8: (a - e) Top view of the ejected electrons in the collision of Ne^+ + Ne at v_p = 0.35 a.u. gated at different ranges of recoil-ion transverse momentum. Sideways projections are given respectively in (f - j).

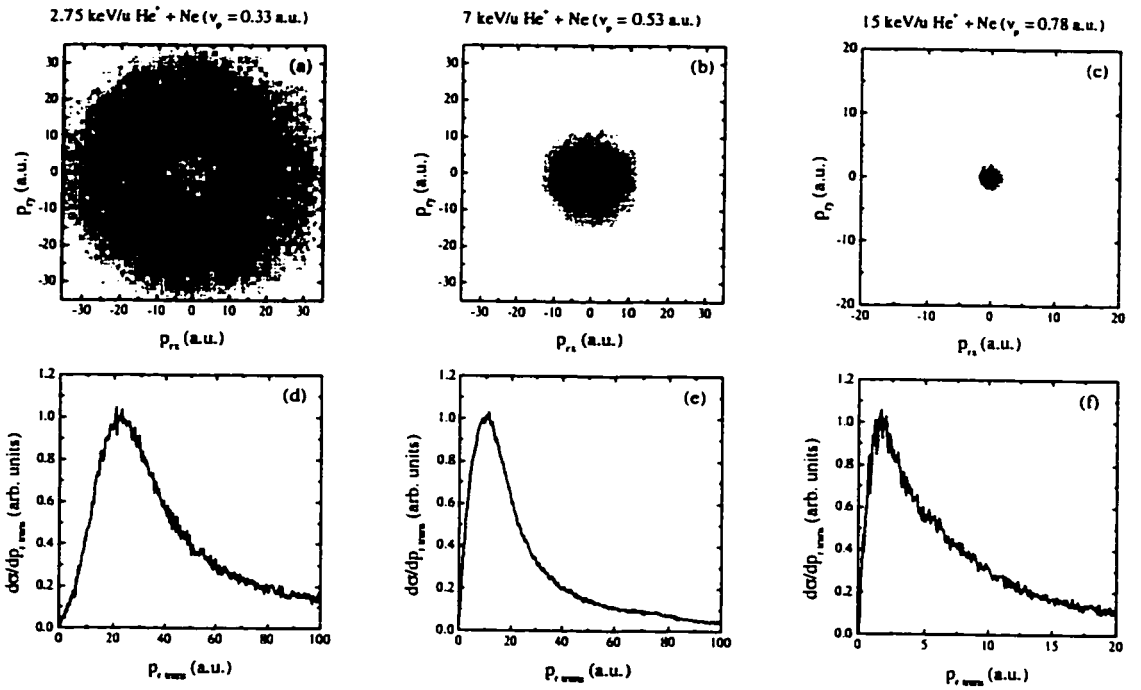

Figure F.9: Recoil-ion transverse momentum distributions in the collision He^+ + Ne leading to single ionization at projectile velocities v_p = 0.33 - 0.78 a.u. (a - c) are the two-dimensional distributions. (d - f) are the radial distributions calculated by integrating the distributions (a - c) over full azimuthal angle.

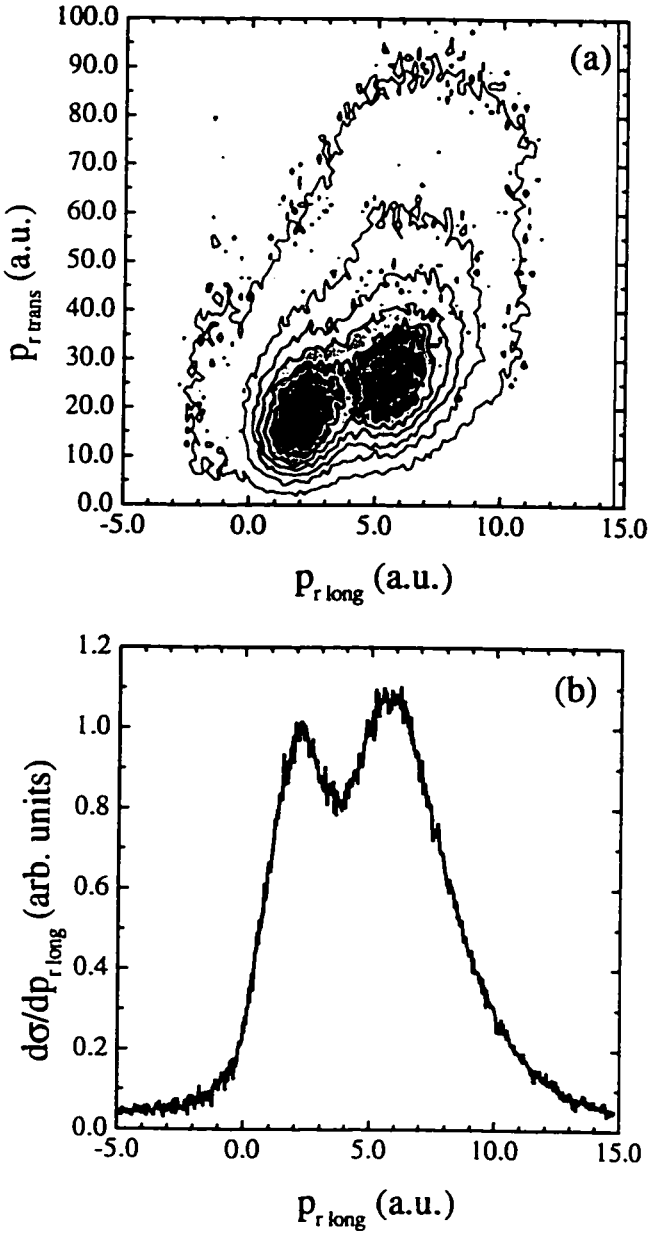

Figure F.10: (a) Recoil-ion transverse momentum versus longitudinal momentum for the collision $He^+ + Ne$ at $v_p = 0.33$ a.u. Note that the scales in the two axes are different for convenience. (b) Longitudinal momentum distribution summed over all transverse momentum.

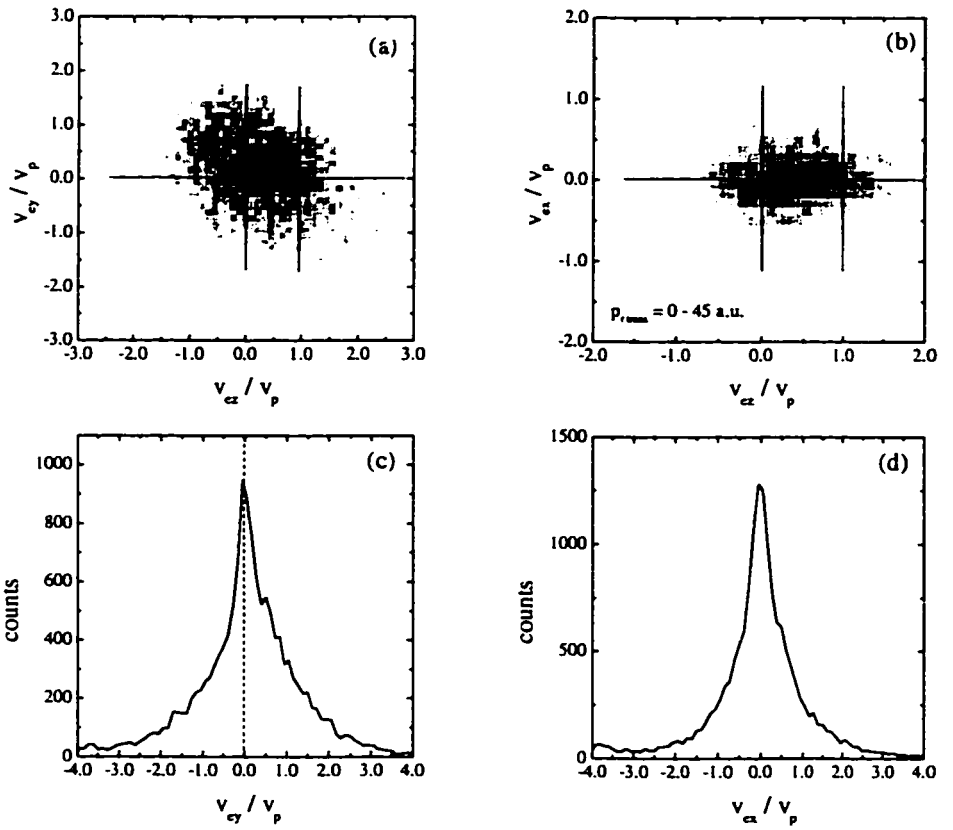

Figure F.11: (a) Top view and (b) side view of the ejected electrons in the collision of He^+ + Ne at $v_p = 0.33$ a.u. (c) and (d) are sideway projections of (a) and (b) respectively.

Appendix G

Data Analysis Code

Data were read and stored in a list mode. In this mode all the information concerning every single event are stored separately. This allowed us to virtually rerun the experiment and imply different conditions to the data. This kind of data analysis was necessary to make use of the coincidence nature of the experiments.

The on-line and off-line analysis of the data was carried out using the software XSYS [130]. The data reading and analysis was carried out through two files. The first file (.com) specifies the areas and gates to be generated and used to store and analyze the data. The second file (.evl) contains the code that tells the computer the calculations and restrictions that need to be done. This file produces the spectra as the calculations for every "event" are carried out.

In this appendix we will not discuss the details of data reduction. Rather we will include two files (.com and .evl) that were used in analyzing data of the experiments of chapter 4. It meant to be an illustration and it should be used for future reference.

```
$!###############TCJET.COM ###############
$!
$!By Mohammad Abdallah aug 7, 1996
$!modified to work with experiments involving the jet as a target
$!works for triple coincidence
$ DMEM ALL GLOBAL FILE
$ AMEM NEW 20000 PAGES*
$!---------------------------------Recoil detector--------------
$ AMEM   1   XR       2048
$ AMEM   2   YR       2048
$ AMEM   3   RR       2048
$ AMEM   4   SUMR     2048
$ AMEM   6   RXX      128
$ AMEM   7   RYY      128
$ AMEM   8   RXY      128 128
$ amem  106   rxl     2048
$ amem  107   ryl     2048
$ amem  108   rxyl    128 128
$!---------------------------------electron detector--------------
$ AMEM  11   XE       2048
$ AMEM  12   YE       2048
$ AMEM  13   RE       2048
$ AMEM  14   SUME     2048
$ AMEM  16   EXX      128
$ AMEM  17   EYY      128
$ AMEM  18   EXY      128 128
$!---------------------------------Porjectile detector-----------
$ AMEM  21   X1P      2048
$ AMEM  22   X2P      2048
$ AMEM  23   Y1P      2048
$ AMEM  24   Y2P      2048
$ AMEM  25   SUMP     2048
$ AMEM  26   PXX      128
$ AMEM  27   PYY      128
$ AMEM  28   PXY      128 128
$!---------------------------------TAC spec.----------------------
$ AMEM  31   TACER    2048     ! electron recoil TAC
$ AMEM  32   TACER2   128
$ AMEM  33   TACPR    2048     ! projectile recoil TAC
$ AMEM  34   TACPR2   128
$ AMEM  36   TACEP    2048     ! projectile electron TAC
$ AMEM  37   TACEP2   128
$ amem  39   t3ry     512 128
$!----------------coincidence spectra----------------------
$ amem  400   tacerpy2  128 128
$ amem  500   taceppy2  128 128
$ amem  600   tacerep   128 128
$ amem  700   tacerg61  2048
$ amem  800   2dpxpy    128 128
$!------------------2dpxpy enlargement----------------------
$ amem  823   ex5      512      !ex
$ amem  826   ex5m     512      !ex enlarged and shifted (exm)
$ amem  828   pxmexmg1   512    !rxm-exm gated on tacer gate #1
$ amem  829   pxmexmg2   512    !rxm-exm gated on tacer gate #2(bgrd)
$ amem  827   pxmexm   512      !828-829
$ amem  831   tacer5   512      !tacer
$ amem  832   tacer5m  512      !tacer enlarged and shifted
$ amem  833   px5      512      !rx
$ amem  834   py5      512      !ry
$ amem  835   py5m     512      !ry enlarged and shifted (rym)
```

```
$ amem  836   px5m      512       !rx enlarged and shifted (rxm)
$ amem  830   2dpxpyg    512 512 !rym vs rxm
$ amem  820   2dpxpygb   512 512 !rym vs rxm(background)
$ amem  825   2dpxpyr    512 512 !TO BE USED as 830-825
$ amem  840   ptrans    512       !prtrans (no angular limits)
$ amem  841   ptransbg   512      !prtrans on background (no limits)
$ amem  850   ptl      512 512    !prtrans(no) vs rxm(include bgrd)
$ amem  865   2dplbg   128 128    !rym vs rxm(background)
$ amem  867   2dpsub   128 128    !TO BE USED AS 860-865
$ amem  860   2dpl      128 128   !rym vs rxm
$ amem  870   ptll      128 128   !prtrans(no) vs rxm
$ amem  880   ptranssh   512      !prtrans (with angular limit)
$ amem  881   ptranshb   512     !prtrans on the background (int of 820)
$ amem  882   ptransfi   512     !880-881
$ amem  890   exptrans   128 512 !prtrans(no) vs ex
$ amem  895   explnm     128 128 !prl vs ex (ex not subtracted)
$ amem  896   explm      128 512 !prl vs ex (ex subtracted)
$ amem  891   rx5g1      512      !rxm gated on tacer gate #1
$ amem  892   rx5g2      512      !rxm gated on tacer gate #2
$ amem  893   rx5g3      512      !rxm gated on tacer gate #3
$ amem  894   rx5g4      512      !rxm gated on tacer gate #4
$!-------------recoil position gated on TACer/tacep----------
$ amem  61   rxyg1  128 128
$ amem  661  rxg1   128
$ amem  761  ryg1   128
$ amem  62   rxyg2  128 128
$ amem  63   rxyg3  128 128
$ amem  64   rxyg4  128 128
$ amem  65   rxyg5  128 128
$ amem  66   rxyg6  128 128
$!------------electron position gated on tacer/tacep---------
$ amem  71   exyg1  128 128
$ amem  72   exyg2  128 128
$ amem  73   exyg3  128 128
$ amem  74   exyg4  128 128
$ amem  75   exyg5  128 128
$ amem  76   exyg6  128 128
$!------------lectron gated on rec and tacer/tacep----------
$ amem  81   exyq9g1  128 128
$ amem  82   exyq9g2  128 128
$ amem  83   exyq9g3  128 128
$ amem  84   exyq9g4  128 128
$ amem  85   exyq9g5  128 128
$ amem  86   exyq9g6  128 128
$!-----rec gated on tacerpy2(400)/taceppy2(500)---------------
$ amem  461   rxyq1  128 128
$ amem  462   rxyq2  128 128
$ amem  463   rxyq3  128 128
$ amem  464   rxyq4  128 128
$ amem  561   rxyq5  128 128
$ amem  562   rxyq6  128 128
$ amem  563   rxyq7  128 128
$ amem  564   rxyq8  128 128
$!-------elec gated on rec and tacerpy2(400)/taceppy2(500)--------
$ amem  471   exyq9q1  128 128
$ amem  472   exyq9q2  128 128
$ amem  473   exyq9q3  128 128
$ amem  474   exyq9q4  128 128
$ amem  571   exyq9q5  128 128
$ amem  572   exyq9q6  128 128
```

```
$ amem  573   exyq9q7  128 128
$ amem  574   exyq9q8  128 128
$!----------------work areas--------------------------
$ amem  701   wa1     128
$ amem  702   wa2     128
$ amem  703   wa3     128
$ amem  704   wa4     128
$ amem  705   wa5     128
$ amem  706   wa6     128
$ amem  707   wa7     128
$ amem  708   wa8     128
$ amem  709   wa9     128
$ amem  710   wa10    128
$ amem  711   wa11    128
$ amem  712   wa12    128
$ amem  801   bwa1    2048
$ amem  802   bwa2    2048
$ amem  803   bwa3    2048
$ amem  804   bwa4    2048
$ amem  805   mwa1    512
$ amem  806   mwa2    512
$ amem  807   mwa3    512
$ amem  808   mwa4    512
$!---------------------------------------------
$ CLEAR FLAGS
$ GATE NEW
$ GATE
$ TDG ALLOC 1 Q1 SPEC 830
$ tdg alloc 2 q2 spec 830
$ tdg alloc 3 q3 spec 830
$ tdg alloc 4 q4 spec 830
$ tdg alloc 5 q5 spec 830
$ tdg alloc 6 q6 spec 830
$ tdg alloc 7 q7 spec 830
$ tdg alloc 8 q8 spec 830
$ tdg alloc 9 q9 spec 8
$ tdg alloc 10 q10 spec 830
$ GATE 31 3
$ GATE 36 3
$ CLEAR ALL
```

```
!
!
!###################TCJET.EVL#####################
!
!EVL FILE FOR TRIPLE COINCIDENCE EXPERIMENTS INVOLVING JET
!BY MOHAMMAD ABDALLAH ON AUG 7, 1996
!
!!!!!!!!!!!!!!!!PARAMETERS AND VARIABLES!!!!!!!!!!!!!!!!!!!
!
!---------PROJ. DET.---------
        REAL PTHS=-100
        REAL PTHH=2049
        REAL PGX1=1
        REAL PGX2=1
        REAL PGY1=1
        REAL PGY2=1
        REAL OFF=12
        REAL PCH=99
                REAL PX1
                REAL PX2
                REAL PY1
                REAL PY2
                REAL PS
                REAL PSS
                INTEGER PIX
                INTEGER PIY
                INTEGER PIXIY

!------------REC. DET.--------------
        REAL RTHS=200
        REAL RTHH=2049
        REAL RGX=1
        REAL RGY=1
        REAL RGR=1
        REAL RCH=250
        REAL RAMPX=1
        REAL RAMPY=1
        REAL RXSH=0
        REAL RYSH=0
        REAL RFACTOR=1.5
                REAL SRXF
                REAL SRYF
                REAL SRRF
                REAL RV1
                REAL RV2
                REAL RV3
                REAL RS
                INTEGER RIX
                INTEGER RIY
                INTEGER RIXIY
                        integer rixl
                        integer riyl
                        integer rixiyl
!--------------spectra enlargement-----------------
                integer rixm
                integer riym
                integer stacer5i
                real tacerc=256.0
                real taccon=1.0
                real ryc=70.0
```

```
                real rycon=4.0
                real rxc=70.0
                real rxcon=1.0
                integer zeone
                integer iseed=439787
                real templ
                integer testm
                integer testmm
                real riytemp
                real pyitemp
                real rixtemp
                integer pxitemp
        integer pxr
        integer pyr
        integer tacerr
        integer ptransr
        real pxreal
        real pyreal
        real tacreal
                real tantheta
                real xm256
                real aang=0.0
                real bang=1.0e9
                real cang=0.0
                real dang=1.0e9
        real tacbgc=256.0
        real tacbgcon=1.0
        integer stacer5g
        real tbg
        real 2dpnorm=1.0
        real tbgnorm
        integer tacsub
        real tacsubr
        real tbgr
                real eixtemp
                integer eixm
                real exc=256.0
                real excon=1.0
                real exreal
                integer exitemp
                integer rxmex
!               integer ripxybg
!
!------------ELEC. DET.--------------
        REAL ETHS=-100
        REAL ETHH=2046
        REAL EGX=1
        REAL EGY=1
        REAL EGR=1
        REAL ECH=250
        REAL EAMPX=1
        REAL EAMPY=1
        REAL EXSH=0
        REAL EYSH=0
        REAL EFACTOR=1.5
                REAL SEXF
                REAL SEYF
                REAL SERF
                REAL EV1
                REAL EV2
```

```
                REAL EV3
                REAL ES
                INTEGER EIX
                INTEGER EIY
                INTEGER EIXIY
!
!-------------VARIABLES FOR ROTATIONS------------------------
!
!--------------REC. DET. ----------------
        REAL RT=0        !ANGLE OF ROTATION FOR REC. DET.
        REAL SINRT
        REAL COSRT
        REAL X1SINRT
        REAL X1COSRT
        REAL RX0=65
        REAL RY0=65
        REAL RX1
        REAL RY1
        REAL RX2
        REAL RY2
        REAL RX3
        REAL RY3
!---------------ELEC. DET.----------------
        REAL ET=6.195919      !ANGLE OF ROTATION FOR ELEC. DET.
        REAL SINET
        REAL COSET
        REAL X1SINET
        REAL X1COSE
        REAL EX0=65
        REAL EY0=65
        REAL EX1
        REAL EY1
        REAL EX2
        REAL EY2
        REAL EX3
        REAL EY3
!------------TAC------------------
        REAL TACEPL=-100
        REAL TACEPH=2048
        REAL TACERL=-100
        REAL TACERH=2048
!
!----------GENERAL PURPOSE PARAMETERS----------
        REAL ZERO=0.0
        REAL ONETHIRD=0.33333333
        REAL FOUR=4
        REAL THREE=3
        REAL EIGHT=8
        real one=1.0
        REAL OTH=130
!
!--------------transverse momentum--------------
        real rycal=1.0
        real rxcal=1.0
        real rxg0=260.0
        real ryg0=260.0
!
!================ SORTING=========================
        OPTION ALLSPEC
        option tape
```

```
!
!
        FORMAT SPX2 1 12 1
        FORMAT SPY1 2 12 1
        FORMAT SPX1 3 12 1
        FORMAT SPY2 4 12 1
        FORMAT STACEP 5 12 1 ! TACEP
        FORMAT STACEP2 5 12 5 ! TACEP/8
        FORMAT SRX 6 12 1
        FORMAT SRY 7 12 1
        FORMAT SRR 8 12 1
        FORMAT STACER 9 12 1     ! TACER
        FORMAT STACER2 9 12 5  ! TACER/8
        format stacer5 9 12 3   !tacer/4
        FORMAT SEX    10 12 1
        FORMAT SEY    11 12 1
        FORMAT SER    12 12 1
!
                EVENT 2
        IF STACEP GT TACEPH EXIT
        IF STACEP LT TACEPL EXIT
        IF STACER GT TACERH EXIT
        IF STACER LT TACERL EXIT
        IF SPX1 GT PTHH EXIT
        IF SPX2 GT PTHH EXIT
        IF SPY1 GT PTHH EXIT
        IF SPY2 GT PTHH EXIT
        IF SRX GT RTHH EXIT
        IF SRY GT RTHH EXIT
        IF SRR GT RTHH EXIT
        IF SEX GT ETHH EXIT
        IF SEY GT ETHH EXIT
        IF SER GT ETHH EXIT
                tape
!===============CORRECTION FOR GAINS AND OFFSETS=================
!
!---------PROJ. DET.---------------
        GET SPX2
        SUB OFF
        MUL PGX2
        STA PX2
                GET SPX1
                SUB OFF
                MUL PGX1
                STA PX1
        GET SPY1
        SUB OFF
        MUL PGY1
        STA PY1
                GET SPY2
                SUB OFF
                MUL PGY2
                STA PY2
!-----------REC. DET.----------------
        GET SRX
        SUB OFF
        MUL RGX
        STA SRXF
        STA RV1
                GET SRY
```

```
                SUB OFF
                MUL RGY
                STA SRYF
                STA RV2
        GET SRR
        SUB OFF
        MUL RGR
        STA SRRF
        STA RV3
!------------ELEC. DET.-------------
        GET SEX
        SUB OFF
        MUL EGX
        STA SEXF
        STA EV1
                GET SEY
                SUB OFF
                MUL EGY
                STA SEYF
                STA EV2
        GET SER
        SUB OFF
        MUL EGR
        STA SERF
        STA EV3
!
!==========================DIVISIONS=======================
!-------------PROJ. DET.------------------
        LDA PY1
        ADD PX2
        STA PX
                LDA PX2
                ADD PY2
                STA PY
        ADD PX1
        ADD PY1
        ADD 1
        STA PS
                if ps eq 0 exit
                DIV FOUR
                STA PSS
                FIX
           IF PSS LT PTHS EXIT
                LDA PX
                MUL PCH
                DIV PS
                STA PIX7
                FIX
                STA PIX
                LDA PY
                MUL PCH
                DIV PS
                STA PIY7
                FIX
                STA PIY
!--------------REC. DET.-------------
        LDA RV3
        MUL RFACTOR
        ADD RV1
        ADD RV2
```

```
        STA RS
        div 3.
        sta rsn
                if rs eq 0 exit
    IF RSN LT RTHS EXIT
                LDA RV1
                MUL RCH
                DIV RS
                MUL RAMPX
                SUB RXSH
                STA RIX7
                FIX
                STA RIX
                        lda rix7
                        mul 16.0
                        fix
                        sta rixl
        LDA RV2
        MUL RCH
        DIV RS
        MUL RAMPY
        SUB RYSH
        STA RIY7
        FIX
        STA RIY
                        lda riy7
                        mul 16.0
                        fix
                        sta riyl
!--------------ELEC. DET.---------------
        LDA EV3
        MUL EFACTOR
        ADD EV1
        ADD EV2
        STA ES
                if es eq 0 exit
    IF ES LT ETHS EXIT
                LDA EV1
                MUL ECH
                DIV ES
                MUL EAMPX
                SUB EXSH
                mul -1.0
                add 130.0
                STA EIX7
                FIX
                STA EIX
        LDA EV2
        MUL ECH
        DIV ES
        MUL EAMPY
        SUB EYSH
        STA EIY7
        FIX
        STA EIY
!
!===================DETECTORS ROTATIONS=====================
!
!---------------------REC. DET.------------------------
        LDA RIX7
```

```
        SUB RX0
        STA RX1
                LDA RIY7
                SUB RY0
                STA RY1
        LDA RT
        SIN
        STA SINRT
                LDA RT
                COS
                STA COSRT
        LDA RX1
        MUL COSRT
        STA X1COSRT
        LDA RY1
        MUL SINRT
        ADD X1COSRT
        STA RX2
                LDA RX1
                MUL SINRT
                STA X1SINRT
                LDA RY1
                MUL COSRT
                SUB X1SINRT
                STA RY2
        LDA RX2
        ADD RX0
        STA RX3
        FIX
        STA RIX
                LDA RY2
                ADD RY0
                STA RY3
                FIX
                STA RIY
!---------------ELEC. DET.------------------
        LDA EIX7
        SUB EX0
        STA EX1
                LDA EIY7
                SUB EY0
                STA EY1
        LDA ET
        SIN
        STA SINET
                LDA ET
                COS
                STA COSET
        LDA EX1
        MUL COSET
        STA X1COSET
        LDA EY1
        MUL SINET
        ADD X1COSET
        STA EX2
                LDA EX1
                MUL SINET
                STA X1SINET
                LDA EY1
                MUL COSET
```

```
                SUB X1SINET
                STA EY2
        LDA EX2
        ADD EX0
        STA EX3
        FIX
        STA EIX
                LDA EY2
                ADD EY0
                STA EY3
                FIX
                STA EIY
!
!=====================SPECTRA INCREMENTS===============
!
!-----------TACS---------------
        TINC STACEP TACEP
        TINC STACEP2 TACEP2
        TINC STACER TACER
        TINC STACER2 TACER2
                TINC STACEr2 rIy tacerpy2
                STA TACERPYI
                tinc stacer2 rix taceppy2
                sta taceppyi
                tinc stacer2 stacep2 tacerep
                        if rixiy q9 then
                                tinc stacer2 riy rxyg1
                        endif
!----------PROJ.---------------
        TINC PX1 X1P
        TINC PX2 X2P
        TINC PY1 Y1P
        TINC PY2 Y2P
        TINC PSS SUMP
        TINC PIX PIY PXY
        STA PIXIY
        TINC PIX PXX
        TINC PIY PYY
!---------REC.----------------
        TINC SRXF XR
        TINC SRYF YR
        TINC SRRF RR
        TINC RSN SUMR
        TINC RIX RIY RXY
        STA RIXIY
        TINC RIX RXX
        TINC RIY RYY
                tinc rixl rxl
                tinc riyl ryl
                tinc rixl riyl rxyl
!--------------ELEC.----------------
        TINC SEXF XE
        TINC SEYF YE
        TINC SERF RE
        TINC ES SUME
        TINC EIX EIY EXY
        STA EIXIY
        TINC EIX EXX
        TINC EIY EYY
!=======================GATES=======================
```

```
        SPEC TACER
            GATE G1 TACER  1
            GATE G2 TACER  2
            GATE G3 TACER  3
        SPEC TACEP
            GATE G4 TACEP  4
            GATE G5 TACEP  5
            GATE G6 TACEP  6
!==============GATED SPECTRA INCREMENTS==============
!
!---rec and elec gated on tacer/tacep (and rec for elec)--
!
if stacer g1 then
        tinc rix riy rxyg1
        sta rxyg1s
        tinc rix rxg1
        sta rxg1s
        tinc riy ryg1
        sta ryg1s
        tinc eix eiy exyg1
        if rixiy q9 then
                tinc eix eiy exyq9g1
        endif
endif
if stacer g2 then
        tinc rix riy rxyg2
        tinc eix eiy exyg2
        if rixiy q9 then
                tinc eix eiy exyq9g2
        endif
endif
if stacer g3 then
        tinc rix riy rxyg3
        tinc eix eiy exyg3
        if rixiy q9 then
                tinc eix eiy exyq9g3
        endif
endif
!if stacep g4 then
!       tinc rix riy rxyg4
!       tinc eix eiy exyg4
!       if rixiy q9 then
!               tinc eix eiy exyq9g4
!       endif
!endif
!if stacep g5 then
!       tinc rix riy rxyg5
!       tinc eix eiy exyg5
!       if rixiy q9 then
!               tinc eix eiy exyq9g5
!       endif
!endif
!if stacep g6 then
!       tinc rix riy rxyg6
!       tinc eix eiy exyg6
!       if rixiy q9 then
!               tinc eix eiy exyq9g6
!       endif
!endif
!
```

```
!------rec and elec gated on 400/500 (and elec on rec)----
!
!
if rxygls ql then
        tinc stacer tacerg61
        sta stacg61
endif
tinc stacer2 riy 2dpxpy
tinc stacer5 riy t3ry
tinc stacer5 tacer5
!--------------enlarged spectra--------------------
        get stacer5
        sta templ
        ran iseed
        sub 0.500
        add templ
        sta templ
        sub tacbgc
        mul tacbgcon
        add 256.0
        sta tbg
        fix
        sta stacer5g
                get stacer5
                sta templ
                ran iseed
                sub 0.500
                add templ
                sta templ
                sub tacerc
                mul taccon
                add 256.0
                fix
                sta testm
        get stacer5
        sta templ
        ran iseed
        sub 0.500
        add templ
        sta templ
        sub tacerc
        mul taccon
        add 256.0
        sta tacreal
        fix
        sta stacer5i
                lda riy7
                sta templ
                ran iseed
                sub 0.500
                add templ
                sta templ
                mul 4.0
                sta riytemp
                fix
                sta pyitemp
                        lda riytemp
                        sub ryc
                        mul rycon
                        add 256.0
```

```
                        fix
                        sta testmm
                lda riytemp
                sub ryc
                mul rycon
                add 256.0
                sta pyreal
                fix
                sta riym
        lda rix7
        mul 4.0
        sta rixtemp
        fix
        sta rixm
                lda rixtemp
                sub rxc
                mul rxcon
                add 256.0
                sta pxreal
                fix
                sta pxitemp
        lda eix7
        mul 4.0
        sta eixtemp
        fix
        sta eixm
                        lda eixtemp
                        sub exc
                        mul excon
                        add 256.0
                        sta exreal
                        fix
                        sta exitemp
                lda pxreal
                add exreal
                sub 256.0
                fix
                sta rxmex
                        tinc stacer5i tacer5m
                        tinc riym pY5m
                        tinc stacer5i riym 2dpxpyg
                        sta 2dpxpyst
                        tinc stacer5g riym 2dpxpygb
                        tinc rixm px5
                        tinc pyitemp py5
                        tinc pxitemp px5m
        if stacer g1 tinc pxitemp rx5g1
        if stacer g2 tinc pxitemp rx5g2
        if stacer g3 tinc pxitemp rx5g3
                tinc eixm ex5
                tinc exitemp ex5m
                if stacer g1 tinc rxmex pxmexmg1
                if stacer g2 tinc rxmex pxmexmg2
!------------------constructing transverse mom. distribution----------
if 2dpxpyst q10 then
        lda stacer5i
        sub 256.0
        mul
        sta ripx2
        lda riym
```

```
!       tinc eix rxmex exptm
        tinc eix pxr explnm
        tinc eix rxmex explm
        tinc tbgr pyr 2dplbg
!-------------------------------------------------------------
if 2dpxpyst q1 then
        tinc rix riy rxyq1
        if rixiy q9 then
                tinc eix eiy exyq9q1
                tinc rixl bwa1
        endif
endif
if 2dpxpyst q2 then
        tinc rix riy rxyq2
        if rixiy q9 then
                tinc eix eiy exyq9q2
                tinc rixl bwa2
        endif
endif
if 2dpxpyst q3 then
        tinc rix riy rxyq3
        if rixiy q9 then
                tinc eix eiy exyq9q3
                tinc rixl bwa3
        endif
endif
if 2dpxpyst q4 then
        tinc rix riy rxyq4
        if rixiy q9 then
                tinc eix eiy exyq9q4
                tinc rixl bwa4
        endif
endif
if 2dpxpyst q5 then
        tinc rix riy rxyq5
        if rixiy q9 then
                tinc eix eiy exyq9q5
        endif
endif
if 2dpxpyst q6 then
        tinc rix riy rxyq6
        if rixiy q9 then
                tinc eix eiy exyq9q6
        endif
endif
if 2dpxpyst q7 then
        tinc rix riy rxyq7
        if rixiy q9 then
                tinc eix eiy exyq9q7
        endif
endif
if 2dpxpyst q8 then
        tinc rix riy rxyq8
        if rixiy q9 then
                tinc eix eiy exyq9q8
        endif
endif
!------------------- PTRANSVERSE BY CHOICE OF ANGLE -------
        lda stacer5i
        sub 256.0
```

```
        sta xm256
        if xm256 eq 0.0 exit
        lda riym
        sub 256.0
        div xm256
        sta tantheta
        if tantheta gt aang then
                if tantheta lt bang then
                        tinc ripxy ptranssh
                endif
        endif
        if tantheta lt cang then
                if tantheta gt dang then
                        tinc ripxy ptranssh
                endif
        endif
!--------------ptransverse by ang for background------------------
        lda stacer5g
        sub 256.0
        sta xm256
        if xm256 eq 0.0 exit
        lda riym
        sub 256.0
        div xm256
        sta tantheta
        if tantheta gt aang then
                if tantheta lt bang then
                        tinc ripxybg ptranshb
                endif
        endif
        if tantheta lt cang then
                if tantheta gt dang then
                        tinc ripxybg ptranshb
                endif
        endif
!++++++++++++++++++++++++++++++++++++++++++++++++++++++++++++++++
!+++++++++++        SALAMAT AND GOOD LUCK        +++++++++++++++
!++++++++++++++++++++++++++++++++++++++++++++++++++++++++++++++++
END
```

Bibliography

[1] A. Dalgarno and S. Lepp, in *Atomic, Molecular, & Optical Physics Handbook*, edited by G. W. F. Drake, (American Institute of Physics, Woodbury, New York, 1996) p. 919.

[2] R. K. Janev, in *Review of Fundamental Processes and Applications of Atoms and Ions*, edited by C. D. Lin, (World Scientific, Singapore, 1993) p. 1.

[3] J. Weisheit, in *Atomic, Molecular, & Optical Physics Handbook*, edited by G. W. F. Drake, (American Institute of Physics, Woodbury, New York, 1996) p. 978.

[4] J. Burgdörfer, in *Review of Fundamental Processes and Applications of Atoms and Ions*, edited by C. D. Lin, (World Scientific, Singapore, 1993) p. 517.

[5] E. T. Jensen, in *Atomic, Molecular, & Optical Physics Handbook*, edited by G. W. F. Drake, (American Institute of Physics, Woodbury, New York, 1996) p. 1007.

[6] H. Bichsel, in *Atomic, Molecular, & Optical Physics Handbook*, edited by G. W. F. Drake, (American Institute of Physics, Woodbury, New York, 1996) p. 1032.

[7] M. Inokuti, in *Atomic, Molecular, & Optical Physics Handbook*, edited by G. W. F. Drake, (American Institute of Physics, Woodbury, New York, 1996) p. 1045.

[8] N. Stolterfoht, R. D. DuBois, and R. D. Rivarola, Rev. Mod. Phys. (to be published).

[9] M. E. Rudd, Y. -K. Kim, D. H. Madison, and T. J. Gay, Rev. Mod. Phys. **64**, 441 (1992).

[10] D. H. Lee, P. Richard, T. J. M. Zouros, J. M. Sanders, J. L. Shinpaugh, and H. Hidmi, Phys. Rev. A **41**, 4816 (1990).

[11] H. I. Hidmi, P. Richard, J. M. Sanders, H. Schöne, J. P. Giese, D. H. Lee, T. J. M. Zouros, and S. L. Varghese, Phys. Rev. A **48**, 4421 (1993).

[12] T. J. M. Zouros, K. L. Wong, S. Grabbe, H. I. Hidmi, P. Richard, E. C. Montenegro, J. M. Sanders, C. Liao, S. Hagmann, and C. P. Bhalla, Phys. Rev. A **53**, 2272 (1996).

[13] Different authors contributions in *Forward Electron Ejection in Ion Collisions* edited by K. O. Groeneveld, W. Meckbach, and I. A. Sellin, Springer-Verlag (1984).

[14] J. S. Briggs, comments At. Mol. Phys. **23**, 155 (1989).

[15] Á Kövér, L. Sarkadi, J. Pálinkás, D. Berényi, Gy. Szabó, T. Vajnai, O. Heil, K. O. Groeneveld, J. Gibbons, and I. A. Sellin, J. Phys. B **22**, 1595 (1989).

[16] R. G. Pregliasco, C. R. Garibotti, and R. O. Barachina , J. Phys. B **27**, 1151 (1994).

[17] J. Macek, Nucl. Instrum. Methods Phys. Res. B **53**, 416 (1991).

[18] J. S. Briggs and J. H. Macek, Adv. At. Mol. and Opt. Phys. **28**, 1 (1991).

[19] W. Meckbach, P. J. Focke, A. R. Goni, S. Suarez, J. Macek, and M. G. Menendez, Phys. Rev. Lett. **57**, 1587 (1986).

[20] C. O. Reinhold and R. E. Olson, Phys. Rev. A **39**, 3861 (1989).

[21] G. C. Bernardi, S. Suarez, P. D. Fainstein, C. R. Garibotti, W. Meckbach, and P. Focke, Phys. Rev. A **40**, 6863 (1989).

[22] P. D. Fainstein, V. H. Ponce, and R. D. Rivarola, J. Phys. B **24**, 3091 (1991).

[23] S. Suarez, C. Garibotti, G. Bernardi, P. Focke, and W. Meckbach, Phys. Rev. A **48**, 4339 (1993).

[24] W. Cravero, C. Garibotti, Phys. Rev. A **50**, 3898 (1994).

[25] Y. D. Wang, V. D. Rodriguez, C. D. Lin, C. L. Cocke, S. Kravis, M. Abdallah, and R. Dörner, Phys. Rev. A **53** 3278 (1995).

[26] R. E. Olson, Phys. Rev. A **27**, 1871 (1983).

[27] R. E. OLson, Phys. Rev. A **33**, 4397 (1986).

[28] R. E. OLson, T. J. Gay, H. G. Berry, E. B. Hale, and V. D. Irby, Phys. Rev. Lett. **59**, 36 (1987).

[29] T. G. Winter and C. D. Lin, Phys. Rev. A **29**, 3071 (1984).

[30] W. L. Fite, R. F. Stebbings, D. G. Hummer, and R. T. Brackmann, Phys. Rev. **119**, 663 (1960).

[31] M. Pieksma and S. Y. Ovchinnikov, Comments At. Mol. Phys. **31**, 21 (1995).

[32] S. Yu. Ovchinnikov and J. H. Macek, Phys. Rev. Lett. **75**, 2474 (1995).

[33] M. Pieksma and S. Y. Ovchinnikov, J. Phys. B **25**, L373 (1992).

[34] M. Pieksma and S. Y. Ovchinnikov, J. Phys. B **24**, 2699 (1991).

[35] E. A. Solov'ev, Sov. Phys. Usp. **32**, 228 (1989).

[36] S. Y. Ovchinnikov and E. A. Solov'ev, Comments At. Mol. Phys. **22**, 69 (1988).

[37] S. Y. Ovchinnikov and E. A. Solov'ev, Sov. Phys. -JEPT **63**, 538 (1986).

[38] A. Bárány and S. Ovchinnikov, Physica Scripta **T46**, 243 (1993).

[39] V. D. Irby, T. J. Gay, J. Wm. Edwards, E. B. Hale, M. L. McKnzie, and R. E. Olson, Phys. Rev. A **37**, 3612 (1988).

[40] V. D. Irby, S. Datz, P. F. Dittner, N. L. Jones, H. F. Krause, and C. R. Vane, Phys. Rev. A **47**, 2957 (1993).

[41] T. J. Gay, M. W. Gealy, and M. E. Rudd, J. Phys. B **23**, L823 (1990).

[42] G. Bernardi, S. Suarez, P. Fainstain, C. Garibotti, W. Meckbach, and P. Focke, J. Phys. B **23**, L829 (1990).

[43] G. Bernardi, P. Fainstain, C. R. Garibotti, and S. Suarez, J. Phys. B **23**, L139 (1990).

[44] W. Meckbach, S. Suarez, P. Focke, and G. Bernardi, J. Phys. B **24**, 3763 (1991).

[45] R. D. DuBois, Phys. Rev. A **48**, 1123 (1993).

[46] R. D. DuBois, Phys. Rev. A **50**, PAGE (1994).

[47] M. Pieksma, S. Y. Ovchinnikov, J. van Eck, W. B. Westerveld, and A. Niehaus, Phys. Rev. Lett. **73**, 46 (1994).

[48] W. Wu, C. L. Cocke, J. P. Giese, F. Melchert, M. L. A. Raphaelian, and M. Stöckli, Phys. Rev. Lett. **75**, 1054 (1995).

[49] R. Dörner, H. Khemliche, M. H. Prior, C. L. Cocke, J. A. Gary, R. E. Olson, V. Mergel, J. Ullrich, and H. Schmidt-Böcking, Phys. Rev. Lett. **77**, 4520 (1996).

[50] J. Ullrich, R. Dörner, V. Mergel, O. Jagutzki, L. Spielberger, and H. Schmidt-Böcking, Comments At. Mol. Phys. **30**, 285 (1994)

[51] K. Ullmann, V. Mergel, L. Spielberger, T. Vogt, U. Meyer, R. Dörner, O. Jagutzki, M. Unverzagt, I. Ali, J. Ullrich, W. Schmitt, R. Moshammer, C. L. Cocke, T. Kambara, Y. Awaya, and H. Schmidt-Böcking, in *Proceedings of the Fourth US / Mexico Symposium on Atomic and Molecular Physics*, edited by I. Alvarez, C. Cisneros, and T. J. Morgan, World Scientific (1994) p. 269.

[52] R. Moshammer, M. Unverzagt, W. Schmitt, J. Ullrich, and H. Schmidt-Böcking, Nucl. Instrum. Methods Phys. Res. B **108**, 425 (1996).

[53] J. H. Macek, Nucl. Instrum. Methods Phys. Res. B **124**, 191 (1997).

[54] J. H. Macek, S. Yu. Ovchinnikov, in *Abstracts of the Twentieth International Conference on the Physics of Electronic and Atomic Collisions,* edited by F. Aumayr, G. Betz, and HP. Winter, (Vienna, Austria 1997), p. WE153.

[55] M. Pieksma, Nucl. Instrum. Methods Phys. Res. B **124**, 177 (1997).

[56] C. L. Cocke and R. E. Olson, Phys. Rep. **205**, 153 (1991).

[57] J. C. Levin, R. T. Short, C. S. O, H. Cederquist, S. B. Elston, J. P. Gibbons, I. A. Sellin, and H. Schmidt-Böcking, Phys. Rev. A **36**, 1649 (1987).

[58] J. Ullrich, H. Schmidt-Böcking, and C. Kelbch, Nucl. Instr. Meth. A **268**, 216 (1988).

[59] J. Ullrich, R. Dörner, S. Lencians, O. Jagutzki, and H. Schmidt-Böcking, Nucl. Instr. Meth. B **61**, 415 (1991).

[60] V. Frohne, S. Cheng, R. Ali, M. Raphaeilian, C. L. Cocke, and R. E. Olson, Phys. Rev. lett. **71**, 696 (1993).

[61] S. D. Kravis, M. A. Abdallah, C. L. Cocke, C. D. Lin, M. Stöckli, B. Walch, Y. D. Wang, R. E. Olson, V. D. Rodriguez, W. Wu, M. Pieksma, and N. Watanabe, Phys. Rev. A **54**, 1394 (1996).

[62] M. Abdallah, S. Kravis, C. L. Cocke, Y. Wang, V. D. Rodriguez, and M. Stöckli, Phys. Rev. A **56**, 2000 (1997).

[63] M. Abdallah, S. Kravis, C. L. Cocke, Y. D. Wang, , M. Stöckli, and R. E. Olson, Physica Scripta **T73**, 219 (1997).

[64] C. L. Cocke, in *Review of Fundamental Processes and Applications of Atoms and Ions*, edited by: C. D. Lin, (World Scientific, Singapore, 1993) P. 111.

[65] R. Phaneuf, in *Atomic, Molecular, & Optical Physics Handbook*, edited by G. W. F. Drake, (American Institute of Physics, Woodbury, New York) (1996) p. 724.

[66] C. L. Cocke, in *Atomic, Molecular, & Optical Physics Handbook*, edited by G. W. F. Drake, (American Institute of Physics, Woodbury, New York) (1996) p. 730.

[67] W. Wu, Ph.D. dissertation, Kansas State University, (1994).

[68] M. Pieksma, S. Yu. Ovchinnikov, J. Phys. B **27**, 4573 (1994).

[69] S. D. Berry, G. A. Glass, I. A. Sellin, K. O. Groeneveld, D. Hofmann, L. H. Andersen, M. Breinig, S. B. Elston, P. Engar, M. M. Schauer, N. Stolterfoht, H. Schmidt-Böcking, G. Nolte, and G. Schiwietz, Phys. Rev. A **31**, 1392 (1985).

[70] K. D. Sevier, *Low Energy Electron Spectrometry*, Wiley-Interscience (1972).

[71] D. L. Matthews, in *Methods of Experimental Physics, vol.* **17***; Atomic Physics; accelerators* edited by: P. Richard, (Academic Press, New York, 1980) p. 433.

[72] N. Stolterfoht, in *Fundamental Processes in Energetic Atomic Collisions*, edited by: H. O. Lutz, J. S. Briggs, and H. Kleinpoppen, (Plenum Press, New York, 1983) p. 295.

[73] N. Stolterfoht, Phys. Rep. **146**, 315 (1987).

[74] A. Niehaus, Phys. Rep. **186**, 149 (1990).

[75] W. Lichten, Phys. Rev. **164**, 131 (1967).

[76] M. E. Rudd, D. Gregoire, and J. B. Crooks, Phys. Rev. A **3**, 1635 (1971).

[77] T. F. M. Bonsen and Vriens, Physica **47**, 307 (1970).

[78] M. E. Rudd and J. Macek, Case Studies in Atomic Physics **3**, 47 (1972).

[79] E. J. Mansky, in *Atomic, Molecular, & Optical Physics Handbook*, edited by G. W. F. Drake, (American Institute of Physics, Woodbury, New York) (1996) p. 635.

[80] R. Abrines and I. C. Percival, Proc. Phys. Soc. London **88**, 861 (1966).

[81] R. Abrines and I. C. Percival, Proc. Phys. Soc. London **88**, 873 (1966).

[82] T. F. M. Bonsen and D. Banks, J. Phys. B **4**, 706 (1971).

[83] R. E. Olson and A. Salop, Phys. Rev. A **16**, 531 (1977).

[84] C. O. Reinhold and C. A. Falcon, Phys. Rev. A **33**, 3859 (1986).

[85] C. O. Reinhold, C. A. Falcon, and J. E. Miraglia, J. Phys. B **20**, 3737 (1987).

[86] R. E. Olson and T. J. Gay, Phys. Rev. Lett. **61**, 302 (1988).

[87] J. M. Hansteen and O. P. Mosebekk, Phys. Rev. Lett. **29**, 1361 (1972).

[88] J. H. McGuire and L. Weaver, Phys. Rev. A **16**, 41 (1977).

[89] R. E. Olson, J. Ullrich, and H. Schmidt-Böcking, J. Phys. B **20**, L809 (1987).

[90] A. Salin, J. Phys. B **2**, 631 (1969).

[91] G. B. Crooks and M. E. Rudd, Phys. Rev. Lett. **25**, 1599 (1970).

[92] J. H. Macek, Phys. Rev. A **1**, 235 (1970).

[93] M. E. Rudd, Y. -K. Kim, D. H. Madison, and J. W. Gallagher, Rev. Mod. Phys. **57**, 965 (1985).

[94] I. M. Cheshire, Proc. Phys. Soc. **84**, 89 (1964).

[95] Dž. Belkić, J. Phys. B **11**, 3529 (1978).

[96] D. S. F. Crothers and J. F. McCann, J. Phys. B **16**, 3229 (1983).

[97] P. D. Fainstein, V. H. Ponce, and R. D. Rivarola, J. Phys. B **21**, 287 (1988).

[98] D. S. F. Crothers, F. B. M. Copeland, and J. T. Glass, in *Atomic, Molecular, & Optical Physics Handbook*, edited by G. W. F. Drake, (American Institute of Physics, Woodbury, New York) (1996) p.589.

[99] M. Barat, in *Fundamental Processes in Energetic Atomic Collisions*, edited by: H. O. Lutz, J. S. Briggs, and H. Kleinpoppen, (Plenum Press, New York, 1983) p. 389.

[100] R. McCarroll, in *Atomic and Molecular Collision Theory*, edited by: F. A. Gianturco, (Plenum Press, New York, 1982) p. 165.

[101] E. E. Nikitin and S. Ya. Umanskii, *Theory of Slow Atomic Collisions*, (Springer-Verlag, Berlin, 1984).

[102] C. D. Lin, in *Fundamental Processes of Atomic Dynamics*, edited by: J. S. Briggs, H. Kleinpoppen, and H. O. Lutz, (Plenum Press, New York, 1988) p. 143.

[103] W. Fritsch and C. D. Lin, Phys. Rep. **202**, 1 (1991).

[104] W. Fritsch, in *Review of Fundamental Processes and Applications of Atoms and Ions*, edited by: C. D. Lin, (World Scientific, Singapore, 1993) P. 239.

[105] E. E. Nikitin, in *Atomic, Molecular, & Optical Physics Handbook*, edited by G. W. F. Drake, (American Institute of Physics, Woodbury, New York, 1996) p. 561.

[106] B. H. Bransden and C. J. Joachain, *Physics of Atoms and Molecules*, (Longman, London, 1986).

[107] N. Andersen, J. T. Broad, E. E. B. Campbell, J. W. Gallagher, and I. V. Hertel, Phys. Rep. **278**, 109 (1997).

[108] U. Fano and W. Lichten, Phys. Rev. Lett. **14**, 627 (1965).

[109] J. S. Briggs, in *Fundamental Processes in Energetic Atomic Collisions*, edited by: H. O. Lutz, J. S. Briggs, and H. Kleinpoppen, (Plenum Press, New York, 1983) p. 421.

[110] R. McCarroll, in *Atomic Processes and Applications*, edited by: P. G. Burke and B. L. Moiseiwitsch, (North-Holland Publishing Company, 1976).

[111] J. C. Brenot, J. Pommier, D. Dhuicq, and M. Barat, J. Phys. B **8**, 448 (1975).

[112] J. C. Brenot, D. Dhuicq, J. P. Gauyacq, J. Pommier, V. Sidis, M. Barat, and E. Pollack, Phys. Rev. A **11**, 1933 (1975).

[113] J. C. Brenot, D. Dhuicq, J. P. Gauyacq, J. Pommier, V. Sidis, M. Barat, and E. Pollack, Phys. Rev. A **11**, 1245 (1975).

[114] M. Barat, D. Dhuicq, R. Francois, C. L. Lesech, and R. McCarroll, J. Phys. B **6**, 1206 (1973).

[115] G. Gerber, A. Niehaus, and B. Steffan, J. Phys. B **6**, 1836 (1973).

[116] M. Barat, D. Dhuicq, R. Francois, R. McCarroll, R. D. Piacentini, and A. Salin, J. Phys. B **5**, 1343 (1972).

[117] R. McCarroll and R. D. Piacentini, J. Phys. B **4**, 1026 (1971).

[118] T. F. O'Malley, Phys. Rev. **150**,14 (1966).

[119] W. H. Miller, J. Chem. Phys. **52**, 3563 (1970).

[120] G. Gerber, R. Morgenstern, and A. Niehaus, J. Phys. B **6**, 493 (1973).

[121] G. Gerber, R. Morgenstern, and A. Niehaus, J. Phys. B **5**, 1396 (1972).

[122] E. A. Solov'ev, Sov. Phys. -JETP **54**, 893 (1981).

[123] M. Pieksma, Ph. D. dissertation, University of Utrecht (1993).

[124] M. P. Stöckli and C. L. Cocke, Nucl. Instrum. Methods Phys. Res. B **56/57**, 239 (1991).

[125] M. P. Stöckli, R. M. Ali, C. L. Cocke, M. L. A. Raphaelian, P. Richard, and T. N. Tipping, Rev. Sci. Instrum. **63**, 2822 (1992).

[126] M. P. Stöckli, P. E. Gibson, C. L. Cocke, B. D. DePaola, D. Fry, S. Kravis, D. Parks, P. Richrd, T.N. Tipping, B. Walch, and S. Winecki, Rev. Sci. Instrum. **67**, 1162 (1996).

[127] E. D. Donets, in *The Physics and Technology of Ion Sources*, edited by I. G. Brown, (John Wiley & Sons, New York, 1989) p. 245.

[128] S. Cheng, Ph.D. dissertation, Kansas State University, 1991.

[129] M.V. Frohne, Ph.D. dissertation, Kansas State University, 1994.

[130] XSYS/IUCF Data Acquisition Software, Indiana University Cyclotron Facility, Bloomington, IN 47405.

[131] Idaho National Engineering Laboratory, EG&G Idaho, Inc. Idaho Falls, ID 83415.

[132] N. Stolterfoht, K. Sommer, J. K. Swenson, C. C. Havener, and F. W. Meyer, Phys. Rev. A **42**, 5396 (1990).

[133] C. P. Bhalla, S. R. Grabbe, and A. K. Bhatia, Phys. Rev. A **52**, 2109 (1995).

[134] T. Vajnai, A. D. Gaus, J. A. Brand, W. Htwe, D. H. Madison, R. E. Olson, J. L. Peacher, and M. Schulz, Phys. Rev. A **74**, 3588 (1995).

[135] N. Toshima, Phys. Rev. A **50**, 3940 (1994).

[136] Y. D. Wang, C. D. Lin, N. Toshima, and Z. Chen, Phys. Rev. A **52**, 2852 (1995).

[137] Y. -Y. Hsu, M. W. Gealy, G. W. Kerby III, M. E. Rudd, D. R. Schultz, and C. O. Reinhold, Phys. Rev. A **53**, 303 (1996).

[138] Y. -Y. Hsu, M. W. Gealy, G. W. Kerby III, and M. E. Rudd, Phys. Rev. A **53**, 297 (1996).

[139] W. Wu, J. P. Giese, I. Ben-Itzhak, C. L. Cocke, P. Richard, M. Stöckli, R. Ali, and H. Schöne, Phys. Rev. A **48**, 3617 (1993).

[140] R. E. Olson, C. R. Feeler, C. J. Wood, C. L. Cocke, R. Dörner, V. Mergel, H. Schmidt-Böcking, R. Moshammer, and J. Ullrich, Nucl. Instrum. Methods Phys. Res. B **124**, 249 (1997).

[141] L. Vályi, *Atom and Ion Sources*, (John Wiley & Sons, London, 1977).

[142] G. Scoles, *Atomic and Molecular Beam Methods*, (Oxford University Press, New York, 1988).

[143] J. B. Hasted, *Physics of Atomic collisions*, (American Elsevier Publishing Company, Inc., New York, 1972) pp 153-161.

[144] A. Kantrowitz and J. Grey, Rev. Sci. Instr. **22**, 328 (1951).

IMAGE EVALUATION TEST TARGET (QA-3)

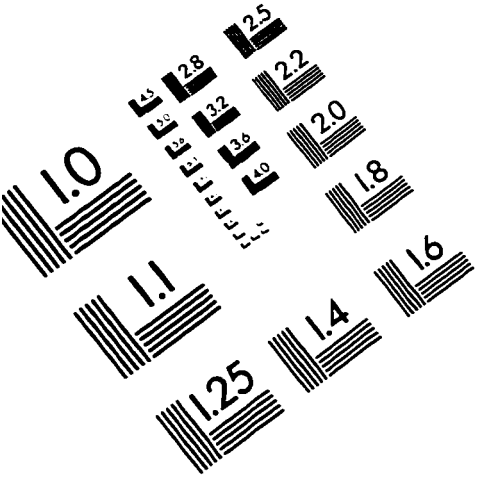

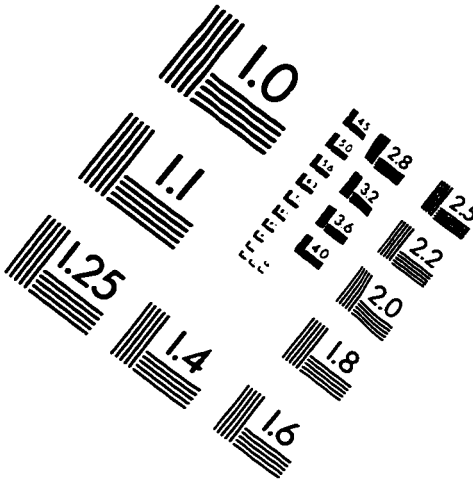

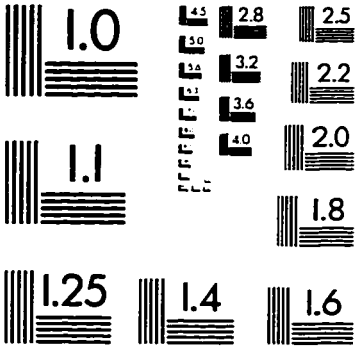

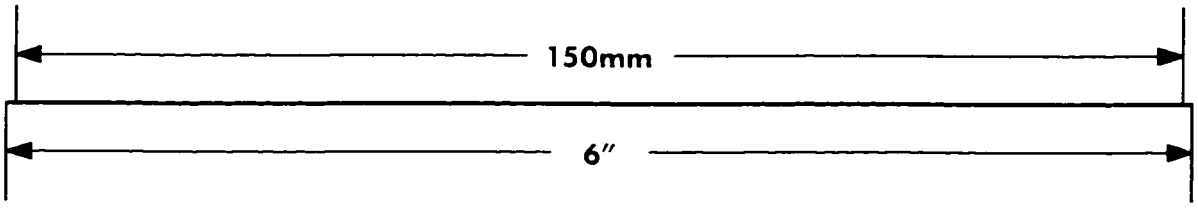

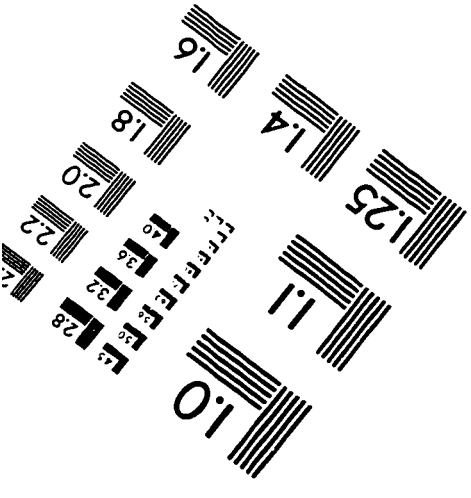

APPLIED IMAGE, Inc
1653 East Main Street
Rochester, NY 14609 USA
Phone: 716/482-0300
Fax: 716/288-5989
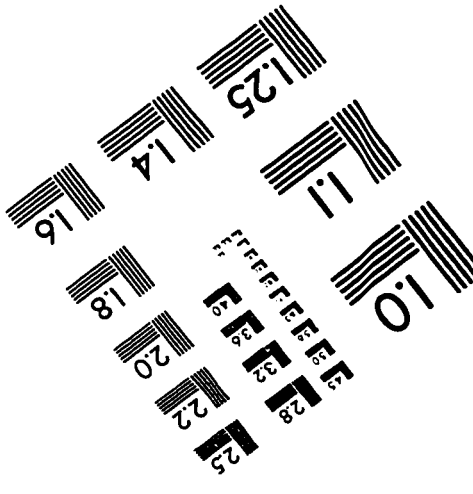
© 1993, Applied Image, Inc., All Rights Reserved